2011

Gold nanoparticle to antibody conjugates for diagnosis applications: molecular interactions and immunoassay development

Miguel Cavadas

Miguel Alexandre dos Santos Cavadas

Bachelor of Biochemistry

Gold nanoparticle to antibody conjugates for diagnosis applications: molecular interactions and immunoassay development

Thesis for the Master degree in Structural and Functional Biochemistry

Supervisor: Prof. Ricardo Franco, Faculdade de Ciências e Tecnologia da Universidade Nova de Lisboa

Jury:

President: Prof. Carlos Alberto Gomes Salgueiro

Examiner: Prof. Eulália Fernanda Alves de Carvalho Pereira

Vowel: Prof. José Ricardo Ramos Franco Tavares

FACULDADE DE CIÊNCIAS E TECNOLOGIA
UNIVERSIDADE NOVA DE LISBOA

September 2011

Miguel Alexandre dos Santos Cavadas

Bachelor of Biochemistry

Gold nanoparticle to antibody conjugates for diagnosis applications: molecular interactions and immunoassay development

Thesis for the Master degree in Structural and Functional Biochemistry

Supervisor: Prof. Ricardo Franco, Faculdade de Ciências e Tecnologia da Universidade Nova de Lisboa

Jury:

President: Prof. Carlos Alberto Gomes Salgueiro

Examiner: Prof. Eulália Fernanda Alves de Carvalho Pereira

Vowel: Prof. José Ricardo Ramos Franco Tavares

Gold nanoparticle to antibody conjugates for diagnosis applications: molecular interactions and immunoassay development

Abstract

Bionanotechnology is an area of rapidly increasing research interest, whose development can potentially improve many fields of our society by providing several advances in biomedical, energy and environment research fields. The present work includes both applied and basic research on bionanoconjugates of gold nanoparticles (AuNP) with antibodies (Ab) referred to as AuNP@Ab. The two main themes of research are:

i) development of a fluorescence immunoassay for malaria diagnosis, using a sensing methodology involving the competitive binding between a fluorophore-labeled antigen (CyAg) and the unlabeled antigen (Ag) to the AuNP@Ab conjugates. The Ag is a new biomarker of malaria infection, the heat shock protein 70 from *Plasmodium falciparum* (*Pf*Hsp70).

ii) physico-chemical characterization of the interaction between the Ag and the AuNP@Ab using Fluorescence, Differential Centrifugal Sedimentation (DCS), and Agarose Gel Electrophoresis (AGE), intended at understanding the nature of the binding, particularly its specificity and the influence of nonspecific protein competitors.

The immunoassay for malaria diagnosis was successfully established using fluorescence detection for AuNPs of different diameters (15 and 30 nm) and using AGE detection for 30 nm-AuNPs.

The AuNP@Ab bionanoconjugates exhibited a specific response to the target Ag, with little, or none, non-specific binding when purified transferrin (Trf) is used. Non-specific binding of proteins from plasma was nevertheless detected. Ag binding to AuNP@Ab was assessed in competitive conditions both with plasma and with Trf. Trf inhibited the Ag binding, while plasma inhibited the Ag binding as accessed by DCS but the same conclusion could not be made for fluorescence due to the large background signal caused by plasma unspecific binding.

Keywords: gold nanoparticles, antibody, antigen, bionanoconjugates, diagnosis.

Resumo

O interesse na investigação em bionanotecnologia está em grande crescimento, o seu desenvolvimento tem o potencial de melhorar várias áreas da nossa sociedade podendo fomentar avanços na investigação biomédica, energética e ambiental.

Este trabalho inclui investigação fundamental e aplicada usando boinanoconjugados de nanopartículas de ouro (AuNP) com anticorpos (Ab) designados por AuNP@Ab. Os dois principais temas de investigação são:

i) desenvolvimento de um imunoensaio de fluorescência para o diagnostico de malária usando uma metodologia que envolve a ligação competitiva entre o antigénio marcado com um fluoróforo (CyAg) e o antigénio não marcado (Ag). O Ag é um novo biomarcador da infecção de malária, a proteína de choque térmico 70 de *Plasmodium falciparum* (*Pf*Hsp70);

ii) caracterização fisico-química da interação entre o Ag e o AuNP@Ab usando fluorescência, sedimentação diferencial por centrifugação (DCS) e electroforese em gel de agarose (AGE), tendo em vista a compreensão da natureza da ligação, particularmente a sua especificidade e a influência de competidores proteicos não-específicos.

O imunoensaio para diagnostico de malária foi estabelecido com sucesso usando detecção por fluorescência com AuNP de diferentes diâmetros (15 e 30 nm) e usando detecção por AGE com 30 nm-AuNPs.

Os bionanoconjugados AuNP@Ab exibiram uma resposta específica para o Ag alvo com pouca, ou nenhuma, ligação não-específica quando Trf é usada. Foi contudo possível detectar a ligação não-específica das proteínas do plasma. A ligação de Ag à AuNP@Ab foi investigada em condições competitivas tanto na presença de plasma como de Trf. A Trf inibiu a ligação do Ag, enquanto o plasma inibiu a ligação de Ag de acordo com DCS, mas a mesma conclusão não se pode aplicar ao estudo com fluorescência devido ao elevado ruído analítico causado pela ligação não-específica de plasma.

Palavras chave: nanopartículas de ouro, anticorpo, antigénio, bionanoconjugados, diagnostico.

Contents

Figures

Tables

Acronyms and symbols

Ab	Antibody
ACS	American Chemical Society
ACT	Artemisinin-Based Combination Therapies
ATP	Adenosine triphosphate
Ag	Antigen
AGE	Agarose Gel Electrophoresis
AuNP	Gold nanoparticle
AuNP@Ab	Ab to AuNP conjugate
AuNP@Ab@Ag	Ag to AuNP@Ab conjugate
AuNP@Ab@Ag@Trf	AuNP@Ab@Ag incubated with transferrin
AuNP@Ab@Trf	AuNP@Ab incubated with transferrin
AuNP@Ag	Ag to AuNP conjugate
AuNP@Trf	Trf to AuNP conjugate
BB	Borate buffer
BNC	Bionanoconjugates
BSA	Bovine serum albumin
cTnT	Cardiac troponin T
CD	Circular dichroism
Cy3B	Cyanine 3B dye
DCS	Differential Centrifugal Sedimentation
DLS	Dynamic Light Scattering
DLVO	Derjaguin-Landau-Verwey-Overbeek theory
EDC	Ethyl(dimethylaminopropyl) carbodiimide
2E6	Anti-*Pf*Hsp70 antibody
F.I.	Fluorescence Intensity
Fab	Fragment antigen-binding
Fc	Fragment crystalizable
FQIA	Fluorescence Quenching Immunoassay
F.Inc.	Relative Fluorescence Increase
FRET	Förster Resonance Energy Transfer
GFP	Green Fluorescent Protein
HRP2	Histidine Rich Protein-2
HRP	Horseradish Peroxidase
ICH	International Conference on Harmonization of Technical Requirements for Registration of Pharmaceuticals for Human Use

Ig	Immunoglobulin
IUPAC	International Union of Pure and Applied Chemistry
IPTG	Isopropyl-1-thio-B-D-galactopyranoside
LB	Luria Broth
LDH	Lactate Dehydrogenase
LoD	Limit of Detection
LoIB	Limit of Inespecific Binding
LoINH	Limit of Inhibition
LoQ	Limit of Quantification
LSP	Localized Surface Plasmon
LSPR	Localized Surface Plasmon Resonance
MUA	Mercaptoundecanoic acid
NHS	N-Hydroxysuccinimide
NP	Nanoparticles
OD	Optical Density
PB	Phosphate buffer
PBS	Phosphate buffered saline
PBST	PBS containing 0.05% Tween 20
PdI	Polydispersity Index
*Pf*Hsp70	Cytosolic heat shock protein 70 from *Plasmodium falciparum*
RBC	Red Blood Cell
RDTs	Rapid Diagnostic Tests
RT	Room Temperature
SD	Standard Deviation
SDS	Sodium DodecylaureylSulfate
SDS-PAGE	Sodium DodecylaureylSulfate Polyacrylamide Gel Electrophoresis
SET	Surface Energy Transfer
SLoD	Statistical Limit of Detection
SLoQ	Statistical Limit of Quantification
SOB	Super Optimal Broth medium
SOC	SOB with Catabolite repression
SP	Surface Plasmon
SPP	Surface Plasmon Polaritons
Trf	Transferrin
TAE	Tris-Acetate-EDTA buffer
TEM	Transmission Electron Microscopy
WHO	World Health Organization

A	Absorbance
A_s	Surface area
C_{abs}	Absorption cross-section
C_{ext}	Extinction cross-section
C_{sca}	Scattering cross-section
D_{NP}	NP diameter
D_{dif}	Diffusion coefficient
D_{pd}	Scattering particle to detector distance
d_o	Donor to acceptor distance whose E_{SET} = 50%
E	Electric field
E_{ex}	Fluorophore excitation rate
$E_{ex,m}$	Fluorophore excitation rate in the presence of a metal surface
E_{SET}	SET energy transfer efficiency
E_{FRET}	FRET energy transfer efficiency
ε	Dielectric constant
ε_{im}	Imaginary part of the dielectric constant
ε_{re}	Real part of the dielectric constant
η	Dispersant viscosity
f	Frictional resistance to mobility
g	Gravitational acceleration
G	Free energy
γ_{SL}	Solid-liquid interfacial surface tension
I	Intensity of the light scattered by a particle
I_o	Intensity of the incident light
k	Wave vector
k_{nr}	Non-radiative fluorophore decay rate
k_m	Non-radiative fluorophore decay rate due to the presence of a metallic surface
κ	Boltzman constant
K	Combination of constants that relates sedimentation time and D_{NP}
λ	Wavelength
λ_{LSPR}	Wavelength of the LSPR frequency
λ_P	Wavelength of the bulk plasma frequency
m	Relative refractive index
μ	Electrophoretic mobility
n_{im}	Imaginary part of the refractive index
n_{med}	Refractive index of the medium
n_{re}	Real part of the refractive index

v	Electrophoretic migration velocity
ω	Rotational speed
q	Particle/molecule net charge
r	Donor to acceptor/surface distance in FRET/SET, respectively
R	NP radius
R_o	Förster radius, donor to acceptor distance whose $E_{FRET} = 50\%$
R_H	Hydrodynamic radius
R_{rot}	Centrifuge radius of rotation
$R_{rot,o}$	Initial centrifuge radius of rotation
$R_{rot,f}$	Final centrifuge radius of rotation
ρ	Density of particles (particles per unit volume)
ρ_p	Particle density (mass per unit volume)
ρ_f	Fluid density (mass per unit volume)
t	Time
T	Absolute temperature
τ	Fluorophore lifetime
Γ	Decay rate
Γ_m	Fluorophore decay rate in the presence of a metal surface
θ	Angle between the incident light and the detector
V	Settling velocity of the particle
X	Sedimentation distance

Chapter I

Introduction

In this chapter an overview of the proposed goals for the present work is presented, followed by a brief introduction to malaria and bioconjugate chemistry, with a focus on the antibody to gold nanoparticle conjugation. The chapter finishes with a detailed explanation of the underlying principles of the experimental techniques and the gold nanoparticle properties relevant to this work. For the sake of clarity, the antigen (Ag) used throughout this work is the *Pf*Hsp70, more precisely the cytosolic *Pf*Hsp70-1 form, and the antibody (Ab) is the monoclonal anti- *Pf*Hsp70 antibody 2E6. The terms Ag and Ab are used preferentially, although in some instances they might be referred to as *Pf*Hsp70 and 2E6.

1. Purpose of the work

The main goal of the present work was the development of a fluorescence immunoassay for the detection of *Pf*Hsp70, the target antigen (Ag), using conjugates (AuNP@Ab) of the monoclonal antibody 2E6, an anti-*Pf*Hsp70 antibody (Ab), and gold nanoparticles (AuNP). This would be a novel approach for the parasite-based diagnosis of malaria. The designed working hypothesis for the immunoassay detection mechanism is presented on Figure 1.1A. It is based on the AuNP's ability to quench fluorescence and the competitive binding between fluorophore labeled (CyAg) and unlabeled (Ag) forms of the antigen. Upon incubation of the AuNP@Ab with the CyAg (blank measurement), AuNP-induced fluorescence quenching would be expected as the Ab would sequester CyAg molecules close to the AuNP surface. Upon addition of unlabeled Ag, there would be a competition between the unlabeled and labeled forms of the antigen for the binding sites at the AuNP@Ab surface, increasing the amount of free CyAg relative to the blank. This increase would be dependent on the added concentration of Ag and therefore the fluorescence intensity increase would be a measure of the extent of Ag binding.

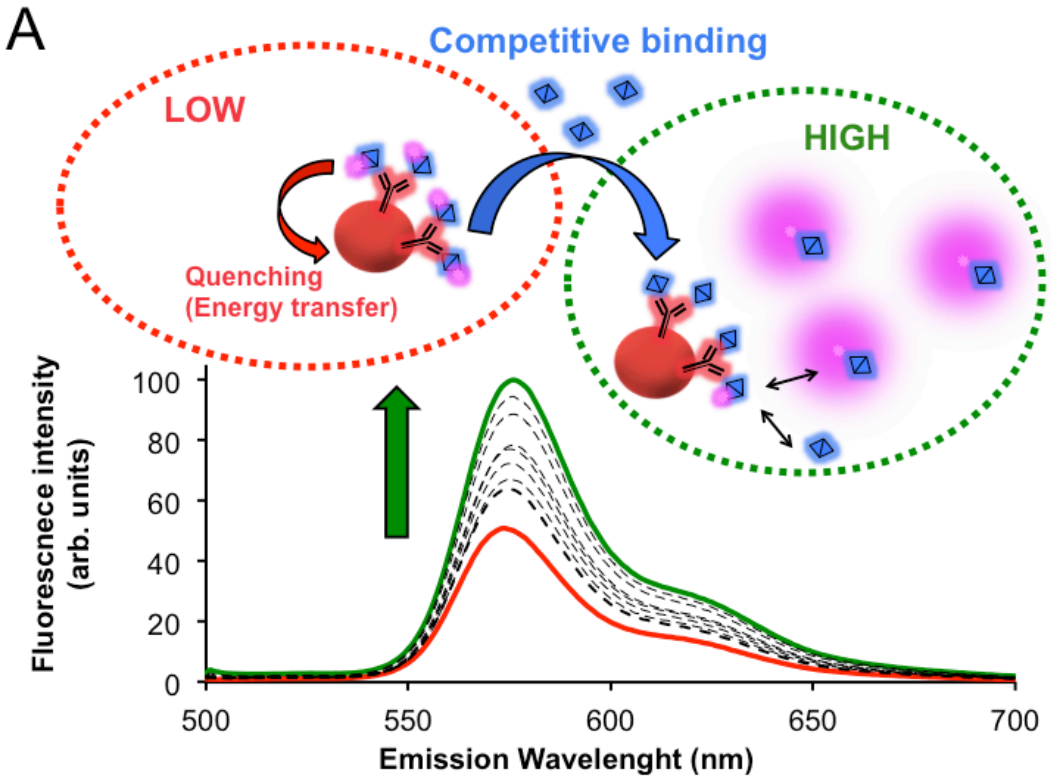

Figure 1.1 Purpose of the work. (A) Labeled and unlabeled forms of the Ag will compete for the AuNP@Ab binding sites, resulting in an increase in the fluorescence intensity (dotted lines and green line) with increasing Ag concentration in relation to the blank (red line).

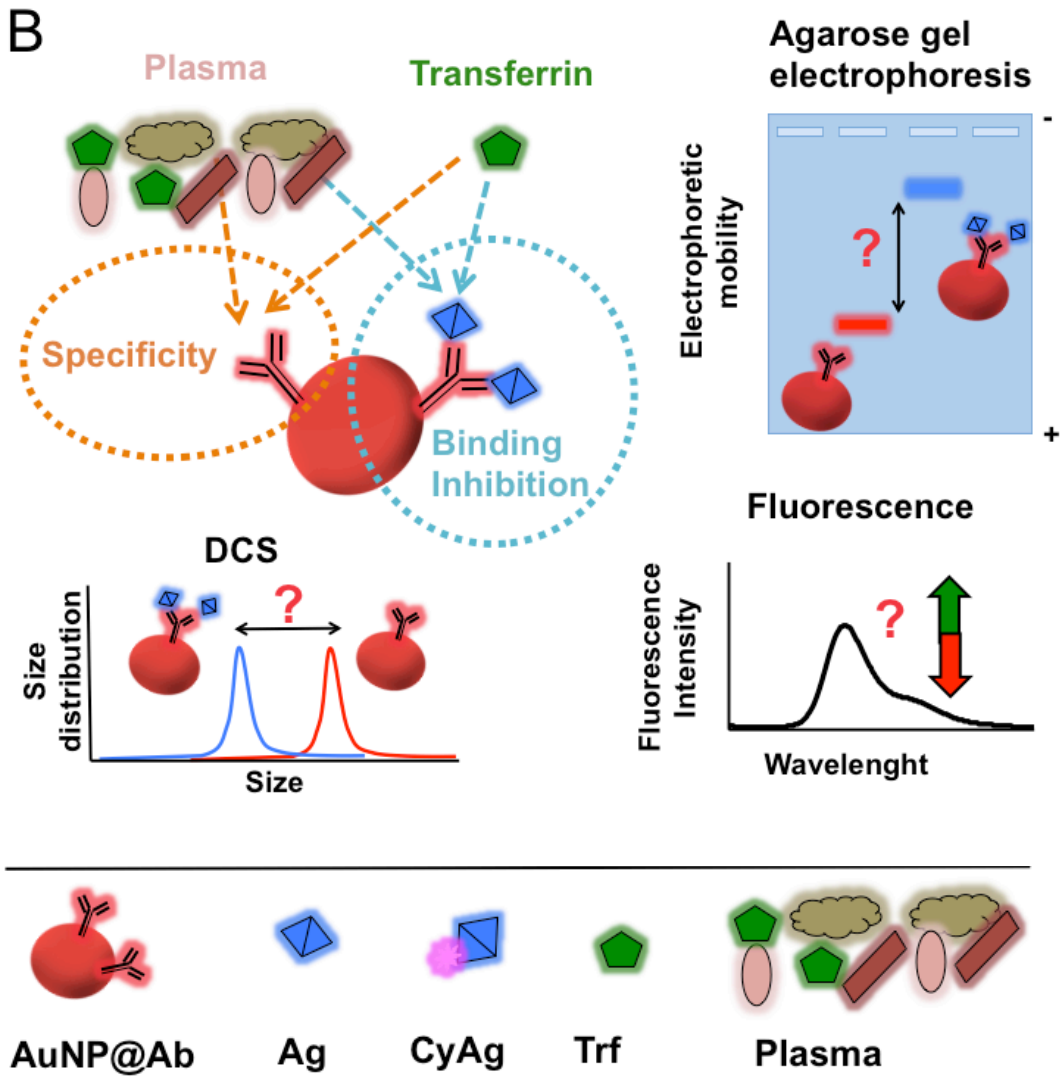

Figure 1.1 Purpose of the work. (Continued) (B) Changes in the analytical signals of fluorescence, DCS and AGE combined with the presence of human plasma and transferrin will be used to evaluate the Ag to AuNP@Ab binding inhibition and the specificity of the AuNP@Ab conjugates.

The studies were further extended to develop straightforward characterization approaches of the AuNP@Ab's activity. This is useful because this type of conjugates is widely used for bioassays and the maintenance of their activity is often the key to success of assay development[1]. In this regard, the characterization of the Ag to Ab binding was performed by several techniques including Agarose Gel Electrophoresis (AGE), Differential Centrifugal Sedimentation (DCS) and Fluorescence, with the studies being extended towards understanding the influence of: 1) the AuNP to Ab conjugation strategy, i.e. cross-linked *vs* electrostatic approach; 2) influence of transferrin (Trf) in the Ag to Ab binding. Trf is a protein that is naturally occurring in plasma and has a similar molecular weight (~80 KDa) to the Ag in use, *Pf*Hsp70 (~70 KDa), being therefore a suitable non-specific

competitor; 3) plasma on the Ag to Ab binding, and finally 4) proving the specificity of the Ag to Ab binding. A schematics of the proposed approach is presented in Figure 1.1B.

2. Malaria: disease and detection

Although estimations vary according to different reports, approximately 3 billion people live in malaria endemic areas of these around 500 million are infected each year, with between one to two million dying from the disease[2,3,4,5]. The following four species of *Plasmodium* (*P.*) cause malaria in humans: *Plasmodium falciparum*, *P. vivax*, *P. malaria*, and *P. ovale*. Of these, it is *P. falciparum* that accounts for the highest mortality rate[2,3,4,6]. Malaria is transmitted in tropical and subtropical areas where adequate temperature and humidity allow the proliferation of the mosquito vector, *Anopholes sp.*, at temperatures below 20 ºC transmission does not occur. Outside these areas malaria can be transfusion transmitted, but not sexually transmitted[3].

Plasmodium sp. have complex life cycles spanning two hosts and several phenotypically distinguishable stages. Once an human is bitten by an infected *Anopheles sp.* mosquito, sporozoites are released into the blood stream from which they reach the liver. Inside the hepatocytes they mature and replicate, culminating with the release of merozoites into the blood stream (exo-erythrocytic stage) were they infect RBC (erythrocytic stage)[6,7]. At this stage malaria symptoms are triggered [7,8]: high fevers, shaking chills, headaches and flu-like illness, starting after an incubation period that lasts from 7 to 30 days.[3] Exactly how malaria kills is not known, but evidence exists to a role of metabolic waste products of the parasite.[3]

The similarity between the symptoms of malaria and other febrile illness has lead to the unnecessary use of chloroquine, which led to the parasite having developed resistance. The new Artemisinin-based combination therapies (ACT) are expensive. These factors promoted a shift from a symptom-based diagnosis to a parasite-based diagnosis[9]. As light microscopy -the gold standard in parasite-based diagnosis- is generally not affordable at point-of-care, rapid diagnostic tests (RDTs) [10], which are inexpensive, fast, accurate and easy to use diagnostic are on demanding[10]. Current malaria RDTs employ mostly immunochromatographic devices that use antibodies for antigen capturing [11,12,13], and their usage combined with ACT and insecticide-treated nets resulted in >50% reductions in malaria cases in 2009 as compared to 2000, as stated in the World Health Organization (WHO) 2010 World Report on Malaria[5].

The three main malarial biomarkers used in RDT are Histidine Rich Protein 2 (HRP2), and plasmodial -Lactate Dehydrogenase (LDH), and -aldolase [10,12]. Information on their function and stage of expression is presented in Table 1.1, along with the information on inducible *Pf*Hsp70-1 the antigen studied in the present work.

The sensitivity and specificity of these tests is of major importance, with several factors influencing these analytical parameters [13,14]. Specificity and sensitivity can be influenced by the source of the antigen used to produce the antibodies, the epitope that the antibody recognizes and finally monoclonal antibodies can be more specific but less sensitive than polyclonal antibodies. For a reliable diagnosis of clinical malaria, parasites densities detected should be equal to or below the 2000 to 5000 parasites μL^{-1} range [12]. As the antigen levels in peripheral blood can vary, with LDH and aldolase rapidly cleared from circulation, while HRP2 can last for several weeks in the circulation even after parasite clearance[9,11], and in *P. falciparum*, mature stages of infected RBC are sequestered in the deep vasculature of tissues [9]; there can be a marked variation in the antigen to parasite density ratio[9] and the sensitivity of these assays will have to be high enough to detect very small amounts of the circulating antigen.

Additionally, false positive reactions for these RDT are known to happen with rheumatoid factor and heterophile antibodies[9], therefore driving the development of alternative detection modalities and antigen targets that could bypass these disadvantages.

*Pf*Hsp70-1 is the only of six *Pf*Hsp70s receiving widespread research attention, it is known as the cytosolic form, and is a member of Hsp70 family, one of the major Heat shock protein families, composed of highly conserved, ubiquitous proteins that occur in most life forms, whose main role is to act as molecular chaperones. Hsp bind to nonnative proteins, facilitating their folding to the native state, with adenosine triphosphate (ATP) expense, and are commonly stress-induced, albeit some can be constitutive. Hsp70 proteins have a molecular mass of ~70 kDa and consist of two distinct domains: the 45- kDa N-terminal domain that binds ATP, and the 25-kDa peptide-binding domain. Hsp70 proteins are localized in the *Escherichia coli* cytosol and in all compartments of eukaryotic cells such as chloroplast, endoplasmic reticulum lumen, mitochondrial matrix, and the cytosol[4].

The Hsp70 from *P. falciparum* (*Pf*Hsp70) was known to be detectable in the pellet of saponin treated *P. falciparum*-infected RBCs using Western Blot analysis[15], and a latex immunoagglutination assay has been developed using monoclonal antibodies for *Pf*Hsp70 detection in plasma, and it was capable of identifying *P. falciparum* infection at parasite densities ranging from 5 x 10^3 to 3.55 x 10^5 parasites.μL^{-1}, with sensitivity around 90%[11].

Table 1.1 Plasmodial antigens used for malaria diagnosis compared to *Pf*Hsp70

Antigen	General features	Ref.
HRP2	◆Present at the erythrocytic stage within the RBC's cytoplasm and membrane and in immature gametocytes; ◆Expression starts after RBC invasion by merozoites and ceases after RBC rupture; ◆Soluble and heat stable protein; ◆Involved in the parasite's detoxification of heme.	[9,10,12]
Aldolase & LDH	◆Present at the erythrocytic stage within the RBC's cytoplasm and in mature gametocytes; ◆Expression starts after RBC invasion by merozoites and ceases after RBC rupture; ◆Soluble protein; ◆Major enzyme of the parasite's glycolytic pathway.	[9,10,12]
*Pf*Hsp70-1	◆Present at both the exo-erythrocytic stage (cytoplasm and nucleus) and erythrocytic stages (membranous structures within infected RBC: Mauere's patches and parasitophorous vacuole); ◆It might also be found in circulation, as there are reports on human Ab against it; ◆Soluble protein; ◆Albeit being the only of six *Pf*Hsp70s receiving widespread research attention its function is still mostly unknown, with roles in cell cycle control, protein translation and immunogenicity being suggested.	[4]

3. Gold nanoparticle and bionanoconjugates: properties and characterization techniques

3.1. Bioconjugate chemistry

Understanding the supramolecular interactions between proteins and nanoparticles (NP) is central to their usage in sensing and therapeutic applications[16].

Under most conditions globular proteins, such as enzymes and immunoglobulins (Igs), show a strong tendency to adsorb at interfaces[17]. When the amount of protein adsorbed is determined as a function of the amount of protein in solution, at equilibrium, an adsorption isotherm is obtained, it is the starting point of most protein adsorption studies. Two parts can be distinguished, a rising part at low concentrations whose slope is an indication of the binding affinity and a plateau of binding saturation[17]. Investigations on simple "model" systems, consisting of a well-characterized protein, a well-characterized sorbent, and an aqueous solvent containing only non-buffering ions, have indicated that protein and sorbent hydrophobicity, charge distribution, protein structural stability, solution pH,

and ionic strength influence the affinity of a protein for a given interface[17]. These findings form the basis of a qualitative theory originally proposed by Norde and Lyklema[18,19,20], which indicates that structural rearrangements in the protein molecule, dehydration of the sorbent surface, redistribution of charged groups in the interfacial layer, and protein-surface polarity usually make the primary contributions to the overall adsorption behavior[17].

For nanometer sized adsorbents, as surface curvature departs from flatness, there is an observed decrease in the degree of protein coverage[21], potentially decreasing the affinity of some proteins to a point where adsorption no longer occurs[22,23], and leading to new opportunities of differential protein adsorption. Several qualitative trends have emerged regarding the influence of NP physicochemical parameters on the protein binding[24], these are summarized in Table 1.2.

Table 1.2 Influence of the NP's physicochemical properties on the protein binding

NP property	Influence on protein binding
Neutral surfaces	Correlate with slower protein surface coverage rates in relation to charged surfaces;
Hydrophobicity	Influences the kinetics, equilibrium, amount and identities of bound proteins;
Size, morphology, shape and curvature	Influences the amount of bound proteins but not its surface identity;
Hydrophilicity and steric hindrance	Correlated to decreased protein binding.

Adapted from Ref.[24]

The interactions of NP with complex biological media, namely plasma[23,25,26,27], is an important issue for therapeutic and sensing applications[28]. The concept of a protein-corona has been established to describe the structure that forms when NPs come into contact with biological fluids[22,23,25,26,27]. The NP-protein interactions are pair specific, which means that for each NP, there will be a range of equilibrium constants (one for each protein) representing the different (and competitive) binding mechanisms that are present[23], initially the proteins will be associated with a particle as a "soft corona", rather than a solid fixed layer, composed of loosely bound proteins evolving to an irreversibly attached protein '"corona"[23,28]. Proteins at high concentrations and with high association rates are expected to occupy initially the surface of the NP, but later they could be replaced by proteins at lower concentrations with slower exchange rates, and/or higher affinities[26,29]. Thus, the whole process of competitive adsorption of proteins onto a limited surface is based on abundance, affinities, and incubation time, collectively known as the "Vroman Effect"[29,30,31].

3.1.1. Protein structure and activity at the NP surface

Protein function is highly dependent on subtle changes in protein structure, which is very susceptible to the environment[1]. Therefore binding to NPs might alter protein conformation, expose new epitopes on the protein surface, or perturb the normal protein function[32].

Information about protein structural changes upon binding to nanoparticles has been based mainly on infrared spectroscopy, circular dichroism (CD), fluorescence, and other methods that can monitor changes in the secondary structure of proteins[32]. Nuclear magnetic resonance has also been used recently[32,33].

Protein activity is typically measured by enzyme substrate reaction, electrochemistry for a redox-active enzyme, or an antigen-binding tests with labeled antibodies[1].

The influence on structure and activity seems to be pair specific[34]. Using CD, citrate stabilized 15nm-AuNP have been shown to induce changes in the conformation of yeast Cytochrome c, but not in the horse-heart counterpart [35], while mercaptohexadodecanoic acid surface modified 10-nmAuNP induce structural changes in lysozyme but not in alpha-chymotrypsin[36]. Gagner *et al.* has shown that the same type of AuNPs do not affect the catalytic activity of alpha-chymotrypsin but inhibit the activity of lysozyme[36].

Effects on the kinetic evolution of the protein activity can also be present, e.g. the conjugation of peptin to AuNP decreases the loss of activity over time in comparison to the unconjugated counterpart[34].

3.1.2. Covalent *vs* non-covalent approaches

The ideal conjugation strategy should attach proteins in a controlled manner, resulting in a stable colloidal system with the required protein surface concentration and activity. Compared to physical adsorption, the most conventional approach, covalent coupling might have, in principle, some advantages for immunoassay development (Table 1.3).

Table 1.3 Comparison of the covalent and non-covalent conjugation approaches in immunoassays

Adsorbed Ab lose their activity	◆Only small amounts of Ab retain their activity when adsorbed at the surface of NPs (e.g. polystyrene[17] and Quantum Dots[37], possibly caused by changes in the protein structure; ◆Aappropriate ligands, such as PEG, might reduce this denaturation[17]; ◆Several covalent approaches have reduced the surface induced denaturation[28].
Covalent attachment is permanent	◆It might prevent elution of bound protein during storage, thus increasing shelf life[17] and increase the stability in complex biological medium[28]; ◆Displacement of physically adsorbed Ab might happen with additives (BSA, polyethylene glycol, casein) used to reduce non-specific reactions and aggregation; as well as with washing buffers used to remove loosely bound proteins and reduce non-specific interactions[17,38].
Antibody orientation	◆Correct spatial Ab orientation can be difficult via physical adsorption, whilst covalent attachment can orient the molecule properly, yielding increased activity and lower reagent consumption[17].
Covalence attaches more protein	◆Some evidence indicates that one can attach 10-40% more protein via covalence[17].
Covalence is more thermally stable	◆The covalent bond is more thermally stable and is therefore desirable in applications that require thermo cycling[17].

A major challenge in NP bioconjugate chemistry is obtaining a specific protein to NP binding while maintaining the protein activity[28]. In the simple form of non-covalent interaction, advantage is taken from complementary electrostatic interactions. While these are useful when specificity is not required, binding specificity might be achieved by controlling the NP's surface chemistry[28]. Covalent interaction may rely on multiple natural ligands (e.g. glutamate and lysine side chains)[28] or on a monovalent attachment (e.g. cysteine residues exhibiting strong affinity towards gold)[28]. Engineered ligands for covalent attachment like the ones provided by amine-carboxylate coupling methods[28] or strepatavidin/biotin coupling methods[16], among others [28], have reported successes in retaining protein's structure[28].

3.1.3 Antibody to nanoparticle conjugates

Immunoglobulins are bifunctional molecules. The Fab ("fragment antigen-binding") has antigen binding-activity, the Fc ("fragment cristalyzable") is responsible for the biological activity. The specificity of the Ab binding to a target protein Ag is the basis for many diagnostics and therapeutic applications, and it is imparted by the N-terminal domain of each chain which have the greater amino acid variations in the molecule[17,39,40,41]. See Figure 1.2 for structural and functional detail.

Ab adsorption to surfaces is usually an irreversible process and occurs rapidly[17,19,20]. The major interactions relevant to Ab adsorption from aqueous solution are hydrophobic, coulombic and hydrogen bonding. The major driving force is the entropy increase in water molecules released from surface interface. Ab adsorption to and desorption from adsorbent surfaces is dependent on time, temperature, nature of protein and adsorbent, ionic strength, protein concentration and surface tension. At pH 7, increasing the ionic strength gradually decreases the electrostatic forces between the Ab and the adsorbent, with hydrophobic interactions taking a predominant role. Although Ab desorption generally does not occur upon simple sample dilution, increasing the ionic strength might elute the bound antibody[17].

3.1.3.1. Antibody to AuNP conjugates in immunoassays

Nanoparticle to antibody conjugates have two major biomedical applications, namely therapy and diagnosis. Targeted drug and gene delivery, together with magnetical or optical hyperthermia are the major potential therapeutic applications; cell sorting and bio-separation, imaging, and sensing are the major diagnosis applications[16].

Gold nanoparticles have been used as radioactive labels in vivo since the 1950s, and since the 1980s immuno-conjugated AuNPs have found utilization as density probes in electron microscopy of biological samples.

From the point of view of in vivo applications, AuNP are practically non-toxic[42], and easy to functionalize with appropriate ligands. These ligands afford additional robustness to a delivery/imaging system in which the gold core imparts stability to the assembly, while the functionalization monolayer allows tuning of surface properties, such as charge and hydrophobicity[43]. From the point of view of diagnostics applications, AuNPs surface enhanced and distance- and refractive index-dependent spectroscopic properties make them unique players in the bio-detection arena.

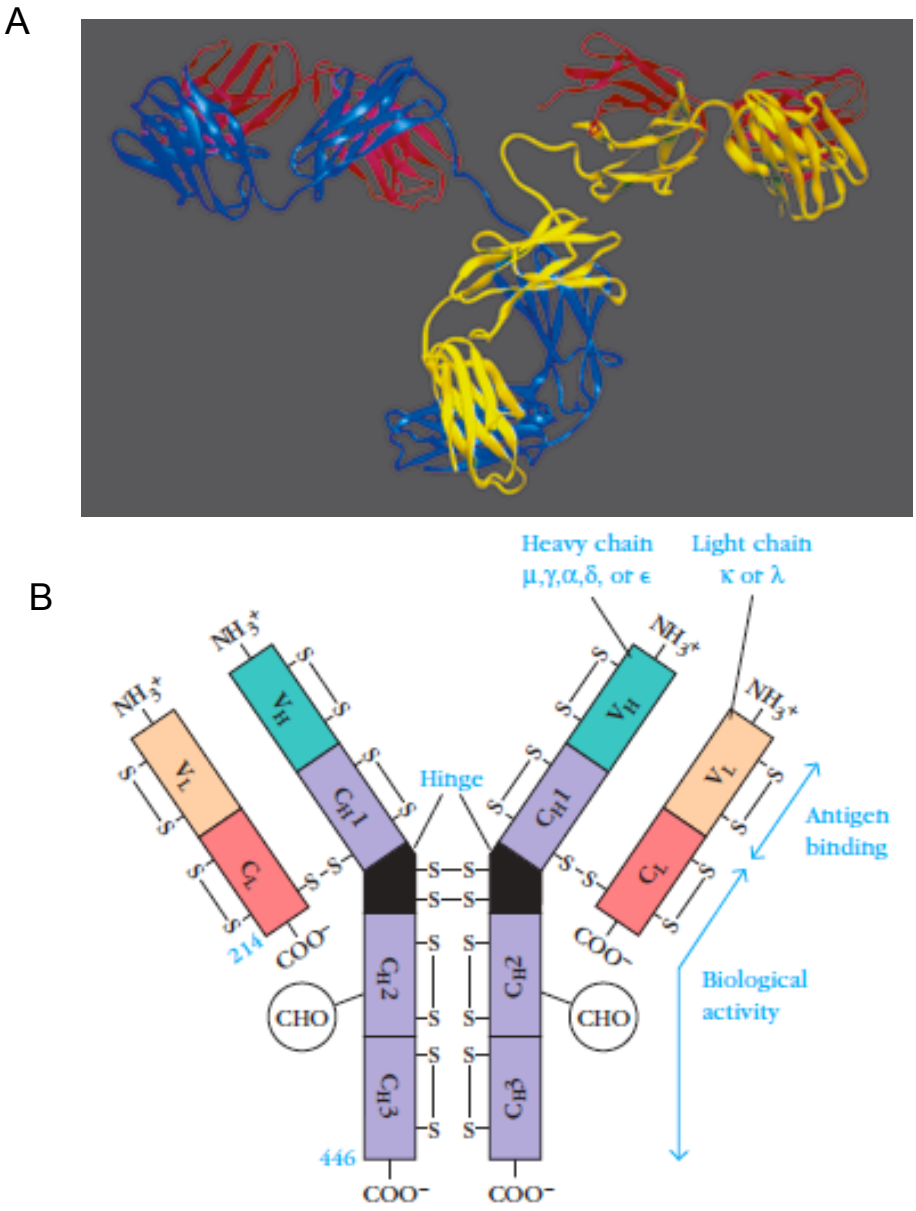

Figure 1.2 Immunoglobulin's structure and function. (A) Ribbon representation of an intact monoclonal antibody. The domains of the molecule are readily visible as is the extended conformation of the hinge region. The Ig is composed of a tetrameric arrangement of pairs of identical light (red) and heavy (yellow and blue) polypeptide chains held together by non-covalent forces and inter-chain disulfide bridges, composed of 2 and 4 domains respectively. These are homologous domains composed of two β-pleated sheets, each containing antiparallel β strands connected by loops. This structure is called an immunoglobulin fold (present in many other molecules besides immunoglobulins, particularly membrane signaling proteins), and the two β-sheets within an immunoglobulin fold are stabilized by hydrophobic interactions between them and by a conserved disulfide bond[39,40,41]. Image based on X-ray crystallography adapted from Ref.[41]. (B) Schematic diagram of immunoglobulin's structure adapted from Ref.[41]. Each heavy (H) and light chain (L) contains an amino-terminal variable (V) region (green and orange, respectively) responsible for binding specificity. The remainder of each chain in the molecule, the constant (C) regions (purple and red), exhibits a limited variation that defines the two light-chain subtypes and the five heavy-chain subclasses: γ, δ, α, μ and ε; and distinguishes the Ig class: IgG, IgD, IgA, IgM, and IgE, respectively. Of these, IgG is the most abundant and its structural characteristics are better understood. Chains γ, δ and α contain a proline-rich hinge region [44], μ and ε, which lack an hinge region, contain an additional immunoglobulin domain in the Fc portion of the molecule[41].

Three main approaches can be defined for bio-diagnostics using AuNPs, based on the type of nanoscale properties involved[45]: i) colorimetric sensing depending on inter- AuNP distance, representing the most developed approach, especially for specific nucleic acid sequence detection; ii) surface-functionalized AuNPs providing highly selective probes that are most generally used in fluorescence quenching-based assays, although surface-enhanced based assays are also gaining importance; and (iii) electrochemical detection methods based on electrical signal enhancement provided by AuNPs.

AuNPs, fluorescent NPs (especially quantum dots) and magnetic NPs, are the three main types of players in the development of probes for biological sensing. Here the focus will be on AuNPs.

AuNPs are used in immunoassays involving electrochemical[46,47,48,49,50] and chemiluminescent methods[51,52,53,54,55,56]. They are used as color probes[57,58] scattering enhancers[59,60], and sensing using AuNPs can also be plasmonic based[61,62,63]. Finally AuNPs can be used in fluorescence quenching immunoassays (FQIA)[64,65,66,67,68], that will deserve special attention in this work.

Fluorescence quenching by AuNPs has been advantageously used in a cardiac troponin T (cTnT) non-competitive sandwich immunoassay[67], a biotin competitive immunoassay with the antigen immobilized on AuNP-Latex[68] and a competitive immunoassay for a drug to BSA conjugate (digoxigenin) with a LOD on the nanomolar range[66]. The latter was the basis for the current work, in which the antigen was labeled with Cyanine3B dye (Cy3B), without the need for BSA coupling (Figure 1.3).

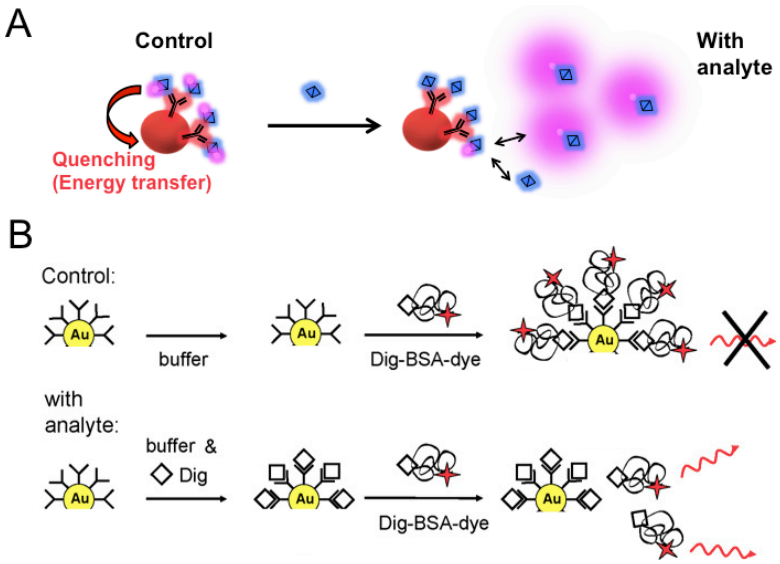

Figure 1.3 Fluorescence quenching immunoassays using AuNP. (A) The assay proposed in this work, a competitive homogenous *Pf*Hsp70 FQIA. CyAg is quenched in the presence of AuNP@Ab, fluorescence is restored upon Ag addition. (B) Competitive homogenous digoxigenin (dig) FQIA. Dig-BSA-fluorescent dye conjugates are quenched in the presence of AuNP conjugated to anti-digoxigenin Ab, fluorescence is recovered upon digoxigenin addition[66].

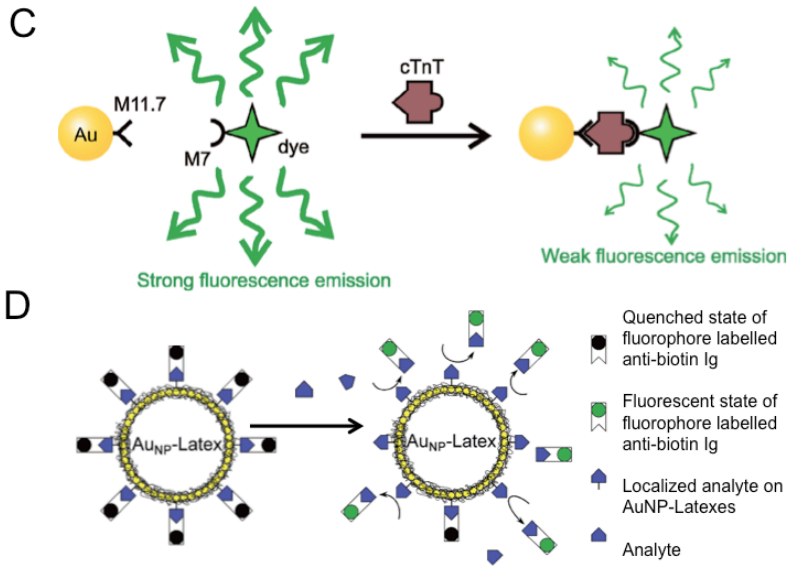

Figure 1.3 Fluorescence quenching immunoassays using AuNP. (Continued) (C) Sandwich homogenous cardiac troponin T (cTnT) FQIA. Two different anti-cTnT antibodies, labeled with a fluorophore or an AuNP, form a sandwich immunoassay in the presence of cTnT, resulting in quenching[67]. (D) Competitive homogenous biotin FQIA. Fluorophore labeled anti-biotin Ab bind to the biotin immobilized on AuNP covered latex particle, resulting in fluorescence quenching. Addition of biotin restores the fluorescence.[68]

3.1.4. Colloidal stability

The isoelectric point of most polyclonal IgG molecules is in the range 6.5-8.5. IgG polyclonal antibodies present a low charge density, therefore, when the particles are covered by IgG a non-specific agglutination process might take place under physiological conditions (pH 7.4 and ionic strength 150 mM), since there is almost no electrostatic repulsion between the antibody coated particles[17]. Antibody-coated particles must be completely stable in the absence of the antigen, otherwise, there will be a decrease in the available antigen binding sites, and loss of sensitivity.

But, what is colloidal stability? When a cube with 1 cm of edge immersed in a fluid medium is divided into small colloidal cubes with 10 nm of edge, the surface area (A_s) of the system increases from 6 cm^2 to 600 m^2 (Figure 1.4). This increasing area process is accompanied by a change in the free energy given by the expression[17]:

$$\Delta G = \gamma_{SL} \times \Delta A_s \qquad \text{Eq.1}$$

where γ_{SL} is the solid-liquid interfacial surface tension. Two situations can occur, $\gamma_{SL}>0$, therefore $\Delta G > 0$, the colloidal dispersion is thermodynamically unstable, the particles tend to assemble to reduce

the interfacial area (aggregation phenomena), the colloid is called lyophobic. Conversely if $\gamma_{SL}<0$ the particles are thermodynamically stable and the colloid is lyophilic. The term colloidal stability refers to the ability of a suspension to resist aggregation. The colloidal stability may be either thermodynamic or kinetic. Lyophilic colloids are thermodynamically stable systems whereas lyophobic colloids are kinetically stabilized. The kinetic stability is a consequence of an energy barrier opposing collisions between the particles and possible subsequent aggregation[17].

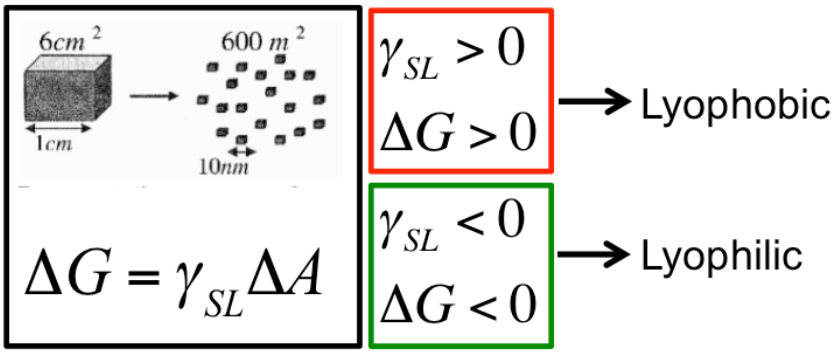

Figure 1.4 Changes in the free energy of a fluid immersed-cube upon fragmentation. The change in the surface area is accompanied by a change in γ_{SL} that determines the thermodynamically stability of the colloid. Thermodynamically stable and unstable colloids are named lyophilic and lyophobic, respectively. Adapted from Ref.[17].

The tendency towards aggregation of lyophobic colloids is attributable to the universal attractive van der Waals forces. In some cases, this attractive force between particle and medium is stronger than that between particles, with the result that the colloidal state is preferred, i.e., the system is lyophilic.

For lyophobic colloids only when the attractive van der Waals force is counteracted by a repulsive force can some degree of stability be obtained. When the particles have charges on the surface the colloid may be electrostatically stabilized. In some cases, a suitable polymer can be adsorbed on the particle surface, as the two surfaces are brought closer together the concentration of polymer units increases in the overlap region with a resulting increase in the osmotic pressure. This tends to bring in solvent from the surrounding medium, with a consequent repulsive force to separate the particles. This polymer-induced stability is referred to as steric stability[17].

The Derjaguin-Landau-Verwey-Overbeek (DLVO) theory of colloidal stability occupies a central position in colloid science. According to this theory, the stability is predicated on the notion that two independent types of forces govern the interaction between similar colloidal particles immersed in polar (especially aqueous) solutions: attractive van der Waals forces and repulsive electrostatic forces due to the net charge of the particle[17].

Adding salt to a dispersion initiates aggregation by suppressing the electrostatic repulsion

between particles. The energy barrier decreases with increasing electrolyte concentration and disappears above certain salt concentration called critical coagulation concentration. The study of this concentration is a practical way to determine colloidal stability[17].

When water is the dielectric medium in which colloidal particles are suspended, the DLVO theory generally fails to predict the stabilities of very hydrophobic or very hydrophilic particle suspensions. For example, the colloidal stability of silica at its isoelectric point, and many hydrophilic colloidal particles, most biological surfaces and macromolecules, remain separated in aqueous solution even in high salt or in the absence of any net surface charge[17].

3.2. Light scattering theory and Dynamic Light Scattering

3.2.1. Light scattering theory

When light impinges on a molecule the electric field induces an oscillating polarization of the electrons, the time varying dipole therefore created reradiates light in all directions and the molecules are said to scatter light[69,70].

Besides light scattering, energy from the electromagnetic radiation can be removed by light absorption, the process by which light energy is converted to internal heat. The combined processes of energy removal from light are usually called extinction[71,72,73].

Rayleigh's theory of light scattering assumes that when a purely scattering small spherical particle, with radius *R,* is exposed to light with an wavelength (λ) much longer than the radius of the particle ($R << \lambda$), every electron in the particle senses the same phase of the wave therefore oscillating and scattering light with the same phase. However when the particle is comparable to or larger than λ ($R \geq \lambda$), electrons in different parts of the particle oscillate with different phases. At this point a new theory is needed and Gustav Mie provided it [74]. In simple terms, and in opposition to Rayleigh, Mie described the scattering as the combination of light from oscillating electric dipoles, quadruples, and other higher order multiples [73], a visual depiction of these multipoles can be seen in Figure 1.5 Mie's theory can be applied for larger particles and particles that do absorb light[74].

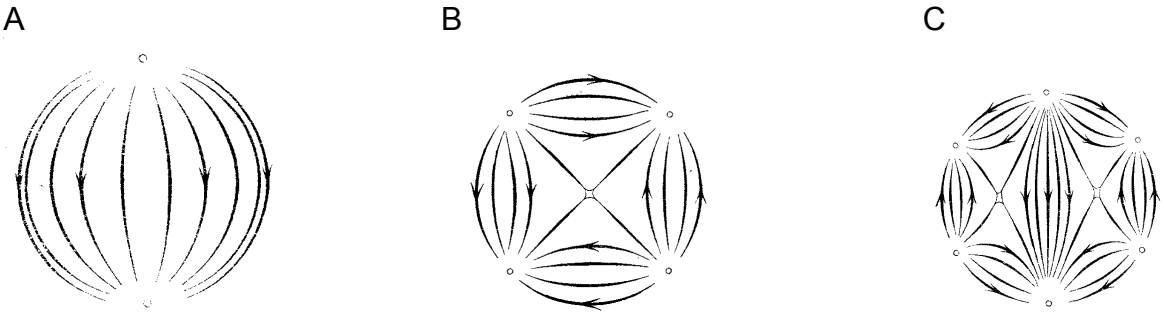

Figure 1.5 Mie's original depiction of the electric multipoles in colloidal metal spheres using electric field lines of force. (A), (B) and (C) dipole, quadrupole and otcupole electric field modes depicted by electric flied lines. Adapted from Ref.[72,74].

The original theory of Rayleigh was developed for pure light-scattering particles (real refractive index only), however, Mie theory shows that the Rayleigh equations also apply when the relative refractive index (m) is complex and the particle radius is much smaller than the wavelength, $R << \lambda$, [73] this is sometimes called the Rayleigh approximation[75], and it can be more precisely defined by the condition[76,77]:

$$R << \frac{\lambda}{2\pi n_{med}|m|} \qquad \text{Eq.2}$$

were n_{med} is the refractive index of the medium where the particle is immersed, and λ is the wavelength, more accurately, in this and every other equation it represents the wavelength in vacuum. It is clear from this equation that the size limit of Rayleigh applicability on explaining the scattering properties of particles depends on several parameters including the wavelength of the incident light and the dispersant and material refractive indexes.

The real and imaginary components of a complex m, at a given wavelength are given by[73]:

$$m = \frac{(n_{re} + in_{im})}{n_{med}} \qquad \text{Eq.3}$$

where n_{re} and n_{im} are the real and imaginary refractive indexes in vacuum. The refractive index of particles which scatter but do not absorb light in a given wavelength range is always real ($n_{im} = 0$) in that range, whereas the refractive index of particles which both scatter and absorb light is complex ($n_{im} \neq 0$). It is the imaginary part n_{im} of the refractive index that accounts for light absorption and also leads to intense light scattering.

In the Rayleigh approximation, the intensity of the scattered light (I) from an unpolarized light is given by[17,72,73]:

$$I = \frac{8\pi^2 R^6 n_{med}^4 I_0}{d^2 \lambda^4} \left| \frac{m^2 - 1}{m^2 + 2} \right| (1 + \cos^2 \theta) \qquad \text{Eq.4}$$

where I_0 is the intensity of the incident light, d is the distance betwenn the particle and the detector, n_{med} is the refractive index of the medium surrounding the particle, and m is the relative refractive index of the bulk particle material (refractive index of a macroscopic piece of the material of which the particle is made divided by n_{med}) and θ is the angle between the incident light and the detector[73]. The light scattering intensity expressions presented above are for single particles, however all of these expressions apply directly to particle suspensions with low particle concentrations where the particles are sufficiently far apart such that inter-particle perturbations and multiple scatterings are insignificant[73].

3.2.2. Dynamic light Scattering

Light scattering by spherical particles can be used for estimating their size. One technique with widespread use for nanotechnology applications is dynamic light scattering (DLS). In DLS experiments a monochromatic beam of laser light impinges on a sample and is scattered into a detector placed at an angle θ with respect to the transmitted beam[69]. The waves of the scattered light coming from randomly distributed particles might be out of phase (destructive interference), or they can be in phase (constructive interference) and illuminate the detector. [69,75]. As a result, at any instant the detector will exhibit bright (illuminated) and dark areas (see Figure 1.6 A), hereafter referred to as a scattering pattern

Due to Brownian motion the positions of the particles are randomly changing, consequently the bright areas in the scattering pattern will also change in both intensity and position. This fluctuation of the scattered light is used to estimate the sample size distribution[69].

An autocorrelation function relates a system property to itself along time, varying between a perfect correlation (correlation = 1) to no correlation (correlation = 0). By analyzing the changes in the scattering pattern (the system property) the DLS apparatus defines an autocorrelation function for the sample being measured. In Figure 1.6 B two hypothetical autocorrelation functions are depicted for particles differing in size. Smaller particles move faster, the scattering pattern changes faster, and the decay rate (Γ) of the correlation function is larger. In a DLS experiment the decay rates for a number of size classes are extracted to produce a size distribution (Cummulants and CONTIN are the most popular methods to do so)[69,70,75,78].

The decay rates depend on the particle size, more precisely on the particle's diffusion coefficient (D_{dif}), the latter are obtained by Eq. 5 [70,78], and these are ultimately used to obtain the hydrodynamic diameters using the Stokes-Einstein equation (Eq.7)[70,78]:

$$\Gamma = D_{dif} q^2 \qquad \text{Eq.5}$$

$$q = \frac{4 n_{med} \pi}{\lambda} \sin\left(\frac{\theta}{2}\right) \qquad \text{Eq.6}$$

$$D_{dif} = \frac{\kappa T}{6 \pi \eta R_H} \qquad \text{Eq.7}$$

where R_H is the hydrodynamic radius, η is the dispersant viscosity, κ the Boltzman constant and T the absolute temperature[70,78]. Depending on the equipment and the quality of the preparation, the range of detection of the R_H varies from 0.6 nm to 60 μm [70].

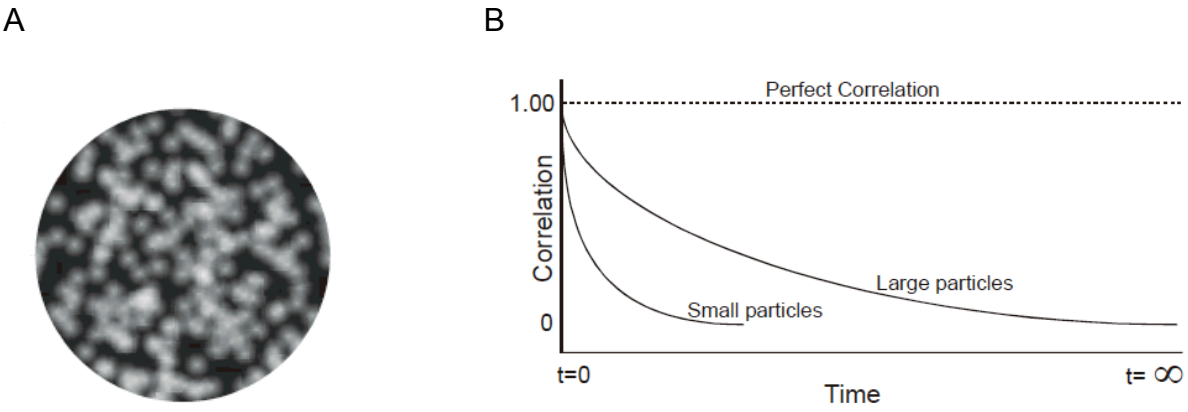

Figure 1.6 Explaining DLS. (A) Scattering pattern that would be seen in a screen detector containing bright areas produced by the constructive interferences from the scattered light by an ensemble of stationary particles in the path of an incident light beam and dark areas were no sign of scattered light is detected. (B) DLS autocorrelation functions for two hypothetical particles differing only in size. Adapted from Ref.[75].

In the instrument used in this work, a Malvern Zetasizer Nano ZS, R_H is given by the parameter Z-average. This value is comparable with other methods of analysis of spherical particles if only one peak is obtained with a reasonably narrow distribution in the correct dispersant. This degree

of polydispersity is evaluated by other instrument-retrieved parameter, the polydispersity index (PdI). A PdI of 0.1 is indicated by the manufacturer as being expectable for narrow monodisperse samples[75]. It should be noted that a value of 0.3 is more commonly used in practical bionanotechnological applications[27,79]. For broad distributions where the PdI is over 0.5, the manufacturer indicates that it is unwise to rely on the Z-Average, and the peak of the size distribution should be used instead. This size distribution is obtained from the scattering intensities, but it can also be plotted as a number distribution. It should be noted that according to Eq.4, larger particles scatter more light, as a consequence the peak values from these distributions might not be the same[75].

3.3. Plasmon resonances and UV-Vis spectroscopy

3.3.1. Theory of plasmon resonances

The relevant concepts will be presented in a way to favor the intuitive understanding of the phenomena, as the topics of metallic NPs is too complex to be fully described here[71,72,73,76,77,80,81,82,83,84,85,86,87,88]. The term plasmon indicates that the electrons are free to migrate in the metal in a manner similar to that of ions in "gaseous" plasma. The term surface plasmon polariton (SPP) has been suggested to describe optically induced electron oscillations, however the term surface plasmons (SP) is now commonly used with the same meaning[80]. Depending on the boundary conditions it is commonly accepted to distinguish bulk plasmons (3D plasma), surface propagating plasmons or SPP (2D films), and localized surface plasmons or LSP (nanoparticles)[87], see Figure 1.7.

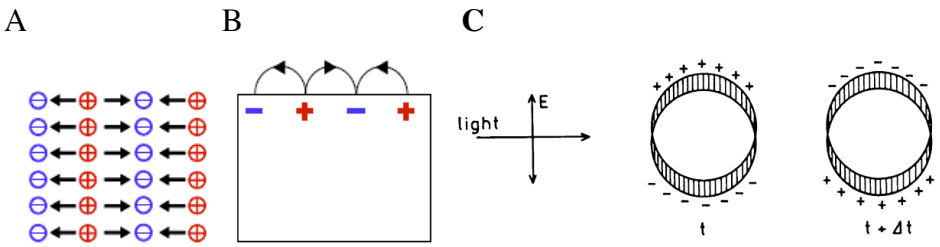

Figure 1.7 Schematic representations of the different plasmons. (A) Bulk plasmon (3D plasma), (B) surface propagating plasmon or SPP (2D films), arrows indicate the electrons oscillation; and (C) localized surface plasmon (nanoparticles), where the horizontal arrow indicates the direction of light propagation and the vertical arrow indicates the direction of the electric field, which is by definition perpendicular to the propagating direction. (A) and (B) Adapted from[87], (C) adapted from[80].

Being a collective oscillation plasmons can be described as a quantum of plasmon oscillation[77], in bulk plasmons this oscillation occurs at the plasma frequency, being ~10eV for gold[87].

In LSP the electric field displaces the free (conductive) electrons from their equilibrium position, creating a charge separation, electron *vs* ionic core, at the nanoparticle surface (Figure 1.7 C) the resulting charge polarization produces the main restoring force, with the oscillation occurring at a well defined frequency in the visible range for AuNP, the LSP resonance (LSPR)[77,87]. To quantify this frequency we need scattering theory. Mie's equations for extinction, absorption and scattering cross sections are as follows:

$$C_{sca} = \frac{2\pi}{|k|^2}\sum_{L=1}^{\infty}(2L+1)(|a_L|^2 + |b_L|^2) \qquad \text{Eq.8}$$

$$C_{ext} = \frac{2\pi}{|k|^2}\sum_{L=1}^{\infty}(2L+1)\left[\mathrm{Re}(a_L + b_L)\right] \qquad \text{Eq.9}$$

$$C_{abs} = C_{ext} + C_{sca} \qquad \text{Eq.10}$$

where k is the incoming wave vector and L are integers representing the dipole, quadrupole, and higher multipoles of the scattering and *Re* denotes that only the real part should be considered. In the above expressions, a_L and b_L are the parameters obtained by the Riccati-Bessel functions ψ_L and χ_L[77].

These cross section are a measure of the scattering or absorbing (or both) powers of a particle, and can be perceived as an hypothetical area surrounding the particles such that every photon surrounding the particle is scattered or absorbed (or both), respectively[73]. The extinction cross section can be directly correlated to absorbance (A), using ρ, the particles density (particle / cm^{-3}) and l, the optical path length (cm)[73]:

$$A = \rho l C_{ext} / 2.303 \qquad \text{Eq.11}$$

In the Rayleigh scattering range ($R << \lambda$) only the dipole term is relevant, and Mie's scattering agrees with Rayleigh's scattering, with Eq. 9 simplifying to[73,76,77,82]:

$$C_{ext} = \frac{24\pi R^3 \varepsilon_m^{3/2}}{\lambda} \frac{\varepsilon_{im}}{\left(\varepsilon_{re} + 2\varepsilon_{med}\right)^2 + \varepsilon_{im}^2} \quad \text{Eq.12}$$

where ε_{im}, ε_{re} are the imaginary and real parts of the particle's dielectric function and ε_{med} is the dielectric function of the medium. Albeit this approximation is only accurate for very small particles ($R << \lambda$), the predictions of the dielectric sensitivity are still quite accurate for larger particles. In Eq. 12, $\varepsilon_{re} + 2\varepsilon_{med}$ will be minimized when $\varepsilon_{re} = -2\varepsilon_{med}$, and the extinction cross-section will be maximized, explaining the LSPR dependence on ε_{med}[77].This is of major importance in the present work as the shift in the AuNPs LSPR peak wavelength (λ_{LSPR}) will be used as a prof of protein to AuNP conjugation. The LSPR sensitivity *to* ε_{med} is caused by the slope in the real part of gold's dielectric function in the wavelength range depicted in Figure 1.8.

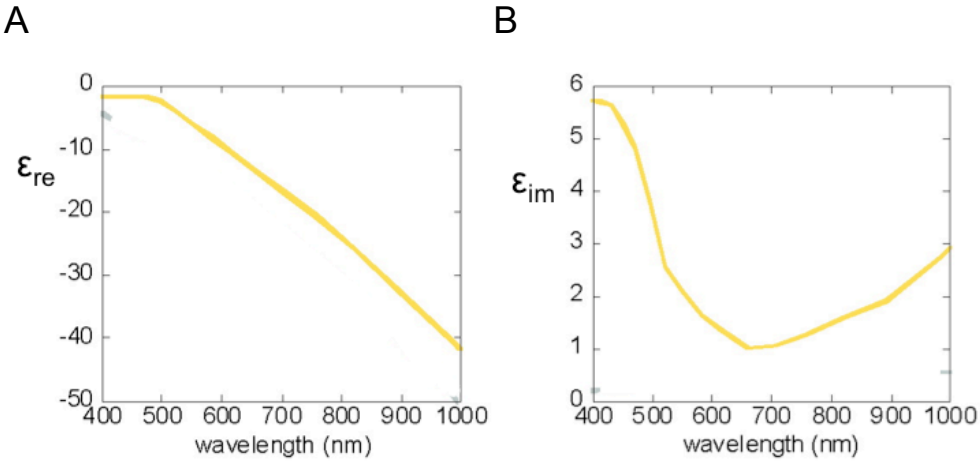

Figure 1.8 Real (A) and imaginary (B) parts of the complex dielectric functions of gold. Adapted from Ref.[77].

The LSPR extinction peak, λ_{LSPR}, can be mathematically related to the medium's dielectric function by[77]:

$$\lambda_{LSPR} = \lambda_p \sqrt{2n_{med}^2 + 1} \quad \text{Eq.13}$$

where λ_p is the wavelength corresponding to the plasma frequency of the bulk metal. While the real part of the particle's dielectric function influences the frequency of the LSPR, the imaginary part is related to the resonance broadening[77]. Tuning the AuNPs size from 10 to 100 nm increases the λ_{LSPR} over 60 nm and the size also influences the resonance line width, due to a combination of intra-band

transitions, which contribute to increased line width for small particles, and higher order (non-dipole) plasmon modes, which contribute to increased line width for larger particles[77]. Other factors affecting the AuNPs optical spectrum are shape and inter-particle distance[77], this last parameter being of major importance to the present work. AuNP aggregation can be induced by the addition of salt or by changing the pH (in case of protonable capping agent). When AuNP begin to aggregate they form pairs of nanoparticles and their optical spectrum acquires a new red-shifted peak in relation to the LSPR. The simplest description of this interaction, the coupling of two nearby oscillators, is the coupling of two nearby dipoles. The interaction energy between the dipole increases with increasing magnitude of the dipole moments and with decreasing inter-particle distance. This interaction energy is strong enough to change the resonant frequencies of the AuNPs, resulting in a red shifted resonance, corresponding to two longitudinally aligned dipoles that give rise to the red shifted band in an optical spectrum[82,89].

3.3.2. UV-Vis spectroscopy

Due to the sensitivity of the AuNP's LSPR to the inter-particle distance and dielectric environment, an UV-Vis spectrum in its most traditional form of A *vs* λ can be used to monitor the colloidal stability and to infer if the protein to AuNP conjugation took place. Aggregation can be detected by the appearance of a second band red-shifted from the LSPR band, and the changes in the dielectric environment at the AuNP surface due to the presence of a protein layer, usually originates a red shift in the LSPR. As sharper LSPR bands arise from more monodisperse samples[88], UV-Vis can also be used to compare the degree of monodispersion of different AuNP syntheses batches. In the case of gold nanoparticles, as both absorption and scattering are responsible for light attenuation, the spectrum of A *vs* λ is more properly called an extinction spectrum.

3.4. Fluorescence and its interactions with metallic surfaces

Fluorescence is a member of the luminescence family of processes where susceptible molecules emit light from electronically excited states created by mechanical (friction), chemical or physical (e.g. absorption of light) mechanism. In this latter case luminescence generated by UV-Vis excitation is called photoluminescence, and can be further divided into fluorescence when emission occurs from the lowest excited state where transitions to the ground state are spin allowed, and phosphorescence when emission occurs from a metastable state bellow the fluorescent state achieved by non-radiative transitions where relaxation to the ground state is spin forbidden. [90,91]

With light absorption a fluorophore is usually excited to some higher vibrational level of S_1 or

S_2, and normally relaxes non-radiativelly to the lowest vibrational level of S_1 -internal conversion- (Figure 1.9). Generally at room temperature (RT), thermal energy is not enough to significantly populate the excited vibrational states, therefore absorption and emission occur mostly from the lowest vibrational states.[92] Typically relaxation occurs to a higher vibrational states of S_0 and then quickly reaches thermal equilibrium.[92] In phosphorescence molecules undergo a spin transition to T_1 (intersystem crossing), before returning to S_0, therefore it is red shifted from fluorescence and its slower because it is spin forbidden[92].

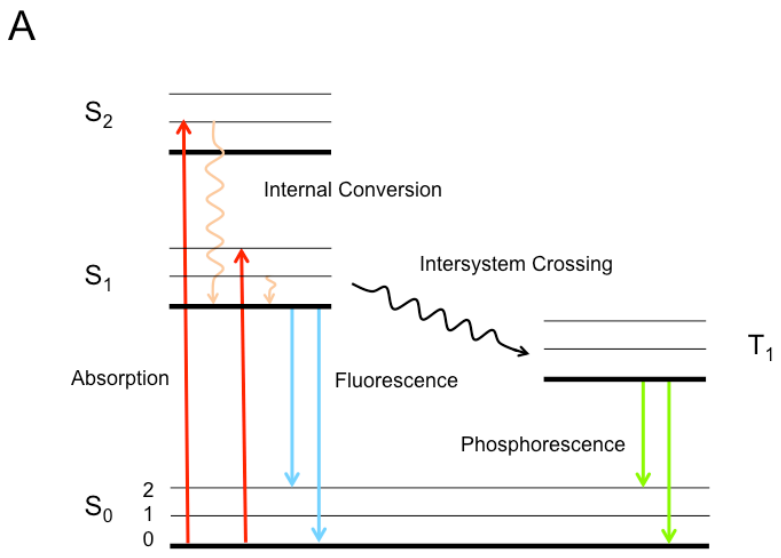

Figure 1.9 Jablonski diagram illustrating key concepts in photoluminescence. The singlet ground state (S_0), first and second electronic excited (S_1 and S_2) and lowest triplet state (T_1) are depicted. Within each electronic level, several vibrational energy levels can exist (0, 1, 2). Radiative transitions are depicted by straight arrows, non-ratiadive transitions by wavy arrows. Absorption (red arrows) can occur to any of the vibrational states of S_1 or S_2, depending on the fluorophore, emission generally occurs from the lowest vibrational state of the lowest excited electronic state, either in fluorescence (blue arrows, from S_1) or phosphorescence (green arrows, from T_1). Adapted from Ref.[92].

Emission is typically red shifted from absorption -Stokes Shift- (Figure 1.9 red and blue arrows), due to several factor including internal conversion, the decay to the higher vibrational levels of S_0, excited state reactions, complex formation, energy transfer and solvent effects.[92]

Excited state electrons might also decay non-radiativelly. The efficiency of radiative decay is measured by the quantum yield (Q), the fraction of fluorophores that decay through emission [92]:

$$Q = \frac{\Gamma}{\Gamma + k_{nr}} \qquad \text{Eq. 14}$$

where Γ and k_{nr} are their radiative and the non-radiative decay rates, respectively. Larger Q means brighter emissions, but no fluorophore has a unitary Q due to Stokes losses[92]. The probability of non-radiative relaxation is higher for fluorophore with higher lifetimes (τ), the average time the molecule spends in the excited state prior relaxation, given by[92]:

$$\tau = \frac{1}{\Gamma + k_{nr}} \qquad \text{Eq. 15}$$

Q and τ can be modified by factors that affect both rate constants (Γ or k_{nr}). A fluorophore is said to be quenched when there is a decreases in the fluorescence emission intensity[92]. This can be due to "non-molecular" mechanisms, such as the attenuation of the incident light by the molecule itself or by other absorbing species; or due to molecular interaction processes as static or collisional quenching, where the quencher forms non-fluorescent complexes with the fluorophore ground state, or the quencher diffusive contacts with the excited state induces non-radiative decay, respectively[92].

In these mechanisms quenching occurs due to the coupling of the electronic orbitals between the molecules. In another quenching mechanisms named Förster resonance energy transfer (FRET), the excited state energy is transmitted by long range dipole-dipole interactions, requiring the donor and acceptor to be in resonance, this is, donor emission and acceptor absorption spectrum overlap [90,93]. FRET is often designated as a "spectroscopic ruler" because there is a distance dependent relationship of the energy transfer rate, providing a microscopic scale to measure separation in vitro[94]. The efficiency of this process (E_{FRET}) depends on the donor to acceptor distance, r, and the Forster radius, R_0 (donor-acceptor distance at which E_{FRET} = 50%)[81,92]:

$$E_{FRET} = \frac{1}{1 + (r / R_o)^6} \qquad \text{Eq. 16}$$

The fact that AuNP's can be used as quenchers at distances up to 25 nm in contrast to the 5-7 nm for traditional quenchers[81], and the fact that 1.4 nm AuNP that show no sign of absorption have high quenching efficiencies towards several organic dyes, suggest that AuNPs do not follow the FRET mechanism. Evidence also exhist for increased quenching efficiencies with increasing spectral overlap promoted by shifting the AuNPs LSPR peak and increasing its intensity[81,95,96].

The quenching efficiency by AuNP has a $1/r^4$ distance dependence different from FRET, this dependence is in agreement with the surface energy transfer mechanism [97] that describes the energy transfer from fluorescent dyes dipole to a metallic surface.[81,98] The efficiency of dipole-surface energy transfer, E_{SET}, expresses as[81]:

$$E_{SET} = \frac{1}{1+(r/d_0)^4} \qquad \text{Eq. 17}$$

wherein, r is the donor-surface distance, while d_0 is the donor-to-surface distance at which the energy transfer efficiency is 50%[81,99].

E_{FRET} depends on $(r/R_0)^6$, R_0 mainly depends on the absorption of acceptor (spectral overlap and dipole orientation), while for dipole–surface energy transfer, E_{SET} depends on $(r/d_0)^4$, d_0 mainly depends on angular frequency and Fermi wave vector of metal[81,92].

The overall length resolution of each method is presented in Figure 1.10[81,99].

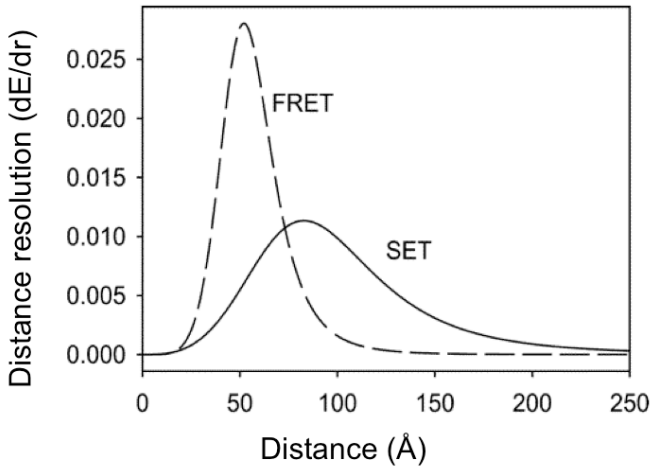

Figure 1.10 Typical separation distance-dependent length resolution of the FRET and SET mechanisms. The first derivative (dE/dr) of the distance dependent efficiency function ($E_{FRET\ or\ SET}$ *vs* r) with respect to the distance (r / Å) is plotted. Adapted from [81,99].

The FRET peak is intense and very narrow, indicating that FRET is very sensitive, but the detection range is very limited, respectively. FRET peak does not extend past 100 Å. The SET curve follows a different trend, being broader and shorter than the FRET curve. Although SET does not have the sensitivity of FRET, it more than makes up for this limitation in both its total usable distance range and its maximum limit of detection. Where FRET resolution essentially drops to insignificance at 100 Å, SET continues to provide similar distance resolution even up to 220 Å. Below 70 Å (the point where SET and FRET have identical resolution), FRET provides the best distance resolution. However, above 70 Å, SET provides better resolution than FRET, and this is clearly the better of the two methods at extremely long distances. Although both SET and FRET rely on dipolar coupling, it is

intuitive to expect SET to have a longer distance dependence due to the cooperative effect of more accessible acceptor dipoles yielding more dipolar interactions. [81,99]

Many details of the fluorophore-metal colloid interactions are not known with certainty, the most important information is that there are probably three dominant interactions of fluorophores with metals, see Figure 1.11[92].

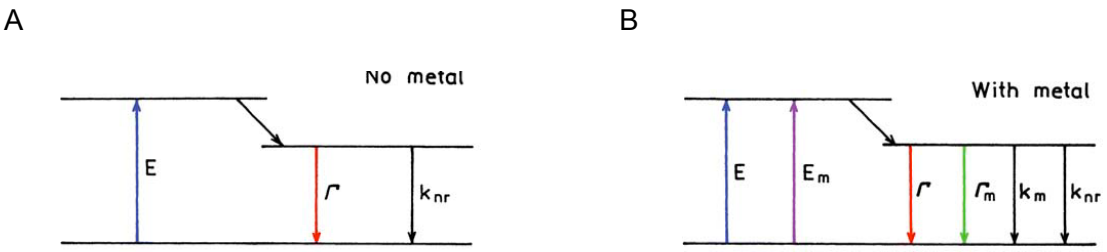

Figure 1.11 Jablonski diagram without (A) and with (B) the effects of nearby metal surfaces on a fluorophore. Adapted from Ref.[82,92].

First, fluorophores might be quenched at short distances from the metal surfaces due to new non-radiative decay routes, causing a decrease in the quantum yield. Considering Eq. 14 we now have, in the presence of the metal surface[92]:

$$Q_m = \frac{\Gamma}{\Gamma + k_{nr} + k_m} \qquad \text{Eq. 18}$$

where Q_m and k_m are the quantum yield and non-radiative decay rate in the presence of the metal surfaces, and k_{nr} is the non-radiative decay rate due to all other non-radiative decay mechanisms.

Then we can have an increased rate of excitation (E_m), due to a more concentrated electric field around the particle, this will increase the brightness without increasing the quantum yield. We now have a rate of excitation with contributions from the incident light (E) and from the nanoparticle's electric field[92]:

$$Excitation\ rate = E_{ex} + E_{ex,m} \qquad \text{Eq. 19}$$

Finally, there can be an increased rate of radiative decay (Γ_m), this will increase the brightness as well as the quantum yield. The quantum yield and lifetime in the presence of the metal surfaces are now given by[92]:

$$Q_m = \frac{\Gamma + \Gamma_m}{\Gamma + \Gamma_m + k_{nr} + k_m} \quad \text{Eq. 20}$$

$$\tau_m = \frac{1}{(\Gamma + \Gamma_m + k_{nr} + k_m)} \quad \text{Eq. 21}$$

Albeit further experiments are necessary to establish the distance dependences of the interactions, according to Lackowitz, the distance of the interactions probably increases, in order, with quenching, increased excitation and increased radiative rate[92]. Regarding the resonant energy transfer mechanism, the important fact is that using AuNP extends the distances for energy transfer up up to 25 nm, as compared to 5-7 nm with organic quenchers. AuNPs also have the advantage of higher quenching efficiency, tunable LSPR, greater chemical and photostability, and nonsusceptibility to photobleaching[81].

3.5. Sedimentation under Stokes conditions and Differential Centrifugal Sedimentation

3.5.1. Differential Centrifugal Sedimentation

DCS has recently gained importance as a nanoparticle size and dispersion characterization technique due to its unmatched resolution[100,101,102]. A CPS Disc Centrifuge was used throughout this work, it is a particle size analyzer with advertised measuring capabilities from 3 nm to 80 µm[100,101]. The analyzer measures particle size distributions using centrifugal sedimentation within an optically clear spinning disc that is filled with fluid. This is done by measuring the time taken for the particles to travel from the center of the disk through a sucrose gradient with defined viscosity to a detector placed at the outer rim of the disk. For materials with homogenous density and simple shape (for example spherical particles) one can directly relate this time to particle size.[100,102]

Smaller particles, as well as less dense materials take more time to sediment. Gold nanoparticles are relatively dense materials (bulk value of 19.3 g cm^{-3}) as compared to liposomes (0.95 g cm^{-3}) or other inorganic particles as silica based nanoparticles (bulk value of 2.2 g cm^{-3}) therefore the time they take to sediment is relatively small, with typical analysis times around five minutes (for the 30 nm particles used in this work).[27,100] Upon binding of proteins to the AuNP surface, their size increases, but at the same time, also the overall particle density decreases. Therefore the time that the particle takes to sediment when conjugated to a protein corona is larger than before conjugation, and, the analytical measured data is equivalent to a decrease in the size of the AuNP protein

conjugates as compared to bare AuNP. The differences in the arrival times, between these density inhomogeneous objects, still allows one to distinguish between them[27,100]. This apparent size decrease can then be corrected taking into account the densities of the material forming the lower density corona around the core AuNP (see Materials and Methods in the Appendix) to obtain an estimation of the protein shell thickness surrounding the particle[27].

3.5.2. Sedimentation under Stokes conditions

For a deeper understanding on how the particle converts the sedimentation time to a size distribution, the theory of sedimentation under Stokes conditions is necessary. The rate of sedimentation inside the rotating disc is controlled by four factors: the size of the particles, the difference in density between the particles and the fluid through which they pass, the viscosity of the fluid, and the strength of the centrifugal field (rotational speed)[100,102].

Sir G. G. Stokes showed that when particles settle in a gravitational field under a certain set of conditions, the forces acting on the particle are in perfect balance, and the particle moves at a constant velocity (which can be predicted) after a very brief period of initial acceleration. The required conditions are[100,102]:

(i) The particle must be smooth, spherical, and rigid enough to not deform due to the forces acting on it.

(ii) The particle must be small compared to the container of fluid

(iii) The particles that make up the fluid must be much smaller than the settling particle, so that the fluid is essentially homogeneous in how it acts on the particle.

(iv) The settling speed must be slow enough that all viscous forces come from smooth (non-turbulent) flow.

These conditions are normally satisfied for most samples run on the DCS apparatus used, CPS Disc Centrifuge, using normal operating parameters. There are two fairly common situations where these conditions are not completely satisfied: (i) Non-spherical particles. They always settle at a rate slower then that of an sphere of equivalent volume; (ii) significant Brownian motion, this broadening has the same probability to occur in any direction, therefore it affects the resolution, a broader peak is seen but not the reported peak size. The smaller the particles and the larger the analysis time, the more extensive this broadening will be[100,102].

If all the conditions specified by Stokes are satisfied, then the viscous drag force acting on the particle is given by[100,102]:

$$Drag\ force = 3\pi D_{NP}\eta V \quad \text{Eq.22}$$

where D_{NP} is the particle diameter, η is the fluid viscosity and V is the settling velocity of the particle. In a constant gravitational field, the gravitational force acting on the particle is given by[100,102]:

$$Gravitational\ force = (\pi/6)D_{NP}^3(\rho_p - \rho_f)g \quad \text{Eq.23}$$

where ρ_p is the particle density, ρ_f is the fluid density, and g is the gravitational acceleration. When the two forces are equal[100,102]:

$$(\pi/6)D_{NP}^3(\rho_p - \rho_f)g = 3\pi D_{NP}\eta V \quad \text{Eq.24}$$

or

$$V = ((\pi/6)D_{NP}^2(\rho_p - \rho_f)g)/(18\eta) \quad \text{Eq.25}$$

The previous equation, Stokes Equation, shows that the velocity of the particle is proportional to the square of the particle diameter, proportional to the difference in density between the particles and the fluid, proportional to the gravitational acceleration, and inversely proportional to the fluid viscosity. The time (t) required for the particle to move from the surface of the fluid to a distance X below the surface is given by[100,102]:

$$t = X/V = (X18\eta)/(D_{NP}^2(\rho_p - \rho_f)g) \quad \text{Eq.26}$$

Rearranging the previous equation into Eq. 27, one can see that the diameter of a particle can be determined by measuring the time required to sediment a known distance:

$$D_{NP} = (X18\eta)/(t(\rho_p - \rho_f)g)^{1/2} \quad \text{Eq.27}$$

as all of the parameters in Eq. 27 are constant during a sedimentation (except for D_{NP} and t), Eq. 27 can be restated as[100,102]:

$$D_{NP} = K/t^{1/2} \quad \text{Eq.28}$$

where K is a combination of constants from Eq27. Of course, inside the Disc Centrifuge the centrifugal acceleration replaces the gravitational field. The centrifugal acceleration increases as the particles move from the surface of the liquid toward the outside edge of the disc chamber, because the radius of rotation increases as the particle moves outward. And then we have[100,102]:

$$Centrifugal\ Acceleration = \omega^2 R_{rot} \qquad \text{Eq.29}$$

where ω is the rotational speed in radians and R_{rot} is the radius of rotation. This value for acceleration is substituted for 'g' in Eq.25 [100,102]:

$$V = (D_{NP}^2(\rho_p - \rho_f)\omega^2 R_{rot}) / (18\eta) \qquad \text{Eq.30}$$

The settling velocity "V" can be restated as the first derivative of the distance from the center of rotation with time[100,102]:

$$\frac{\delta R}{\delta t} = (D_{NP}^2(\rho_p - \rho_f)\omega^2 R_{rot}) / (18\eta) \qquad \text{Eq.31}$$

This differential equation can be rearranged to separate variables, and then integrated to get a solution for settling time as a function of the starting radius ($R_{rot,o}$), the ending radius ($R_{rot,f}$) [103], and several constants[100,102]:

$$\frac{\delta R}{R_{rot}} = (D_{NP}^2(\rho_p - \rho_f)\omega^2) / (18\eta)\delta t \qquad \text{Eq.32}$$

$$\int \frac{\delta R}{R_{rot}} = (D_{NP}^2(\rho_p - \rho_f)\omega^2) / (18\eta) \int \delta t \qquad \text{Eq.33}$$

$$\ln \frac{R_{rot,f}}{R_{rot,o}} = ((D_{NP}^2(\rho_p - \rho_f)\omega^2) / (18\eta))t \qquad \text{Eq.34}$$

Eq. 34 can be rearranged to the same form as Equation 28[100,102]:

$$D_{NP} = ((18\eta \ln(R_{rot,f} / R_{rot,o})) / ((\rho_p - \rho_f)\omega^2))^{1/2} / t^{1/2} \qquad \text{Eq.35}$$

or:

$$D_{NP} = K / t^{1/2} \qquad \text{Eq.28}$$

Even though the conditions within the disc centrifuge are quite different from sedimentation with gravity, the same type of simple equation describes both processes. The DCS software uses the sedimentation time for a calibration standard of known diameter to precisely determine the value of *K* in Equation 28, therefore a calibration standard is run before any sample analysis, in this way, the accuracy of each particle size distribution is assured. The exact values for the individual constants in Equation 28 do not need to be determined, since it is only the combined constant *K* that must be known[100,102].

As the particles move towards the outer edge of the disc, they pass through the detector light beam, and the intensity of the light that reaches the detector is reduced by the particles. Using Mie theory of light scattering, the DCS software generates a particle size distribution by calculating the weight of material at each size based upon the elapsed time of sedimentation, the light absorption, and the efficiency of light scattering by the particles as a function of particle diameter[100,102].

The calculated distribution will be accurate as long as the particles are spherical (or nearly spherical) and as long as the refractive index of the particles and fluid and the absorption constant for the particles are accurate. If these values are not known accurately, the accuracy of the reported distribution will be reduced but the CPS Disc Centrifuge will continue to give accurate relative distributions[100,102].

3.5.3. Function of the density gradient

The Stokes equation applies to individual particles that are settling in a fluid. However, a sample injected into the disc is not a single particle, but rather millions of individual particles suspended in a fluid. If you attempt to operate the Disc Centrifuge using a homogeneous fluid (for example, water) inside the disc, and inject a sample of particles suspended in water, then the analysis always fails, and no information about the particle size distribution is collected.[100,102] The analysis fails because a suspension of more dense particles in a less dense fluid makes the suspension behave like a fluid of higher density, rather than like individual particles suspended in a fluid of lower density. For example, if one measures the density of a 50% (by weight) emulsion of polymethyl methacrylate in water, the measured density is not the density of water, but rather the average density of water and polymethyl methacrylate. A hydrometer will show the density of the latex is much higher than water. When adding a drop of this latex to a container of water, the drop will rapidly fall through the water

toward the bottom of the container, leaving a stream of particles behind as it falls (due to some mixing of particles into the bulk water). The drop settles very rapidly, not at all according to the size of the particles that make up the emulsion, but rather only according to the apparent density of the emulsion relative to water.[100,102]

The bulk settling of a suspension as if it were a homogeneous fluid is called "streaming"; streaming makes measurement of the particle size distribution impossible.

The density gradient that is used in the CPS Disc Centrifuge counteracts the destabilizing effect of higher apparent density in the sample. The sedimentation of particles inside the disc will be stable if (and only if) the apparent density of the fluid inside the disc increases continuously from the surface of the fluid to the outside edge of the disc at all times during the analysis. This requirement is stated by the following equation[100,102]:

$$\frac{\delta \rho_f}{\delta R_{rot}} \geq 0 \qquad \text{Eq.36}$$

where ρ_f is the apparent density of the fluid.

The density gradient that is established inside the disc allows Equation 36 to be satisfied during the analysis. When a very dilute sample is injected onto the surface of the fluid inside the disc, the apparent density of the sample could be slightly higher than the fluid at the surface of the fluid in the disc, but the fluid just under the surface is also higher in density (due to the density gradient), so there is no instability.[100,102] The particles sediment according to the Stokes Equation, and the there is no significant "streaming" of the sample during the analysis[100,102].

3.6. Agarose Gel Electrophoresis

Agarose Gel Electrophoresis (AGE) is classical technique for biomolecule analysis[104]. It is a relatively new strategy for the characterization of NP[105,106,107] and their conjugates with biomolecules, including nucleic acids[108,109] and proteins[110]. Agarose gels have larger pores, are easier to prepare and free from toxic components as compared to acrylamide gels[104]. In electrophoretic experiments, particles, biomolecules or in this case the AuNP to protein conjugates, migrate towards the opposite charged electrode. Different particles migrate at different velocities according to[104]:

$$v = \frac{Eq}{f} \qquad \text{Eq.37}$$

where v is the velocity, E is the electric field, q is the net charge of the molecule and f is the frictional resistance to mobility of the particle, this last parameter depends on the mass of the particle, its shape, the buffers viscosity and the matrix porosity. For the AuNPs to protein conjugates used in the present work, keeping the same experimental conditions, the negatively charged AuNP will migrate at slower velocities with increasing amounts of proteins as q will decrease and the size of the conjugates will also increase leading to an increase in f[104].

Chapter II

Materials and methods

In this chapter the experimental procedures are concisely presented, with the detail considered necessary to allow the reproduction of the results. Identification of equipment suppliers is presented where necessary. Unless otherwise stated reactants were from Sigma-Aldrich-Fluka, and were of the highest purity available.

4. Overexpression and purification of the recombinant PfHsp70

The Ag used in this work, *Pf*Hsp70, was heterologously expressed as in *E.coli* RosettaBlue™ cells,[103,111] (Novagen, Germany) as a recombinant fusion protein, with pQE30 being the vector and 6xHis being the fusion Tag.[112] The pQE30/*Pf*Hsp70 plasmid was a kind gift from Prof. Gregory Blatch, Rhodes University, South Africa, and was the same used in the work reported by Matambo *et al.*[112]. *E.coli* RosettaBlue™ cells carry a resistance marker in their genome for tetracycline (Tet),[111] and the pRARE plasmid used for enhanced expression of eukaryotic proteins that contain codons rarely used in *E. coli*, with a chloramphenicol (Cmp) resistance marker,[111] and the plasmid pQE30/*Pf*Hsp70 with the inserted DNA sequence of the *Pf*Hsp70 protein with a N-terminal $(His)_6$ Tag and an ampicilline [113] resistance marker[112].

Plasmodium falciparum has an extremely AT-rich genome (80% AT; 15,16) and heterologous overexpression of *P. falciparum* genes in *Escherichia coli* has been difficult because of rare codon usage (commonly referred as "codon bias").[112,114] Baca and Hol [114] engineered a plasmid that encodes tRNAs for rare codons, in particular arginine (R) (AGA/AGG), isoleucine (I) (AUA), and glycine (G) (GGA) and therefore the plasmid is referred to as RIG. This plasmid was shown to facilitate the heterologous production of full-length *P. falciparum* proteins in *E. coli* [114], including PfHsp70 using the plasmid pQE30/*Pf*Hsp70[112].

E.coli RosettaBlue™ cells [103,111] carry an enhanced version of pRIG, pRARE, encoding tRNA genes for all the "problematic" rarely used codons including Leu and Pro tRNA genes besides those for Arg, Ile and Gly present in the pRIG.[103,111] As an enhanced version of the pRIG plasmid used in the work of Matambo *et al.*, pRARE should allow the expression of full length *Pf*Hsp70 using the pQE30/*Pf*Hsp70 plasmid (constructed and used by Matambo et al.[112]), although it was not previously tested. *E.coli* cells used by Matambo *et al.* were also of a different strain, namely *E. coli* XL 1 Blue, from Stratagene.

According Dr. Gonçalo Doria and Bassem Guirgis, FCTUNL, Portugal, transformation was performed based on the manufacturer's protocol,[111] briefly, 10 ng of pQE30/PfHsp70 plasmid were added to 20 µL of RosettaBlue™ cells and incubated on ice for 5 minutes. The reactions were heat shocked at 42 ºC for 30 seconds and placed on ice for further 2 minutes. Eighty microliters of SOC medium (Super Optimal Broth medium (SOB) with catabolite repression, i.e., it is SOB with glucose, resulting in higher transformation efficiencies of plasmids [115]) were added to each reaction and incubated at 37°C while shaking at 250 rpm for 1 hour. Selection of transformants was accomplished by resistance to antibiotic with an appropriate volume of each reaction plated onto Luria Broth (LB) agar media[116] containing ampicillin, chloramphenicol and tetracycline at final concentrations of 100 $\mu g.mL^{-1}$, 34 $\mu g.mL^{-1}$ and 12.5 $\mu g.ml^{-1}$, respectively, and incubated overnight at 37 ºC.

Large scale production was performed according to Matambo *et al.*,[112] with slight modifications: stock cultures in 30% glycerol cryopreserved at -80ºC for long term storage (Glycerol 87 %, p.a., Panreac, 122329.1211, Barcelona, Spain)) were used to grow bacterial colonies on LB agar plates (LB Agar Miller for microbiology, Merck KGaA, 1.10283.0500, Darmstadt, Germany) with 100 μg/mL of Ampicilin, 34 μg/mL of Chloramphenicol, 12.5 μg/mL of Tetracycline. Isolated colonies on agar plates (stored at 4ºC) were used to prepare 50 mL of overnight LB cultures, 10 g /L bactotryptone (BactoTM Tryptone, pancreatic digest of casein, Becton, Dickinson and Co. (BD), 211705, Le Point de Claix, France), 5 g / L bactoyeast extract (BactoTM Yeast Extract, extract of autolysed yeast cells Dickinson and Co. (BD), 212705, Le Point de Claix, France) and 10 g/L NaCl, with the same concentrations of antibiotics as described previously. These where further diluted (1:100) into 2 L of fresh broth (8x250 mL containers) and allowed to grow until mid-log phase, OD600 ≈ 0.5, at this point production of the Ag was induced with isopropyl-1-thio-B-D-galactopyranoside (IPTG), with final concentration of 1 mM, (IPTG, 99 %, dioxan free, NZYTech, genes and enzymes, MB02602, Lisboa, Portugal) and then allowed to grow overnight. All growths were performed at 37ºC, broth cultures were incubated on an orbital shaker at 150-210 rpm.

All purification procedures were performed at 4 ºC. Since the expressed Ag has a 6xHis-tag at its N-terminus, a chromatography column packed with Ni-NTA resin (Qiagen, Germany) was used as the method for its purification from the bacterial crude extract.[117]

Cells were harvested (30 min, 14 000 rpm, Beckman Coulter Avanti J26-XPI Centrifuge, JA10 Rotor) in 8 x 500 mL Beckman centrifugation tubes and resuspended in 20 mL of lysis buffer, 8M Urea, 300 mM NaCl, 10 mM Imidazole, 10 mM Tris, pH 8.0, 1 mM lysozime, and 800 uL of protease inhibitor cocktail (a tablet per 2 mL of milli-Q water), then a small amount of DNAse was added and the cells were homogenized, afterwards a French press (French pressure cell press, Thermo Electron Corporation, Germany) was used to mechanically break the cells (2000 psi gauge pressure, 3 cycles). Cell debris was removed by centrifugation (Eppendorff centrifuge, 501R, 4 200 x g for 90 min) and the supernatant was collected (~20 mL) and added to 10 mL of the Ni-NTA agarose resin, previously equilibrated with washing buffer (10 mM imidazole, 300 mM NaCl, 10 mM Tris pH 8.0, 800 μL protease inhibitor cocktail / mL buffer), in a glass container and left at 4ºC with gentle shaking for 90 min. The resin was transferred into the column with additional 20 mL of washing buffer used to remove the residual resin in the container. Washing buffer was used to remove non-specifically bound proteins (OD at 280 nm consistently below 0.1, washing buffer as baseline, with ~10 mL collected per tube) and elution buffer (100 mM imidazole, 300 mM NaCl, 10 mM Tris pH 8.0, 800 μL protease inhibitor cocktail / mL buffer) was used to remove the histidine tagged *Pf*Hsp70 protein (OD at 280 nm consistently bellow 0.1, with elution buffer as baseline, with ~10 mL collected per tube). Aliquots were stored at -20ºC until further treatment.

Ni-NTA Agarose resin was regenerated after long term storage (wash with 1 column volume milli-Q, 5 volumes of 100 mM EDTA, pH 8.0, 1 volume milli-Q, regenerate with 2 volumes of 100 mM $NiSO_4$, equilibrate with 2 volumes of washing buffer), and washed after use with 10 volumes of NaOH, 0.5 M, and then 5 volumes 30 % ethanol were added to avoid microorganism growth. For short-term storage up to a week, washing buffer was used.

Buffer exchange was necessary as imidazole might induce aggregation.[118] Amicon ultrafiltration system (Amicon, Millipore) with ultrafiltration membranes (Millipore, MWCO 30 KDa) or Centricons (MWCO 30 KDa, Amicon-ultra, Millipore) were used to exchange the elution buffer to Phosphate Buffered Saline (PBS, pH 7.4, 10 mM phosphate buffer, 137 mM NaCl, 2.7 mM KCl) by 3 cycles of protein concentration and addition PBS (concentration to $1/20^{th}$ of the initial volume followed by restoring the volume to the initial value with PBS). Protein purity was confirmed by 10% Sodium DodecylaureylSulfate Polyacrylamide Gel Electrophoresis (SDS-PAGE) and by Western blot analysis using the 2E6 antibody. Buffer exchanged aliquots were stored at -20ºC, with no addition of preservatives or cryoprotective agents, e.g. glycerol.

5. Purification of the anti-*Pf*Hsp70 monoclonal antibody

According to Dr. Miguel Prudêncio and Dr. Cláudia Cunha, IMM, Portugal, antibody production was performed as follows: an hybridoma culture was grown using standard scale-up culturing conditions to produce 2.6 L of culture containing the monoclonal Ab[119]. Protein precipitation was performed using 50% w/v ammonium sulfate solution at 4ºC. The precipitate was collected by centrifugation and resuspended in PBS and excess salts were removed by 2x overnight dialysis in dialysis tubing (Medicell International, UK; pore size 12-14 kDa) against PBS. After dialysis, 100 ml of impure Ab-containing solution was obtained. The solution was centrifuged at 10,000 rpm for 30 min at 4ºC to remove any precipitates and the supernatant was concentrated to 35 ml by ultrafiltration with gentle mixing at 4ºC (cut-off value of membrane 30 kDa).

Purification of 2E6 antibody was performed using Protein G sepharose affinity chromatography with Protein G HP Spin Trap columns[120] (GE Helathcare, 28-9031-34, Bukinghamshire, UK) or Protein G Sepharose 4 Fast Flow[121] (GE Healthcare, 17-0618-01, Upsala, SE). The loaded amounts of impure antibody were bellow the maximal binding capacity to minimize losses. The collected solution was concentrated by ultrafiltration (30 KDa MWCO, Amicon, Millipore) and the buffer was exchanged by 5 cycles of centrifugation and PBS addition (as previously described).

Protein G HP Spin Trap consists of pre-packed columns of Protein G from GE (lacks the albumin binding sites to avoid undesirable cross-reactions with albumin) immobilized by N-Hydroxysuccinimide (NHS) chemistry on a matrix of highly cross-linked, 6%, agarose microparticles, average size 34 µm. Protein G Sepharose 4 Fast Flow consists of Protein G from GE immobilized by

the CNBr method to Sepharose 4 Fast flow (a matrix of spherical, average size 90 µm, highly cross-linked, 4 %, agarose microparticles).

Protein G HP Spin Trap columns were used as follows, according to manufacturer instructions [120]: all centrifugations using spin columns were performed at 150 x g for 1 min. The columns were equilibrated with 600 µL binding solution (20mM sodium phosphate; pH = 7). About 100 µL of the impure Ab and 300 µL of binding solution were mixed and added to the spin columns, followed by mixing by inversion for 8 min. The columns were then washed twice with binding buffer. Finally, elution was performed twice by adding 400 µL of elution buffer (glycine HCl 0.1M pH = 2.7), mixing by inversion for 1 min and centrifuging into collection tubes containing 30 µL of neutralizing solution (Tris-HCl buffer 1M; pH = 9). Washing twice with binding buffer regenerated the columns, storage was performed with 20 % ethanol.

According to Isabel Silva, Protein G Sepharose 4 Fast Flow was used as follows, based on manufacturer instructions [121]: 10 mL of the resin were added into a cylindrical plastic columns and equilibrated with 5 to 10 column volumes of binding buffer (20 mM, sodium phosphate, pH 7.0), then 3 mL of the impure antibody solution were added to the column and washing was performed with binding buffer until the OD at 280 nm was consistently bellow 0.1. Elution was performed with elution buffer (0.1 M Glycine-HCl, pH 2.7) and neutralization of the eluate was performed by adding 60-200 µL of neutralizing buffer (1M Tris-HCl, pH 9.0) *per* mL of eluate. Columns were regenerated after elution by washing with elution buffer, 2-3 column volumes, followed by washing with binding buffer, 2-3 column volumes, storage was performed in 20 % ethanol, at 4ºC.

To determine the purity of the Ab, samples were analyzed on a 12 % SDS-PAGE. The samples were prepared by mixing 10 µL of sample with 20 µL sample and boiled at 100ºC for a few minutes. Samples were loaded into the gel and run at 215 V during approximately 50 min, with a Tris-Glycine buffer-system and a BioRad power supply.

6. Synthesis and surface modification of gold nanoparticles

Gold nanoparticle synthesis was performed according to the Turkevich method with slight modification[122,123]. All glassware was cleaned with *acqua regia* followed by extensive washing with milliQ water prior to use. A solution containing 62.5 mL of milliQ water and 43 µL of a 30% wt gold salt solution was heated until boiling under reflux in a round bottomed flask, using a sand-bath, at this point 6.25 mL of sodium citrate solution (36.8 mM) was quickly added. After this addition, the solution changed from the gold complex characteristic yellow solution to colorless, then black (possibly described as dark blue) and finally red (see Figure 2.1). Heating and stirring was continued for another 15 minutes, at this point the nanoparticle colloid was allowed to cool down to RT. Only

after this the solution was characterized by UV-Vis and stored at 4ºC until further use. The procedure was performed under vigorous stirring using a magnetic stirrer.

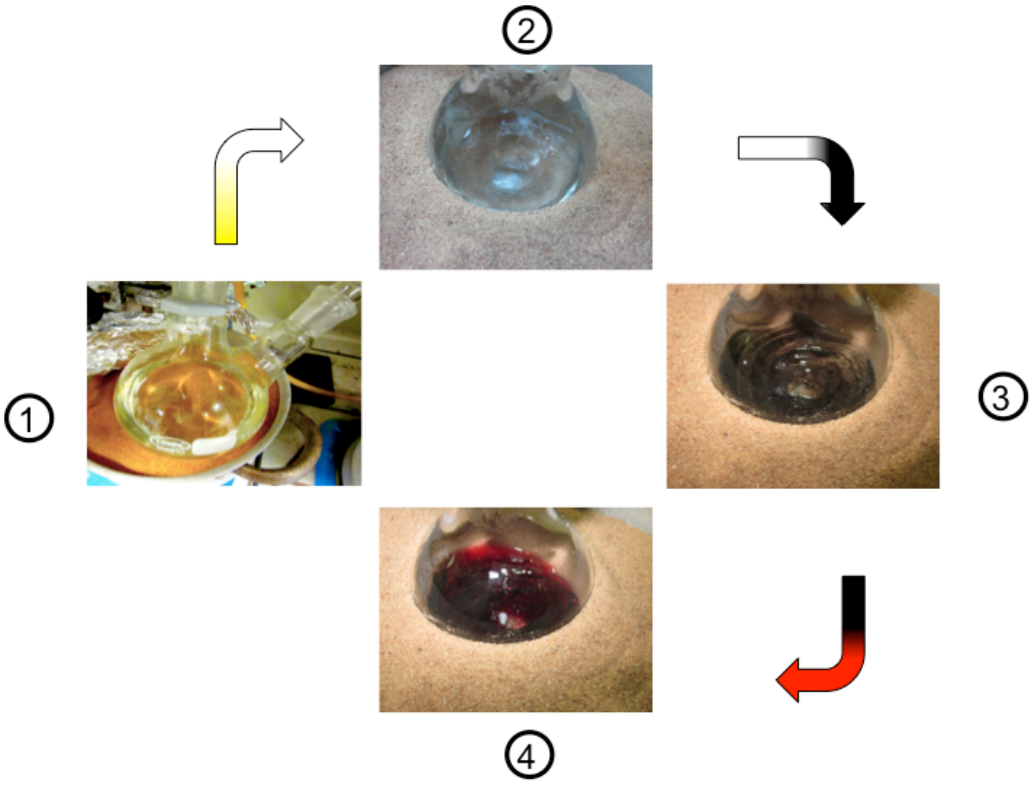

Figure 2.1 Color changes during homemade-AuNP synthesis. The initial gold (III) solution (1) turns into a colorless solution after addition of citrate (2). From this point the solution turns black/dark blue and (3) finally red (4), indicating the formation of a gold nanoparticle colloid.

To change the surface chemistry of the AuNP, citrate, the capping agent used in the synthesis of the homemade-AuNP was place exchanged with mercaptoundecanoic acid (MUA) or with the pentapeptides CALKK or CALNX, where X=D,N,S. These molecules contain thiol groups with higher affinity for the gold surface than the citrate's carboxylic groups. In a typical procedure, an appropriate volume of 1 mM of MUA (etanolic solution) was added to the AuNP colloid at a molar ratio of MUA to AuNP of 120, and allowed to incubate overnight at 4ºC. Pentapetides were in aqueous solution. When the influence of different molar ratios of MUA was studied, both 100 mM and 1 mM MUA ethanolic stock solutions were used and the final ethanol percentage (V/V) was kept constantly equal to 1% by adding absolute ethanol along with the MUA ethanolic solution. No changes in the colloid stability were detected, even in the control solution, where ethanol was added without MUA.

Commercial-AuNP consisted of a citrate-stabilized[124] gold colloid with 30 nm diameter (nominal value) purchased from British BioCell International (BBI, Cardiff, UK) and were used without further treatment. Only MUA place exchange was performed.

7. Antibody conjugation to gold nanoparticles and BSA blocking

In a typical experiment, to 2 mL of a 0.67 nM home made-AuNP functionalized with MUA (MUA to AuNP molar ratio of 360), 2 mL of an antibody solution were added and allowed to incubate overnight, at 4ºC. Different antibody to AuNP molar ratios, ranging from 15 to 1200, were prepared by diluting the antibody stock solution in phosphate buffer (PB, 5 mM, pH 7.2).

To prepare the cross-linked conjugates, stock solutions of EDC and NHS[125,126], 280 and 120 mM respectively, were prepared by dissolving the respective salts in milli-Q water and were added to the antibody solutions (keeping the final volume of antibody solution equal to 2 mL) to a final NHS and EDC to MUA molar ratios of 10 and 23.3, respectively. Incubation was performed for two hours at RT.

BSA blocking was performed to avoid non-specific antigen binding to the AuNP@Ab conjugates. In a typical experiment 2 mL of BSA (3 μM in PB) were added to 2 mL of 2 nM conjugates at an [BSA]/[AuNP]=1500, and incubation was performed for 30 minutes at RT. This solution was diluted to 30 mL with PB and excess BSA was removed by centrifugation (5205 g, 90 minutes, 4ºC), followed by pellet resuspension in PB for a final 0.28 nM AuNP@Ab concentration.

For the commercial AuNP, in a typical experiment antibody conjugation experiment, to 2 mL of a 0.56 nM gold nanoparticle colloid, 2 mL of an antibody solution were added and allowed to incubate overnight, at 4ºC. Different antibody to AuNP molar ratios were prepared by diluting the Ab stock solution in PB. BSA blocking was performed by adding 2 mL of BSA 1.4 μM to 2 mL of AuNP@Ab 0.28 nM, without further PB dilution prior to washing.

8. UV-Vis Spectroscopy

UV-Vis spectroscopy was used for acquiring AuNP extinction spectra. These allowed the comparison of band broadness, calculation of aggregation ratios related to the colloidal stability, and detection of LSPR shifts upon conjugation.

Additionally, UV-Vis spectroscopy was used to estimate the size and concentration of the AuNP. A method reported by Haiss et al.[127] was used. To this end the ratio between the AuNP absorption at the SPR maximum and at 450 nm was used to obtain the size of the gold nanoparticles, this size corresponded to a certain molar extinction coefficient ($M^{-1}cm^{-1}$) that was used to estimate the concentration of the AuNPs.

UV-Vis spectroscopy was also used to follow the bacterial growth curves by monitoring the absorbance at 600 nm, to quantify protein content through the BCA assay method, and to monitor chromatographic purification of the Ag, by measuring the absorbance at 280 nm.

UV-Vis spectra were recorded using quartz cells with 1 cm path length (Hellma, Germany), in

the 200 to 800 nm range using an UV-Vis spectrophotometer from UNICAM (model UV2) or Cary (model Cary 50 version 3.0 or model 6000i version 1.12).

9. Differential centrifugal sedimentation

DCS measurements were performed with a CPS Disc Centrifuge (model DC24000, CPS Instruments, Florida, USA) at 22000 rpm, using a 8-24 % sucrose gradient and 0.37 μm PVP particles as internal calibrators in each measurement. PBS was the sucrose gradient dispersant. The estimation of the protein shell thickness was performed as previously described[27] (see Appendix).

The final reaction volume was 100 μL. All AuNP to antibody incubations and AuNP@Ab to Ag (or Trf or plasma) incubations were performed at RT for at least 2 hours. To prepare the appropriate dilutions of Ag (or Trf or plasma) stock solutions in PBS, where further diluted in PBS. 50 μL of AuNP@Ab (0.28 nM) were added to 20 μL of Ag (at different dilutions from a 1.2 $mg.mL^{-1}$ stock) and 80 μL of PB, in Ag to Ab molar ratios of 120 to 3, correspond to final antigen concentrations from 160 to 4 $\mu g\ mL^{-1}$. To prove the selectivity of Ag binding Trf was used instead of Ag. To assess the influence of Trf as a competitive binder: 50 μL of AuNP@Ab (0.28 nM) were added to 20 μL of Ag (at a Ag to Ab molar ratio of 30), 20 μL of Trf (at Trf to Ag ratios of 1, 2 and 4) and 60 μL of PB. Plasma was used either at a constant concentration, or at increasing concentrations where the natural Trf concentration matched that of the purified Trf concentrations in equivalent experiments. For the assessment of colloidal stability and size increase upon Ab conjugation: commercial AuNP had [AuNP]=0.056 nM and [Ab]/[AuNP]=200, for home made AuNP, [AuNP]=0.67 nM and [Ab]/[AuNP]=300.

10. Dynamic light scattering

Measurements were performed in a Malvern Zetasizer Nano ZS (Malvern, Worcestershire, UK), using disposable plastic cells, with 800 μL of AuNP, at a controlled temperature of 25 ºC, with light detection at 173º, backscatter mode. Each sample was measured at least 3 consecutive times, with each measurement being the average of 20 sub-measurements ("runs"). For commercial AuNP, [AuNP]=0.056 nM and [Ab]/[AuNP]=200, for home made AuNP, [AuNP]=0.67 nM and [Ab]/[AuNP]=300.

11. Agarose gel electrophoresis

Gels were prepared by heating agarose in 50 mL Tris-Acetate-EDTA (TAE) buffer, 0.25 X, pH 8.4, and allowing the gel to form at RT. AuNP conjugates, [AuNP]=0.28nM, were pelleted by centrifugation (20817 g, 4ºC, 15 min), after their pH was adjusted to 12, resuspended in 12 μL of supernatant and mixed with 2 μL glycerol (87%) prior to loading. Unless otherwise stated, 15 wells gels, with 1.0 % agarose, were run at constant voltage of 300 V, with a 15 cm electrode spacing, for 40 minutes, in TAE 0.25 X, using the mini-protean system from BioRad. Digital pictures were acquired with a Canon IXUS 105 digital camera, with a total of 12 Mega Pixels resolution and processed with linear contrast adjustments in order to give a better representation of the visual contrast seen in the gels. The electrophoretic mobility (μ) is defined as the observed rate of migration of a component (ν) divided by electric field strength (E) in a given medium[128]. In the case of agarose gel electrophoresis, a solid support medium, only apparent values can be determined[128]; and, in our case, mobilities are expressed with a negative sign, because migration of particles occurs in the direction opposite to the electrophoretic field. As we aim at comparing conjugates of AuNP with different proteins, in the given conditions of ionic strength, pH, buffer composition, electric field, running time and agarose percentage, apparent electrophoretic mobility values can be calculated to compare the migration of AuNPs run on different gels. The electrophoretic mobility was calculated as follows,

$$\mu = \frac{\nu}{E} \qquad \text{Eq.38}$$

where ν is the observed rate of migration, calculated as the migration distance (obtained with a 0.05 cm resolution) divided by the migration time (1800 s), and E is the electric filed strength calculated as the applied electron motive force (150 V) divided by the electrode separation (15 cm)[107,128,129,130].

All AuNP to Ab incubations and AuNP@Ab to Ag (or Trf) incubations were performed at RT for at least 2 hours. 100 μL of appropriate diluted Ag solutions where added to 300 μL of AuNP@Ab (0.28 nM), in Ag to Ab molar ratios of 49 to 0.095, corresponding to final antigen concentrations from 114 to 0.211 μg mL^{-1}. To prove the selectivity of Ag binding to AuNP@Ab Trf was used instead of Ag. For assessing the influence of Trf as a non-specific competitor in the Ag binding to AuNP@Ab: 100 μL of Ag and 100 μL of Trf were added to 300 μL of AuNP@Ab (0.28 nM), using appropriately diluted solutions to obtain the final Ag or Trf to Ab molar ratios ranging from 49 to 0.095.

For the section on the fluorescence immunoassay development using the commercial-AuNP the differences were: after incubation the conjugates ([AuNP]=0.67 nM, no pH adjustment) were

pelleted by centrifugation (1 hour), resuspended in 27 µL of the supernatant and mixed with 3 µL of glycerol (87%) before loading; Agarose gels, 0.5 %, were prepared with TAE 0.125 X, and run at constant voltage of 150 V, for 30 minutes, in TAE 0.125 X.

12. *Pf*Hsp70 labeling with Cy3B

For the fluorescence competitive immunoassay, using the homemade-AuNP the *Pf*Hsp70 antigen was labeled with Cyanine 3B dye (Cy3B) (Cy3B-N-hidroxisuccinimidine monoester, PA63101I, GE Healthcare, MW=766 $gmol^{-1}$)[131,132]. Cy3B stock solution was 5 $mg.mL^{-1}$ in dimethyl sulfoxide. To 300 µL of purified recombinant *Pf*Hsp70 (3.8 mg/ml or 55 µM in PBS, pH 7.4) 7 µL Cy3B (stock solution) were added, with a Cy3B to PfHsp70 molar ratio of 3:1. Incubation was performed for 2.5 hours at room temperature, in the dark. Excess free dye was removed by ultrafiltration with 40 minutes centrifugation cycles at 10 000 g (3 KDa MWCO, Amicon, Millipore) using PBS as washing buffer. After several washing cycles, the eluted buffer was colorless with the absorbance of Cy3B consistently below 0.05 while the retained protein presented the characteristic pink color from the dye. The Cy3B labeled Ag solution (CyAg) was finally concentrated to 500 µL, this was the stock solution with [Ag]= 2.3 mg mL^{-1} (or 33 µM). The solution of labeled antigen was stored at -20 ºC until further use.

For the section on the molecular-level antigen to AuNP@Ab binding the differences were: to 300 µL of Ag (2.1 mg mL^{-1}) Cy3B (stock solution) was added to a final Cy3B:Hsp70 molar ratio of 10 to1; incubation was performed overnight (at least 10 hours) at 25°C, excess Cy3B was washed (5KDa, MWCO, Amicon, Millipore); and a 1:10 dilution in PBS of the washed CyAg was the stock solution, with [Ag]= 0.21 mg mL^{-1}.

13. Saponin pellets preparation

According to Dr. Miguel Prudêncio and Dr. Cláudia Cunha, IMM, Portugal, *Plasmodium falciparum*-infected RBC cultures were prepared by separating human RBCs by Ficoll gradient from freshly collected buffy coats discarded from blood donations of healthy adults. A *P. falciparum* 3D7 culture was then started by adding parasitized RBC to freshly prepared RBC to a hematocrit of 3% and grown in complete medium. Venous blood collected from a healthy individual in a tube with heparin to prevent blood clotting was used as control.

RBC numbers in infected and non-infected blood samples were normalized to 4.56 x 10^9 cells. RBCs were separated from whole blood samples, treated with saponin and the pellets used to perform

Western blot analysis. Briefly, whole blood was centrifuged at 800 x g for 5 min at 4ºC, plasma was removed and RBCs were washed in PBS followed by lysis in saponin (0.15% in PBS).

14. Western blot

Proteins separated by SDS-PAGE were transferred to nitrocellulose membranes (Schleicher and Schull, BioScience). Membranes were blocked in 5% w/v of non-fat dry milk in PBS containing 0.05% Tween 20 (PBST). After blocking, membranes were incubated with monoclonal 2E6 antibody against *Pf*Hsp70 or anti-actin primary antibody, used as a loading control. Primary antibody binding was detected by using horseradish peroxidase (HRP)-labeled anti-mouse or anti-rabbit IgG.

Antibodies were diluted in 5% w/v of non-fat dry milk in 0.05% PBST and nitrocellulose membranes overlaid with antibodies for 1 hour at RT. The blots were developed by addition of chemiluminescent substrate (SuperSignal West Pico Chemiluminescent Substrate, ThermoScientific). Alternatively, after blocking, membranes were incubated with AuNP@MUA@Ab conjugates (0.83 nM), prepared in the absence of NHS/EDC cross linkers, for 1 hour at RT.

15. Plasma preparation

According to Dr. Marco Monopoli, UCD, Ireland, from 8 to 12 seemingly healthy donors around 50 mL of blood was collected. EDTA treated tubes were inverted 10 times after collection, before centrifugation (at 1200 *g*, 10 minutes, 4ºC) they were turned again 3 times. The supernatant (plasma) was pulled into a 50 mL tube, and kept on ice. Then it was centrifuged again (at 2500 *g*, 15 minutes, 4ºC), the supernatant was aliquoted into 1 mL tubes and stored at -80ºC.

For using the freezed samples, they were allowed to defrost at RT, followed by centrifugation at 1600 *g* for 15 minutes at 15ºC. The supernatant was collected stored in ice and used immediately. Any unused plasma is safely discarded.

16. Fluorescence

For the development of the fluorescence immunoassay with homemade-AuNP, a Cary Eclipse spectrophotometer (Varian, Australia) controlled by the Cary Eclipse software (Version 1.1, Varian, Australia) was used. Emission spectra were recorded in the 500-700 nm range, where the characteristic spectrum of Cy3B is observed, excitation was performed at 480 nm. All samples were

measured in quartz cells with 1 cm optical path length (Hellma, Germany). Measurements were performed at RT. A final reaction volume of 60 μL was used containing 20 μL of BSA blocked conjugates ([AuNP]=0.28 nM, [Ab]/[AuNP]=75), 20 μL of labeled antigen (825 nM) and 20 μL of Ag diluted solutions, the latter were replaced with 20 μL of PBS for blank measurements. In either case, incubation was performed for at least 3 hours at room temperature.

The increase in the fluorescence intensity as related to the blank with increasing analyte concentration was expressed as a relative fluorescence increase (F.Inc. (%)), calculated as follows:

$$F.Inc.\ (\%) = \left(1 - \frac{F.I.Blank}{F.I.Sample}\right) \times 100 \qquad \text{Eq.39}$$

with "F.I. Blank" and "F.I. Sample" being the buffer corrected fluorescence intensities at 574 nm, the Cy3B emission maximum, of the blank (i.e. CyAg incubated with AuNP@Ab) and of the sample containing the Ag, respectively.

For the studies on the Ag to Ab binding at the AuNP surface, using commercial-AuNP, the experimental differences were as follows: a Fluorolog spectrophotometer was used (Fluorolog 3, Horiba Scientific, Japan) and the results were expressed as fluorescence intensity (arb. units) vs [Ag] ($\mu g.mL^{-1}$) .

All AuNP to Ab incubations and AuNP@Ab to Ag (or Trf) incubations were performed at RT for at least 2 hours, CyAg was added after this period, in a total incubation time of 3 hours. To prepare the appropriate dilutions of Ag and Trf (stock solutions in PBS, pH 7.4) where diluted in PBS.

The final reaction volume was 60 μL. Control solutions: 5 μL of AuNP@Ab (0.056 nM) and 5 μL of Cy-Ag (0.21 mg/mL) were added to 50 μL of PB. Analyte solutions: 5 μL of AuNP@Ab, 5 μL of Cy-Ag and 5 μL of Ag (at different dilutions from a 1.2 mg / mL stock) were added to 45 μL of PB. To prove the selectivity of Ag binding to AuNP@Ab Trf was used instead of Ag. For assessing the influence of Trf as a non-specific competitor in the Ag binding to AuNP@Ab, control solutions: prepared as in C; analyte solutions: 5 μL of AuNP, 5 μL of Cy-Ag, 5 μL of Ag (at different dilutions from a 1.2 mg / mL stock) and 5 μL of Trf (at the same concentration as that used for Ag in each analyte solution) were added to 35 μL of PB. Plasma was used either at a constant concentration, or at increasing concentrations where the natural Trf concentration matched that of the purified Trf concentrations in equivalent experiments.

17. SDS-PAGE

For the analysis of the Ag expression and purification (10 % gel), and for Ab purifications (12 % gel) SDS-PAGE was performed. A Biorad power supply was used at a constant voltage of 215 V, for 50 minutes, with 10µL of sample being mixed with 20 µL of sample buffer and heated up for a few minutes in a boiling water bath before loading. For the SDS-PAGE to be used in the Western Blot, the changes in the procedure were as follows: 15 µL of sample and sample buffer were mixed and run on a 12 %, for 1 hour at 180 V.

18. BCA assay

BCA working solution was prepared by mixing stock reagents A and B (1:50 V/V). To 100 µL of the sample or standard solution 500 µL of working reagent were added and allowed to incubate at 60 ºC for 30 min. A calibration curve was obtained with a concentration range from 5 to 25 µg mL^{-1}, by measuring the absorbance at 562 nm. Quartz or polystyrene cells were used. The limit of detection for this protocol, as indicated by the supplier is of 5 $\mu g.mL^{-1}$[133].

19. Peak Fit analysis of the DCS results

The software PeakFit (PeakFit® v4.12, Seasolve Software Inc., San Jose, CA, USA) was used for fitting the DCS weight distribution results with the goal of assessing the agreement between the experimental and the fitted distributions and for a quantitative analysis of the populations present at each experimental condition. The analyzed systems were those where AuNP@Ab with commercial-AuNP were incubated with the Ag, including the kinetic studies as well as the competitive studies with Trf. For this purpose, two Gaussian population distributions representing AuNP@Ab and the AuNP@Ab@Ag were used, using as peak types chromatographic Gaussian areas. Data was automatically fitted using the option: "*Auto PeakFit II: second derivate*", followed by an automatic adjustment of the smoothing ("*AI Expert Smoothing*" an algorithm that seeks to determine the ideal smoothing level to reduce experimental noise), and a graphical (*"Full peak Fit with numerical update")* and numerical (*"Fast Peak Fit with numerical update"*) iterative improvement of the fit. The R^2 for the fitted Gaussians were equal to or higher than 0.99, the automatic fit with baseline subtraction was used when it increased the R^2 values.

Chapter III

Results

In this section a detailed description of the major experimental findings is presented. The results are presented in two subsections describing the results of the experimental work aimed at developing a fluorescence based malarial immunoassay, section 20, and the results for the studies aimed at further understanding the antibody to antigen binding, section 21. Results regarding the production and purification of the antigen and purification of the antibody were included in the first subsection. For clarity, 15 nm diameter homemade-AuNP surface modified with MUA were used in section 20, and 30 nm diameter commercial-AuNP were used in section 21.

20. Gold nanoparticle based fluorescence immunoassay

20.1. Overexpression and purification of the recombinant *Pf*Hsp70

Protein overexpression and purification was performed accordingly to a previously optimized protocol in our laboratory based upon the work of Matambo et al.[112].

SDS-PAGE allowed the analysis of the protein expression products and of the efficiency of the purification steps. Figure 3.1 A presents a typical SDS-PAGE gel of the protein preparations from the various stages of protein purification. The final eluate, containing the specifically bound protein products from the protein expression, typically exhibited an extensive degree of lower molecular weight derivatives of the full length *Pf*Hsp70. SDS was also used to analyze the pattern of protein degradation during the bacterial growth, the aim was to see if decreased extension of protein degradation could be obtained by allowing the bacterial culture to grow shorter or longer times then the typically used overnight growth periods of around 16 hours. From figure 3.1 B, the SDS-PAGE shows that at 62 hours of incubation there is an increase in the extension of the protein degradation (marked by a red asterisk).

In figure 3.1 C, there is presented SDS-PAGE profiles of concentrated purified products on different overproduction and purification experiments. One can see that the extent of degradation seems to be much less in batch V, and full length *Pf*Hsp70 seems quite pure as compared to the intensity of the other visible bands. In fact, this was obtained after a small change in the previously established protocol, were protease inhibitor cocktail was added to the washing and elution buffers, in theory, washing and elution would dilute the inhibitors and their efficiency would decrease abruptly, by using the inhibitor cocktail in the washing and elution buffers, this dilution would be prevented.

As will be presented in section 20.4, the protein antigen (results for batch V are displayed) was also analyzed by Western blot (Figure 3.13), confirming the presence of low molecular weight form of *Pf*Hsp70, but also evidencing that the full length protein is the major component, as seen by the more intense band for the full length protein, as compared to the degradation products.

As mentioned in section 4, the plasmid used to account for the codon bias, pRARE, and the *E. coli* strain used for protein expression were different from the plasmid, pRIG and *E. coli* strain successfully used by Matambo et al. Although the ATPase activity of the Ag -*Pf*Hsp70- was not determined, what would be a proof of retained native conformation, the Ag was successfully expressed in a conformation that could be detected by the Ab used -2E6- and allowed the establishment of an immunoassay (see below).

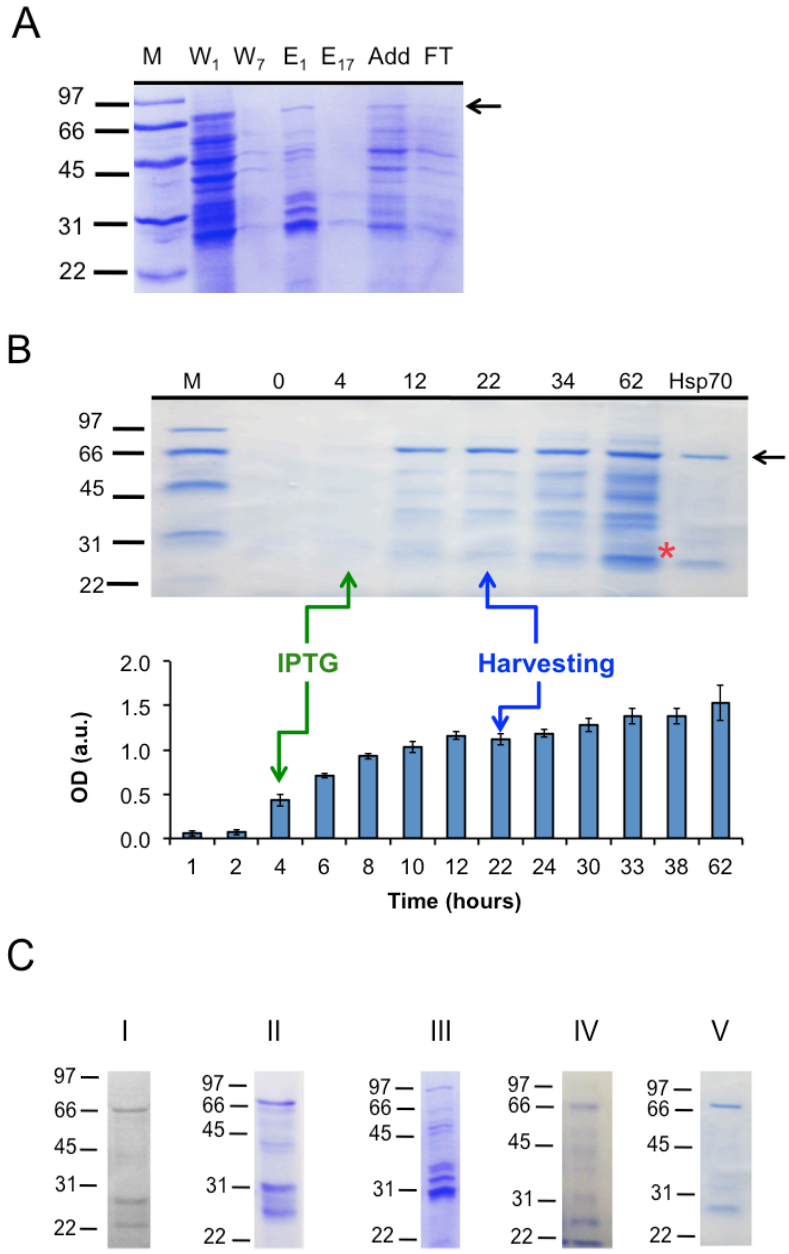

Figure 3.1 Overexpression and purification of *Pf*Hsp70. (A) SDS-PAGE gel of the protein preparations from the various stages of protein purification. Lane M: molecular weight marker; W_1-W_7: first and last washes respectively; E_1-E_{17}: first and last elution respectively; Add: bacterial extract added to the column; FT: flow through. The arrow indicates the position of full length *Pf*Hsp70. The added bacterial extract and the flow through were diluted 1:40 times to prevent sample overloading which lead to blurring of a large area of the gel if the undiluted samples were used. (B) Upper panel: SDS-PAGE gel of protein extracts from the bacterial growth culture after treatment with lysis buffer. Lanes 0 to 62: time (hours) of bacterial culture growth starting from broth inoculation; Hsp70: concentrated purified product; red asterisk marks the time at which a clear increase in the degradation products was seen; arrow, indicates de position of full length PfHsp70. Proteins extracts were obtained from an equal volume of cells, pelleted and resuspended in lysis buffer. Lower panel: optical density of the bacterial growth culture (mean values from 3 aliquots on different growth recipients with error bars representing standard deviations) at different times starting broth from inoculation. In both cases IPTG indicates time of induction and harvesting indicates time of cell harvesting. (C) Purified concentrated protein products from independent protein overproduction experiments. Lane I to V indicates the different batches of protein production, and is presented in chronological order starting from the first protein production experiment.

20.2. Purification of the anti-*Pf*Hsp70 monoclonal antibody

To evaluate the antibody purification efficiency, a 12% SDS-PAGE was used (Figure 3.2). Antibody purification is quite efficient as analyzed by SDS-PAGE. The impure fraction (Lane "Add" on Figure 3.2) is dominated by two major bands corresponding to the heavy and light chains of immunoglobulins, as indicated by the arrows. Another band with great intensity is present in the beginning of the gel, close to the well, possibly corresponding to antibody molecules whose individual polypeptide chains have not been separated by disulfide bridge reduction promoted by the reducing agent present in the sample buffer (β-mercaptoethanol). This band might also be comprised of other high molecular weight impurities not resolved in 12 % SDS-PAGE gels. The non-reduced antibody molecules present in this band can still be seen in the eluted fractions. Higher heating up times or higher percentages of the reducing agent should be able to reduce the amount of this unreduced fraction. As for the flow through, the fraction collected after incubating the antibody impure extract with the protein-G/sepharose resin, contains several bands not corresponding to antibody molecules, and the heavy and light chain bands are not predominant, indicating that practically all the antibody has been retained in the affinity chromatography resin. The washing steps further remove some impurities, as well as some antibody molecules, and the eluted fractions are majorly composed of the light and heavy chains of the immunoglobulin.

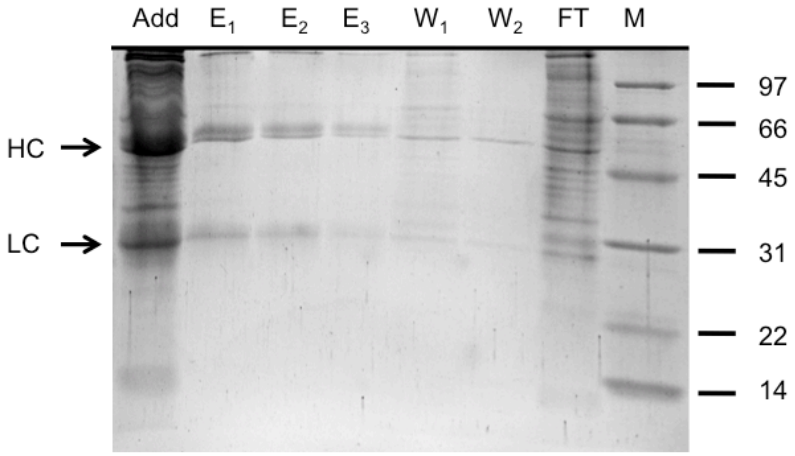

Figure 3.2 Anti-*Pf*Hsp70 monoclonal antibody purification. Lane "Add": impure antibody added to the columns, E and W: elutions and washes by sequential order; FT; flow through; M: molecular weight markers. LC and HC stand for Light Chain and Heavy Chain of the immunoglobulins molecules that run separately on SDS-PAGE gels due to the intermolecular disulfide bridges reduction by β-mercaptoethanol present in the loading buffer.

20.3. Antibody to homemade-gold nanoparticle conjugation

20.3.1. Gold nanoparticle characterization

In Figure 3.3 it is represented the UV-Vis spectrum of AuNP from 5 different nanoparticle batches. Batch I, IV and V, seem to be more monodisperse then batches II and III, as their LSPR bands are slightly narrower (black lines). The ratio between the absorbance at 600 and 520 nm is indicated as an inset table in Figure 3.3, here we can see that for the broader spectra (II and III) it is higher, and it is lower and consistently similar between the three other spectra, 0.207±0.001, with a RSD of 0.47 %. Knowing that broader LSPR bands arise from less monodisperse samples[88], this aggregation ratio apparently seems to be a suitable indicator of the differences in the monodispersion state of different batches of AuNP synthesis. However, this should only be taken as an indication as it has not been correlated with the actual sample degree of monodispersion in a systematic study using an appropriate high resolution size characterization technique such as transmission electron microscopy, usually performed in studies were the UV-Vis spectroscopic features of the nanoparticles are to be correlated with their size distributions[127,134]. Consequently, even thought this differences were noted in the aggregation ratio between different batches, no batches were discarded based on the criteria of having higher aggregation ratios. Regarding the protein to AuNP conjugation, it cannot be stated if the differences in the band broadness seen between different nanoparticle batches actually influence the activity of the conjugates formed, as no study was performed to test this, although it may be regarded as a possible source of variability in the antibody to nanoparticle conjugates' activity.

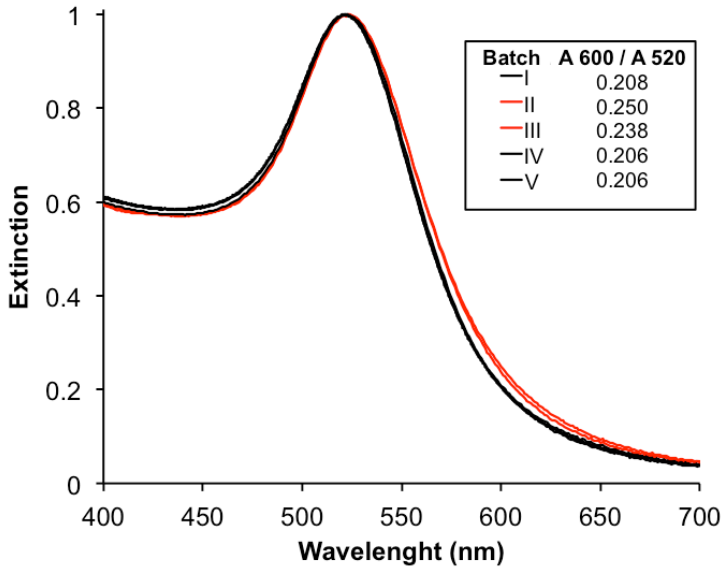

Figure 3.3 UV-Vis spectrum of five AuNP batches. Normalized UV-Vis spectrum at the absorbance of the LSPR maximum; inset: aggregation ratios. [AuNP] ≈ 1 nM.

Gold nanoparticles are sensitive to the pH and ionic strength of the dispersant. Surface charge neutralization, results in colloid aggregation at a certain value of ionic strength[17,35]. As a result a second band, red-shifted from the LSPR band of "stable" colloids is seen in a UV-Vis spectrum (see Figure 3.4 A). AuNP (citrate stabilized) and AuNP surface modified with MUA, hereafter referred to as AuNP@MUA, both aggregated at NaCl concentration of 30 mM, and their pH stability is very similar. These results were obtained with MUA to AuNP molar ratio of 120 to 1, and this ratio was used throughout the present work. MUA molecules at the AuNP surface bind covalently trough the thiol group, the saturated backbone allows the molecules to be closely packed due to hydrophobic interactions, and finally the carboxylic groups confer solubility and allows covalent coupling to the lysine side chains of proteins using EDC/NHS cross-linkers. This monolayer protected gold surface would also be more promising for retaining the native antibody structure by avoiding direct binding to the AuNP surface. [35].

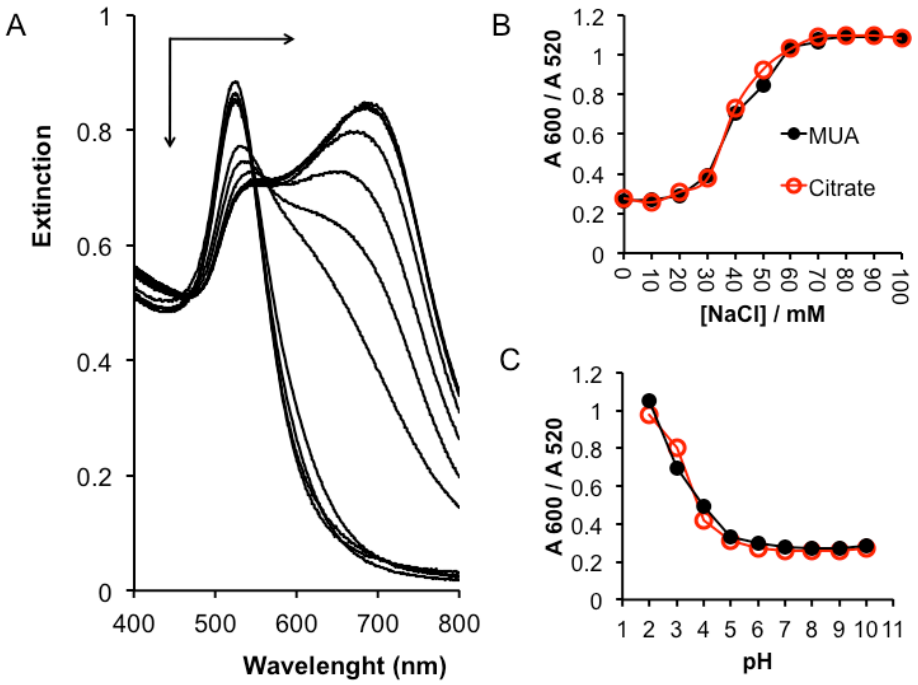

Figure 3.4 UV-Vis assessment of the AuNPs and AuNPs@MUA's stability against pH and ionic strength challenge. (A) UV-Vis extinction spectra of AuNPs (1.7 nM, pH 7) challenged against increasing NaCl concentration in the 0 to 100 mM range. (B) Aggregation ratio highlighting a minimal 30 mM NaCl necessary for initiating aggregation in both particles. (C) Aggregation ratios for pH titration experiments on AuNPs and AuNP@MUA (1 nM), highlighting the similar pH dependence response.

A small redshift in the LSPR can sometimes be seen for the MUA to AuNP molar ratios of 360. This shift is negligible as it is of only 1-2 nm (within equipment error), however, when this ratio

is increased, the shift is as large as 7 nm for some of the larger MUA to AuNP molar ratios tested (from 1500 to 1 500 000) indicating a noticeable variation in the refractive index of the surface of the AuNPs. To prove that this shift is caused by increasing amounts of MUA covalently bound to the nanoparticle surface, one would have to design an experiment whose response would be dependent on the degree of surface coverage of AuNP by MUA. As the aggregation of AuNP with changing pH is dependent on the pKa values of the adsorbed surface stabilizers, as citrate or MUA, the titration of AuNPs at different MUA to AuNP molar ratios, would provide a way of determining an apparent pKa value of the nanoparticle (or "half titration point" as in Ref.[35]) as it changes from a monodisperse colloidal state towards an aggregated state. The different pKa values obtained, after fitting the titration curve to a sigmoidal curve (using a Boltzman equation) are presented in Figure 3.5, along with the changes in the wavelength of the LSPR maximum for several different MUA to AuNP molar ratios. These results show that the LSPR maximum stabilized around 526 nm, a ~6 nm shift from citrate stabilized AuNP, and the apparent pKa value stabilized around 4.5, being the citrate stabilized AuNP apparent pKa of ~2. This shows that the MUA to AuNP molar ratio of 360 was not enough for completely exchanging the citrate molecules at the AuNP surface, nevertheless it should be noted that this small ratio was enough for the covalent binding of antibodies, as will be shown in the next sections.

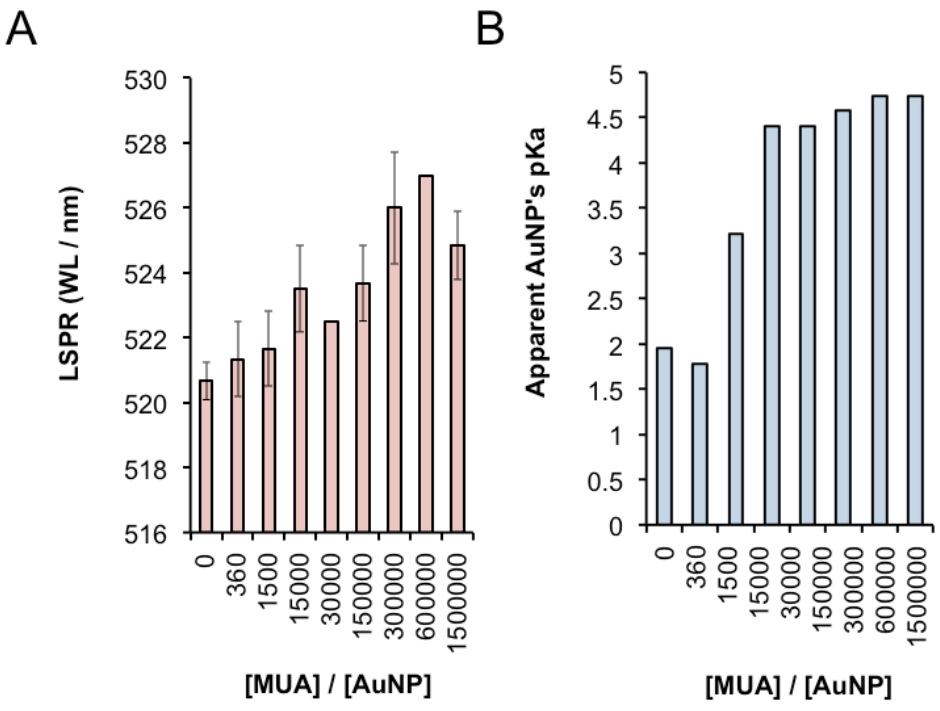

Figure 3.5 Shift of the AuNP@MUA's LSPR and apparent pKa values with increasing MUA to AuNP ratios. (A) The shift in the AuNP@MUA SPR is represented as an average of the LSPR (wavelength of the LSPR maximum) at 3 pH values in the 7 to 11 units range, error bars represent standard deviations. (B) For the titration experiments, the aggregation ratio parameter was calculated for each pH value at each MUA to AuNP molar ratio, these data were fitted to a sigmoidal tendency curve (using a Boltzman function, Origin 7.5 Software) and the maximum of the first derivative of the sigmoidal fit is the value assigned to be the apparent pKa value of the MUA functionalized AuNP. [AuNP]=0.67nM.

20.3.2 Proving antibody conjugation and colloidal stability: UV-Vis

20.3.2.1. Localized Surface Plasmon Resonance shift

For the electrostatic conjugates, a redshift of 7±1 nm of the LSPR is seen for all the Ab to AuNP molar ratios tested, in relation to the LSPR of AuNP in the absence of Ab whose LSPR is ~520 nm. The exception was the Ab to AuNP molar ratio of 15, where the shift was 20±8 nm (Figure 3.6D), accompanied by significant band broadness (Figure 3.6B). This broadening was attributable to the presence of the Ab and not to the presence of the incubation buffer (Figure A.1A Appendix).

For the cross-linked conjugates, the redshift in the LSPR was 7±1 nm upon antibody conjugation, except for the Ab to AuNP molar ratios of 30 and 15 with 26±8 and 74±38 nm redshifts (Figure 3.6C) taken as an indication of aggregation. As can be seen in the lower panel of Figure 3.6A, the cross-linked AuNP@Ab are visually stable starting at ratio 60. When no Ab was added, the presence of the cross-linkers induced a shift in the extinction spectrum maximum of 223±48 nm (Figure 3.6C), this is due to the plasmon coupling of the particles that are now in close proximity, resulting in a second extinction band red shifted from the LSPR of unperturbed AuNP colloids (Figure 3.6A). The appearance of a second band red shifted from the LSPR is also seen in the Ab to AuNP molar ratio of 15. The appearance of the second band in the ratio of 30 is not obvious from the extinction spectrum, it seems that there has only been a redshift in the energy of the LSPR, not the appearance of a new band red shifted from the LSPR.

It is interesting to see that in Ab to AuNP molar ratios of 0 to30, the lower the Ab to AuNP ratio, the larger the redshift in the extinction spectrum. As explained in the introduction section, the shift in the frequency of the oscillating dipoles of the AuNP increases with decreasing inter-particle distance, therefore, these results area possible indication that the inter-particle distances increased from Ab to AuNP ratio 0 to 30.

The cross-linkers promoted aggregation seen by an increase in the band broadness and appearance of a second extinction band can be exclusively attributed to EDC and is independent of the presence of MUA (see Figure A.1C Appendix).

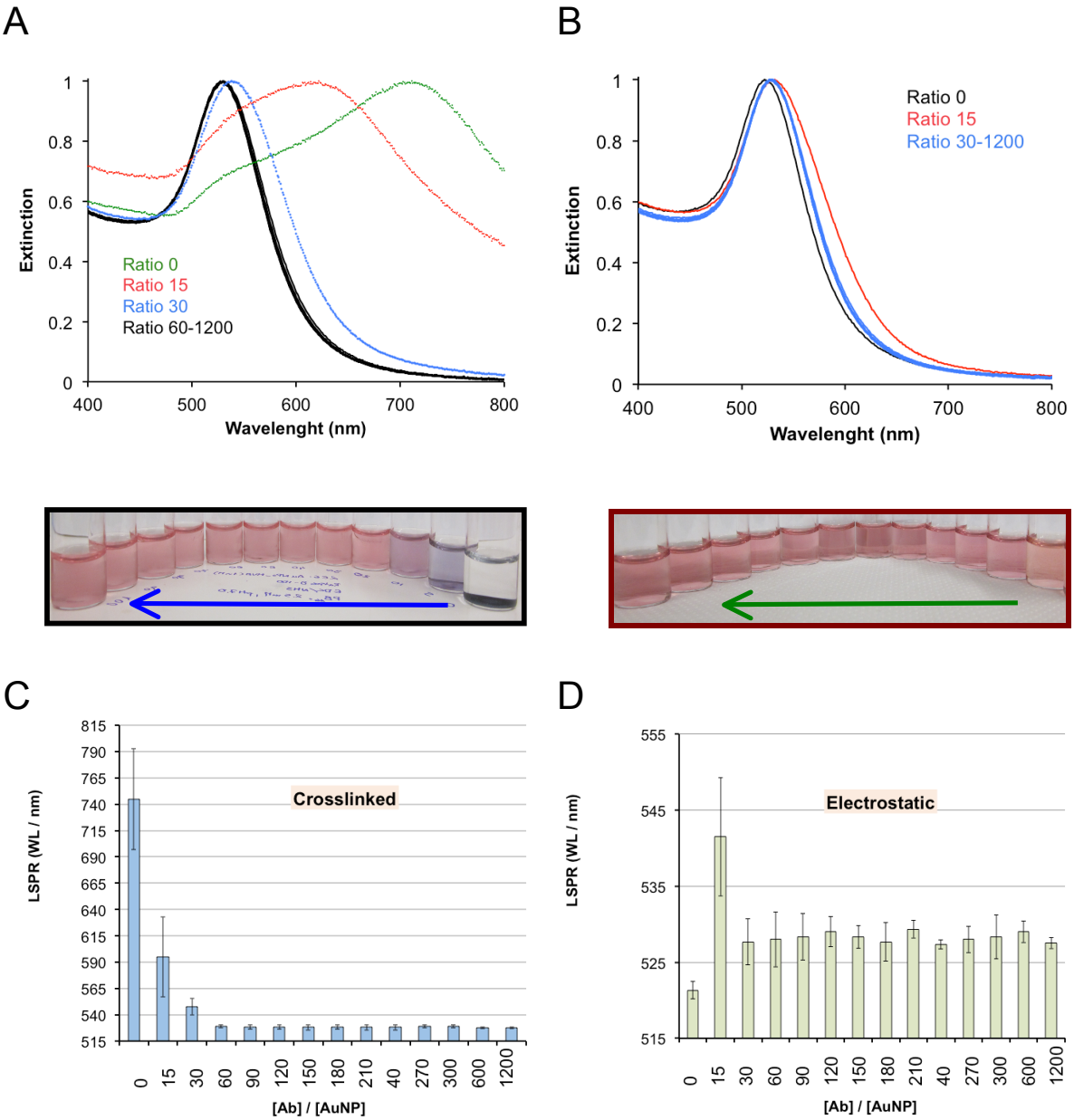

Figure 3.6. LSPR changes in AuNP@MUA to antibody conjugates. UV-Vis spectrum of cross-linked (A) and electrostatic (B) AuNP@Ab conjugates. Spectra were normalized at the absorbance maximum to highlight changes in the band broadness. Lower panels shown digital pictures of the colloids, arrows indicate increasing Ab to AuNP molar ratios: 0, 15, 30, 60, 90, and so on until 300. (C) and (D) LSPR wavelength (nm) as function of the Ab to AuNP molar ratio, with average results of 3 and 2 independent experiments plotted, respectively, and error bars representing SD. [AuNP]=0.67nM.

20.3.2.2. Colloidal stability upon ionic strength challenging

In the presence of 30 mM NaCl AuNP@MUA start to aggregate as evaluated by the aggregation ratio (Figure 3.4B). Antibody conjugation to AuNP@MUA (AuNP@Ab) will be shown to increase the stability against ionic strength challenging. This is *per se* a proof of conjugation. It

indicates a mechanism of colloidal stabilization, where proteins at the AuNP surface avoid particles from coming as closely spaced in solution, as they would be in the absence of proteins. These studies were further extended to evaluate the degree of surface coverage by defining the minimal antibody concentration necessary to stabilize the AuNP@Ab conjugates against a fixed NaCl concentration (0.15 and 1.5 M NaCl). This is commonly called "colloidal aggregation test" in the immunoassay area.

The minimal Ab to AuNP molar ratio necessary for stabilizing the AuNP@MUA against ionic strength challenge is 60 for the cross-linked conjugates (Figure 3.7A) and 30 for the electrostatic conjugates (Figure 3.7B). This difference in the minimal Ab ratio is not an indication that the electrostatic approach is able to saturate the AuNP surface at lower Ab to AuNP ratios, because the cross-linked conjugates are already aggregated at the Ab to AuNP molar ratio of 30 before ionic strength challenging, due to the presence of EDC, one of the cross-linkers.

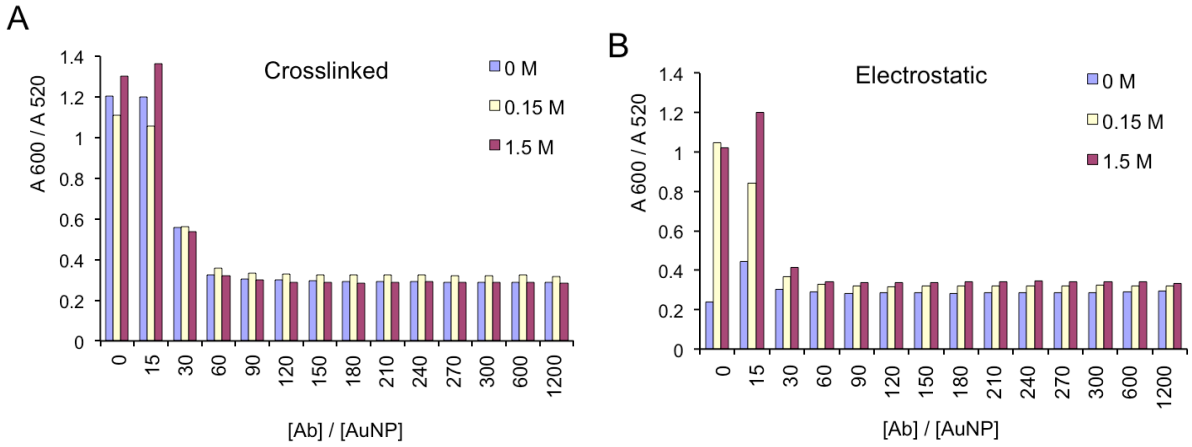

Figure 3.7 Colloidal aggregation tests of AuNP@MUA to Ab conjugates. The aggregation ratio is plotted as function of the molar concentration of NaCl added, 0 M represents the conditions were no salt was added. The data for both the cross-linked (A) and electrostatic (B) approaches is presented. [AuNP]=0.67nM.

20.3.2.3. Colloidal stability upon BSA blocking and washing

The aggregation ratio was used to monitor the stability of the AuNP@Ab throughout the different experimental preparatory steps used to prepare them: conjugation to the antibody, BSA blocking and washing from excess proteins (Figure 3.8). All Ab to AuNP molar ratios of the two conjugation approaches, electrostatic and cross-linked, were stable against BSA blocking and washing as accessed by the aggregation ratio parameter (Figure 3.8 A and B). AuNP@Ab conjugates at an Ab to AuNP molar ratio of 75, BSA blocked and washed (conditions used in the fluorescence assay, see below) were challenged against 1.5 and 0.15 M NaCl, and they remained stable (Figure 3.8 C). The normalized extinction spectra of AuNP@Ab and their BSA blocked and washed conjugates are almost superimposable (Figure 3.8 D, green lines) indicating that no significant changes in the LSPR band broadness were detected. Ionic strength challenging induced a noticeable increase in the band

broadness (Figure 3.8 D red and blue lines), however, they remained visually stable (no red to violet color change even after several months).

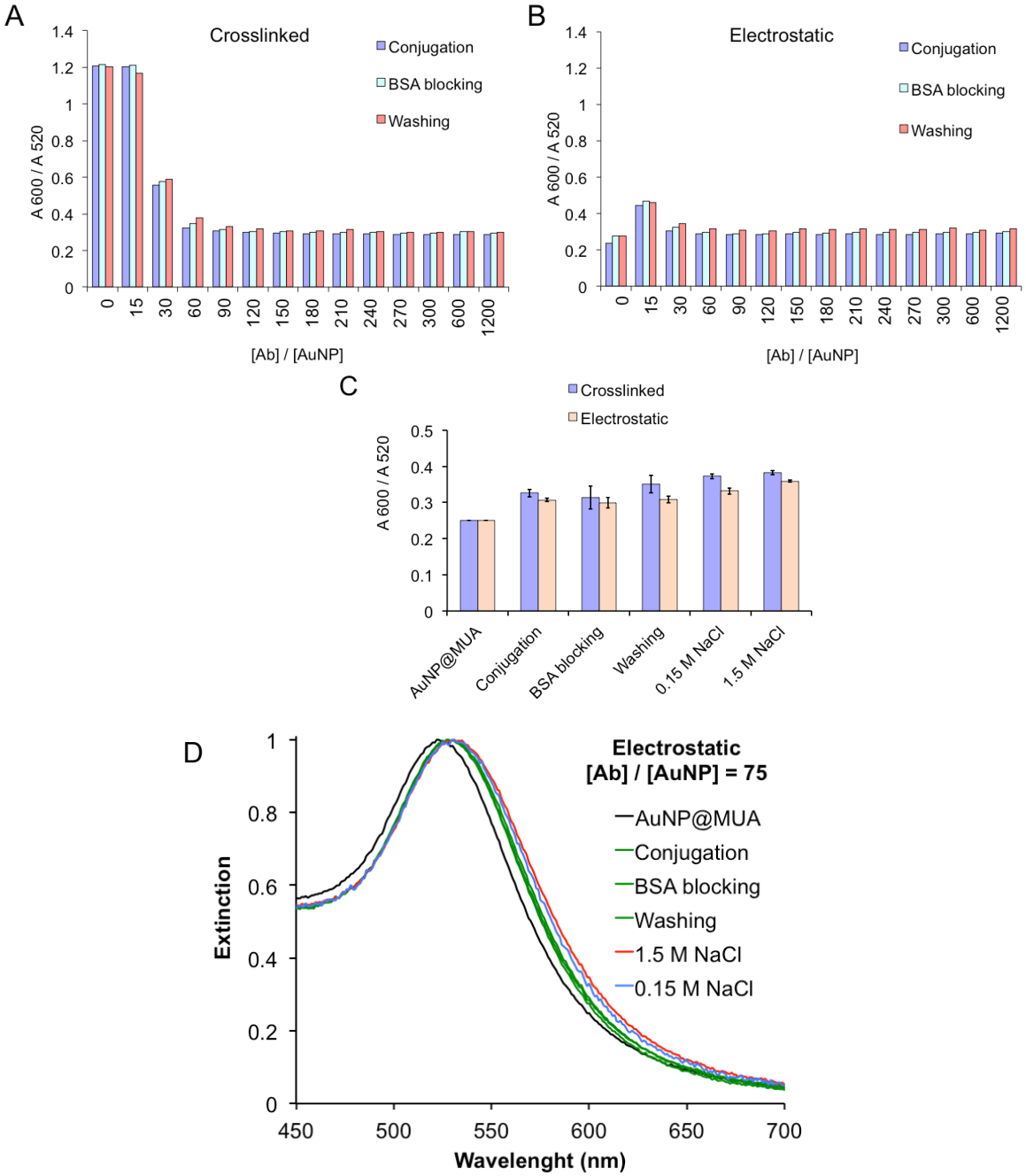

Figure 3.8 Colloidal stability upon BSA blocking and washing of electrostatic and cross-linked conjugates. Aggregation ratios for the AuNP@Ab conjugates at the different preparatory steps (conjugation, blocking and washing) for the different Ab binding approaches, cross-linked (A) *vs* electrostatic (B) at Ab to AuNP molar ratios of 0 to 1200. (C) Aggregation ratios for the AuNP@Ab conjugates at the different experimental steps (conjugation, blocking, washing) and for the ionic strength challenging (0.15 and 1.5 M NaCl) for the Ab to AuNP molar ratio of 75 of both the Ab binding approaches. The aggregation ratios for unconjugated AuNP@MUA are also presented. (D) UV-Vis spectra for the different preparatory steps of the electrostatic conjugation approach are presented, highlighting the small differences in the spectra broadness of AuNP@MUA (black line), the spectra of the different preparatory steps (green line) and the spectra of the washed BSA blocked conjugates upon increased ionic strength challenging (blue and red lines). UV-Vis spectra were normalized at the absorbance maximum to highlight the differences in the band broadness. The spectra are representative of two independent experiments. [AuNP]=0.67nM.

20.3.2.4. Colloidal stability upon pH challenging

The simple inspection of the pH versus aggregation ratios curves allows us to infer that there is an effective conjugation of the Ab to the AuNP as the experimental curves are quite different. For AuNP@MUA, after aggregation starts at pH close to 4-5, the particles remain aggregated when the pH is further decreased, if the antibodies are present at the surface, this aggregation starts at higher pH values, close to 5-6, but then at pH values lower then 3-3.5, the colloid seem to remain stable again (Figure 3.9). The exact nature of this phenomenon was not studied. Possibly the isoelectric point of the Ab is achieved at pH close to 5-6, minimizing the electrostatic repulsion, and maximizing the attractive interactions between the AuNP@Ab conjugates. The increased stability below pH 3-3.5 might be caused by changes in the protein conformation and overall charge in these acidic conditions. The most important information is that the conjugates should be used at pH higher than 6.

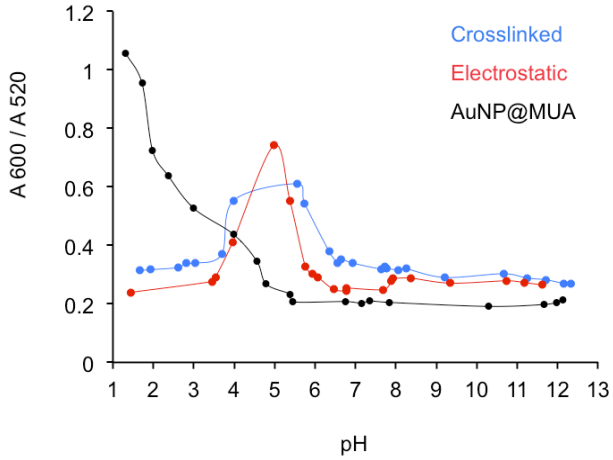

Figure 3.9 Stability of the AuNP@MUA and AuNP@Ab at different pH values. Aggregation ratio at different pH values for AuNP@MUA (black line) and for cross-linked (blue line) and electrostatic (red line) AuNP@MUA to Ab conjugates. BSA blocked and washed conjugates where tested. [MUA]/[AuNP]=360, [AuNP]=0.67nM, [Ab]/[AuNP]=75.

20.3.3. Proving antibody conjugation and colloidal stability: DLS

Upon Ab binding, DLS could detect a size increase (ca. 19 nm) much larger then the uncertainty of the method (ca. 2.2 nm, *SD* of 3 independent measurements), and there is no colloid destabilization as accessed by the PdI (Figure 3.10).

Some scattering intensity size distributions obtained on different days on the same AuNP@MUA stock solution showed larger peaks corresponding to a small fraction of the total scattered light, but enough to increase the PdI values to values larger then 0.3, which is often referred as the threshold for a stable colloid[27], and therefore this larger peaks could be attributed to some sample aggregation.

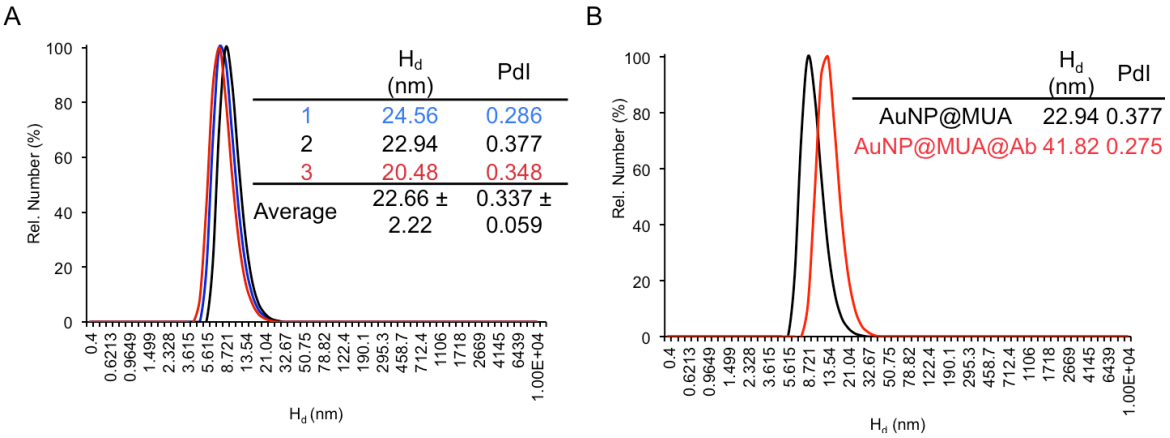

Figure 3.10 DLS relative number size distributions of AuNP@MUA and AuNP@Ab. (A) The results of three independent measurements (different days) on the same AuNP@MUA batch color codded. (B) AuNP@MUA size increase upon Ab conjugation. [Ab]/[AuNP]=300. Each distribution averages 3 measurements with 20 sub runs. [AuNP]=0.67nM.

20.3.4. Proving antibody conjugation and colloidal stability: DCS

Upon Ab binding to AuNP@MUA, DCS could detect a size increase in the diameter (ca. 7.72 nm) much larger then the uncertainty of the method (ca. 0.14 nm, *SD* of 3 independent measurements). The actual experimental observation is a decrease in the size of the particles upon Ab conjugation (Figure 3.11). In fact, upon conjugation there is a decrease in the particles density, meaning that the particles take more time to sediment, as compared to unconjugated particles without a protein "shell" (or "corona") at its surface. Mathematical treatment of the experimental data can be applied to get an estimative of the particle's shell thickness (see Materials and Methods in the Appendix).

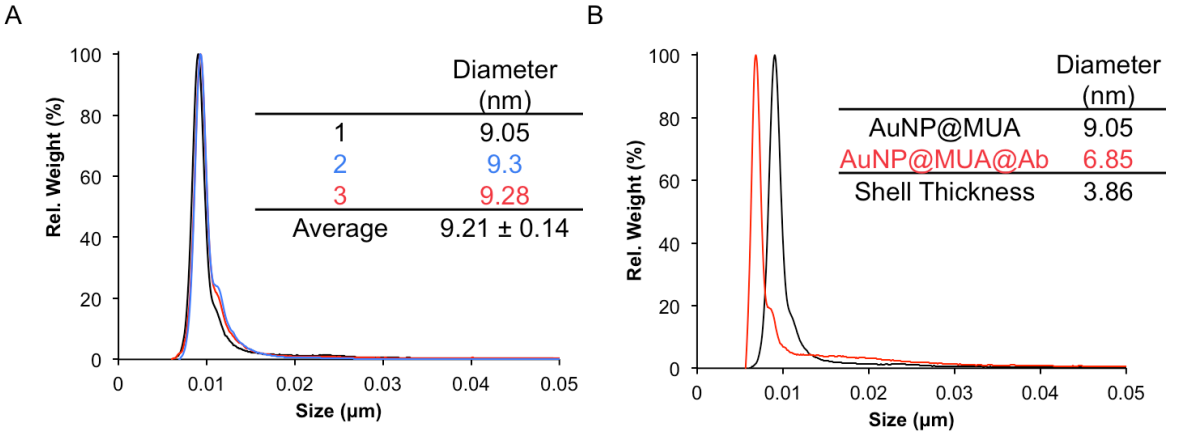

Figure 3.11 DCS relative weight size distributions of AuNP@MUA and AuNP@Ab. (A) The results of three independent measurements (different days) on the same AuNP@MUA batch color codded. (B) AuNP@MUA size increase upon Ab conjugation. [Ab]/[AuNP]=300, [AuNP]=0.67nM.

The DLS retrieved size is the average hydrodynamic diameter (often given the symbol Z or z-average), and it is an intensity mean. This leads to different size distributions if the results are analyzed by intensity distribution or by number distribution (Figure A.2 Appendix). For the homemade-AuNP@MUA stock used the DLS retrieved size is ~23 nm, but the number distribution is centered around 9-10 nm (inset Figure A.2 Appendix) These differences arise from the fact that larger particles scatter more light then smaller particles and their contribution biases the experimentally observed intensity distributions towards larger sizes, even thought by number their percentage is bellow 0.01%. This might be the reason why the DLS retrieved size is much larger then the average diameter obtained by TEM, ~14 nm (Figure A.3 Appendix). The differences might also arise from inter-batch variability, or in the measuring methods themselves. TEM allows us to measure the diameter of the inorganic gold core in dried samples, DLS retrieved size is the that of a sphere of equal hydrodynamic diameter as the average scattering particle in suspension. For DCS, the AuNP analyzed were from the same stock used for DLS, and the reported diameter was ~9 nm, more in agreement with the DLS number size distribution, centered around ~10 nm (Figure A.2, inset, in the Appendix). The differences must arise from the analytical methods themselves. The DCS retrieved size is that of a sphere with a certain hydrodynamic diameter that would take the same amount of time to sediment in the density gradient, as the time the experimental particle takes to sediment.

As for the size of the Ab shell thickness, DCS showed an increase of the diameter of ca. 7.7 nm, and DLS, and increase of ca. 19 nm ([Ab]/[AuNP]=300).

20.3.5 Proving antibody conjugation and colloidal stability: AGE

The cross-linked conjugates from ratio 0 to 30 display blue to violet colors (Figure 3.6 A), ratios 60 to 120 are visibly stable. Pelleting by centrifugation to remove excess antibody and to concentrate the AuNP before loading doesn't further destabilizes the AuNPs (see condition "washing" in Figure 3.8 A). However when the gel is run the bands from ratios 60 to 120 are only marginally stable (Figure 3.12 A), an indication that the electric field, interaction with the matrix[107] or surface charge cancellation and/or aggregation due to the buffers ionic strength are an additional barrier to the stability of the conjugates, particularly if these have low [Ab]/[AuNP] ratios. In the same way, when electrostatic conjugates are run (Figure 3.12 B), long smears are observed for the smaller [Ab]/[AuNP] ratios, rather then a compact band as observed for the larger ratios.

Cross-linked conjugates mobility is constant (ca. -0.6 $\mu m.cm.V^{-1}.s^{-1}$), while the electrostatic conjugates mobility decreases with increasing [Ab]/[AuNP] ratio, until saturation is achieved (at ca. -0.4 $\mu mcmV^{-1}s^{-1}$). Saturation occurs at [Ab]/[AuNP] ratios of ca. 300 and ca. 75 for the electrostatic and crosslinking approaches respectively. Taken together these results indicate that less Ab molecules are needed for a compact corona (saturation of the surface) with the cross-linkers.

ζ-potential measurements (Figure A.4 and accompanying discussion in Appendix) performed by Bassem Giurgis and Dr. Inês Gomes, FCT/UNL, Portugal, have corroborated this finding, Ab to AuNP binding saturation (indicated by a ζ-potential plateau) was achieved for smaller ratios when cross-linkers where used.

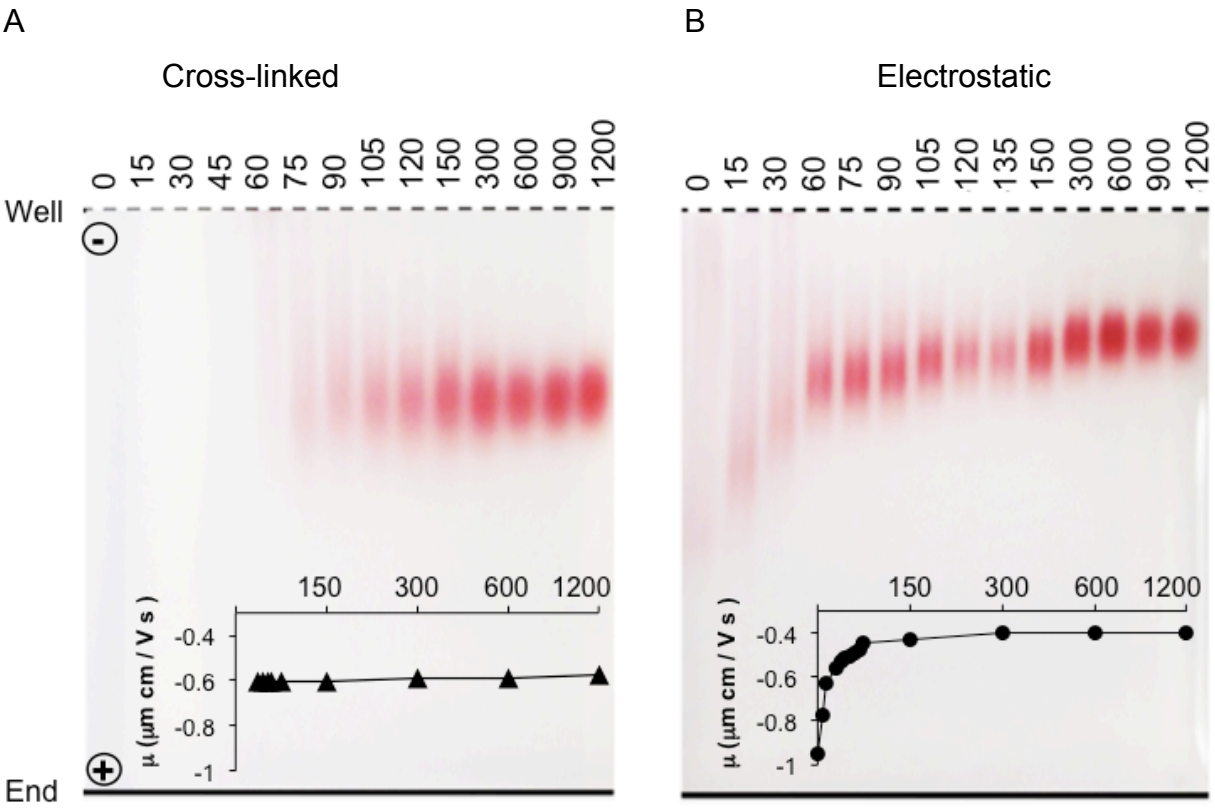

Figure 3.12 AGE of AuNP@MUA to antibody conjugates. AGE of AuNP@MUA functionalized with Ab by the electrostatic (A) or cross-linking (B) approaches. The [Ab]/[AuNP] ratios are indicated in each well, + and – indicate the relative position of the electrodes. Insets: electrophoretic mobility of the conjugates calculated from the agarose gels (see material and methods for calculation).

20.4. Proving the activity of AuNP@Ab conjugates

To prove that: 1) the recombinant Ag (*Pf*Hsp70) is recognized by the monoclonal Ab (2E6); 2) the Ab can detect the native antigen; 3) the Ab retains its activity when conjugated to the gold nanoparticles, Western blot analysis was performed on the recombinant antigen and on infected and non-infected blood samples. "Infected" means a sample from a RBC culture infected with *Plasmodium falciparum*, and non infected blood was obtained from a healthy donor. For the immunostaining the classical approach was used, in which after blotting the SDS-PAGE samples to a nitrocellulose strip, the antigen is detected by incubation with the primary Ab (2E6), followed by incubation with a horse radish peroxidase labeled secondary Ab for chemiluminescence detection. A

less common approach for immunostaining was to reveal the target Ag on the nitrocellulose strip using the AuNP@Ab conjugates (Figure 3.13).

As can be seen from Figure 3.13, the Ab could detect both recombinant and native forms of the Ag, and the activity of AuNP@Ab conjugates is retained. These experiments are a prof of conjugation, a prof of the AuNP@Ab conjugates and a prof that the antibody-antigen pair can be used for detection in clinical samples, as well as for studies with the recombinant for of the protein.

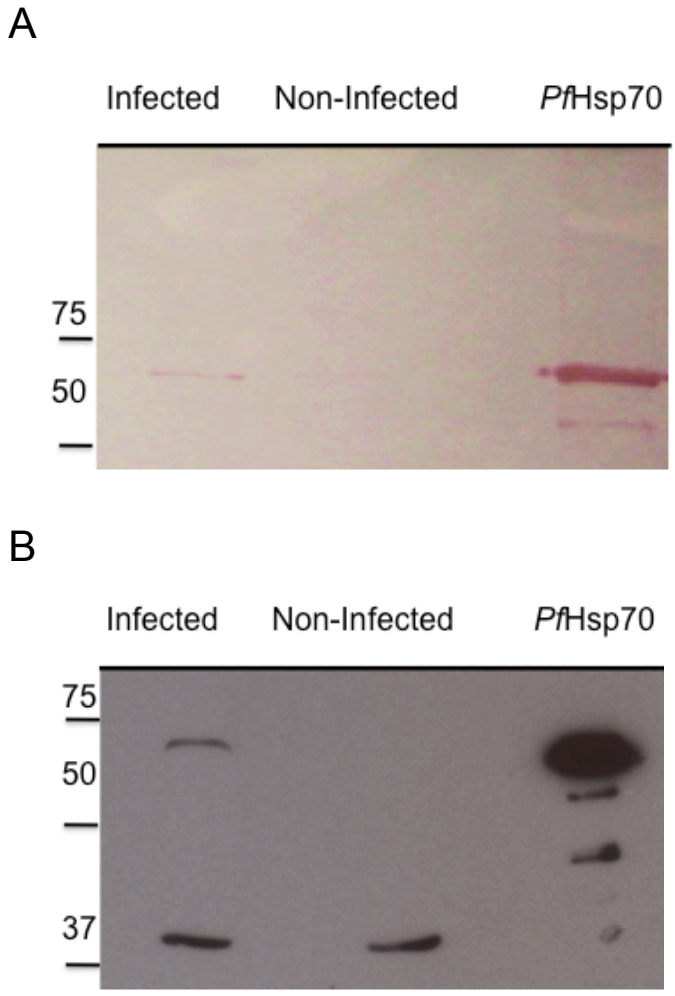

Figure 3.13 Detection of the recombinant and native forms of the Ag (*Pf*Hsp70) by traditional and modified Western blot. Detection of the native form of the Ag was performed using saponin treated pellets of infected human RBC culture (Lane: Infected), and blood from an healthy donor was used as a non-infected control (Lane: Non-Infected). Detection of recombinant Ag was performed using the Ag purified in the present work (Lane: *Pf*Hsp70). (A) Modified Western blot: Ag detection (red bands) was performed by incubating the membranes with AuNP@Ab, [Ab]/[AuNP]=75, [AuNP]=0.83nM. (B) Classical Western blot: Ag detection was performed by immunostaining with the Ab and an horse radish peroxidase-conjugated secondary antibody. A band corresponding to *Pf*Hsp70 was detected in the infected but not in the non-infected samples. The bands at ~42 KDa, right panel, correspond to specifically immunostained actin, used as loading control.

20.5. Cy3B labeling of the Ag

The Ag was effectively labeled by the fluorophore Cy3B, as perceived by the red shift in the absorbance maximum of the UV-Vis spectrum of Cy3B when conjugated to the protein (Figure 3.14), and by the fact that after several washing steps, using centrifugal ultrafiltration devices, the eluate was clear, without exhibiting the characteristic pink color of Cy3B, or any significant absorption in the Cy3B typical visible absorption range[132], while the retentate remained visibly pink.

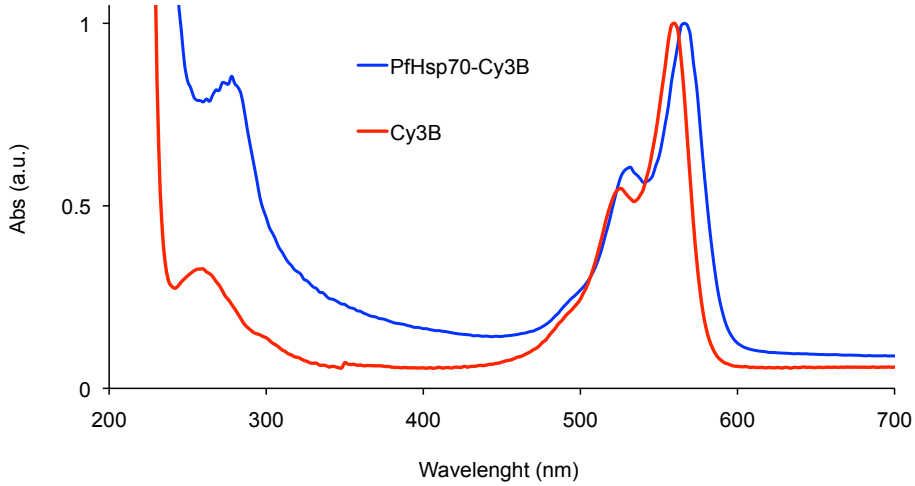

Figure 3.14 Absorbance spectra of free Cy3B (red trace) and of Cy3B-labeled Ag (blue trace). Shift in the peak maximum occurred from 558 nm to 566 nm upon labeling. The spectra were normalized at the absorption maximum in the visible range. Both solutions where prepared in PBS.

20.6. Immunoassay

A linear response between the Ag concentration and the relative fluorescence increase was obtained in the 8.2 to 24 μg mL^{-1} range (Figure 3.15). Regarding the sensitivity of the assay, a tentative statistical limit of detection (SLoD) was determined to be 2.4 μg.mL^{-1} (SLoD = 3.3 x *SD* / *m*, where *SD* is the standard deviation of the y intercept of the calibration curve, and *m* the slope of the calibration curve); and the statistical limit of quantitation (SLoQ) was estimated to be 7.3 μg mL^{-1} (LoQ = 10 x *SD* / *m*) according to[135].

As for the repeatability of the assay, the intra-assay coefficient of variation (Intra-assay CV (%) = (mean of the *SD* of 10 duplicated samples / grand mean of the duplicates) x 100) was calculated to be 4.7 %, while the inter-assay coefficient of variation (Inter-assay CV (%) = SD of the mean of 10 duplicates measured in different days / grand mean of the duplicates) x 100) was calculated to be 6.3

%. A figure of less then 10 % for the first and 10-15 % for the second is considered to be satisfactory, therefore the repeatability of the proposed assay is considered to be well within the acceptable ranges for an immunoassay[136].

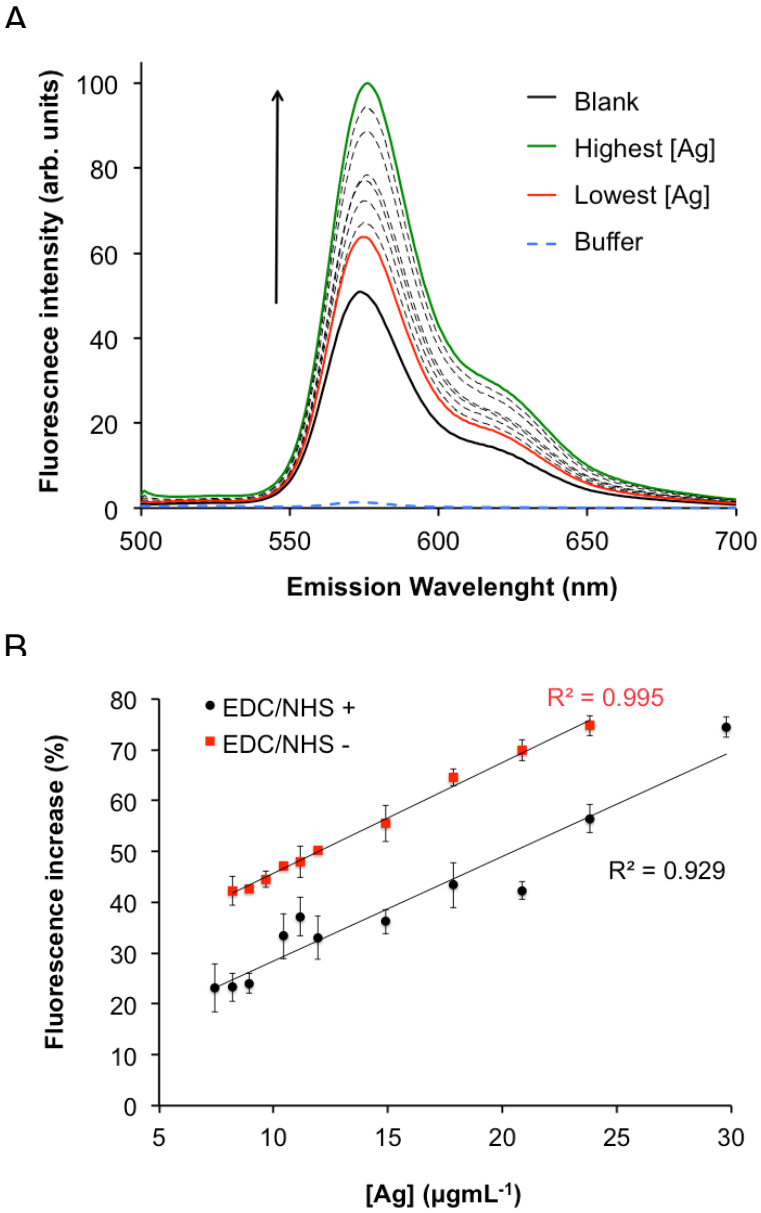

Figure 3.15 Fluorescence response and influence of the conjugation conditions on the homemade-AuNP immunoassay. (A) Typical fluorescence emission spectra of the immunoassay. (B) Relative fluorescence increase (%) as a function of the Ag concentration for the electrostatic (red dots) and for the crosslinking procedure (black dots). Continuous lines are linear regression fits to the experimental data. Error bars represent *SD* from 3 replicate measurements averaged.

20.6.1. Influence of the conjugation strategy in the activity of AuNP@Ab conjugates

The fluorescence increase for the cross-linked conjugates ([Ab]/[AuNP]=75) is consistently lower then that for electrostatic conjugates in the concentration range tested. Electrostatic conjugates are therefore more active, i.e. they are able to bind more Ag than their cross-linked counterparts at, almost, any given concentration tested. Linear detection ranges of 8.2 to 24 and 7.4 to 30 μgmL^{-1}, SLoD of 2.4 and 5.7, and SLoQ of 7.3 and 17 were obtained for electrostatic and covalent conjugates, respectively.

20.6.2. Detection of the native Ag in *P. falciparum* infected RBC culture

Saponin extracts of the membranes of *P. falciparum* infected RBCs from a RBC culture and RBC from an healthy, non-infected, human donor, were analyzed in the current assay. Starting from the initially obtained extracts (see Materials and Methods) a 1:10 dilution followed by 4 consecutive (1:1) dilutions with PBS were prepared. These were then tested in the assay, in the same experimental conditions as those used for the purified *Pf*Hsp70.

An analytical signal was obtained that decreased linearly with the increasing dilution of the extracts (Figure 3.16). The background signal that could be detected in the sample obtained from saponin-treated isolated RBCs from non-infected blood was ca. 30 in the fluorescence increase scale, a value equivalent to that obtained for a 160-fold diluted infected sample. The next dilution, 80-fold, had a fluorescence increase value significantly above the background signal from the non-infected samples.

Assuming a single parasite infection in each RBC, in the 3% parasitemia infected RBC culture, a parasite density of *ca.* 1.7×10^5 parasites.μL^{-1} was obtained. This means that the 80-fold dilution corresponds to a parasite density of ca. 2000 parasites.μL^{-1}. Therefore the immunoassay is suitable for clinical malaria diagnostics as the recommended values by WHO for a reliable identification of clinical malaria is between 2000 to 5000 parasites.μL^{-1}, a parasite density range bellow the density found in many populations with endemic malaria[12].

Introducing the fluorescence increase value of the 80-fold dilution in the calibration curve of Figure 3.15, a value of *ca.* 14.9 $\mu g.mL^{-1}$ of *Pf*Hsp70 is obtained in the saponin extract of the RBC infected culture.

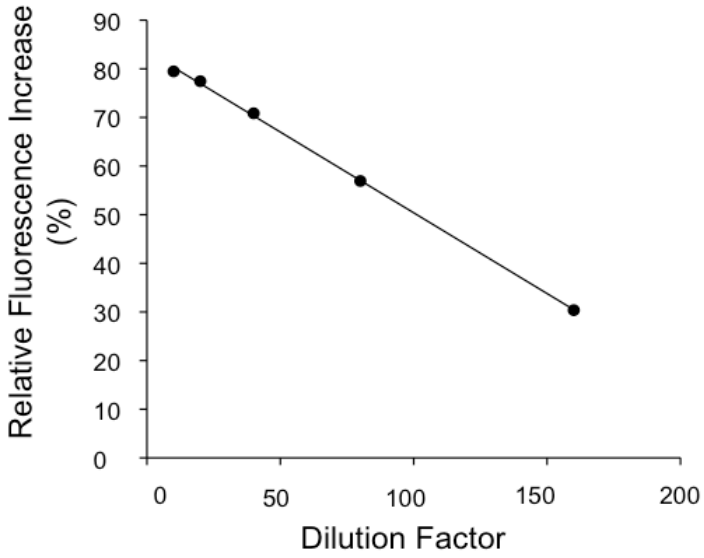

Figure 3.16 Detection of native Ag (*Pf*Hsp70) in saponin extracts of a *P. falciparum* infected red blood cell culture. Sequential dilutions of a RBC saponin extract from a human RBC culture presenting a 3% parasitemia level were assayed. Each point averages 3 consecutive measurements.

21 Molecular-level antigen to AuNP@Ab binding

In this section all the experiments were conducted using commercial-gold nanoparticles with a diameter of approximately 30 nm. The acronym AuNP, that standed for homemade-gold nanoparticles in section 20, now stands for the commercial-gold nanoparticles. Whenever homemade-gold nanoparticles are to be cited, they will be referred to as homemade-gold nanoparticles, or homemade-AuNP.

21.1. Antibody to commercial-gold nanoparticle conjugation

21.1.1. Colloidal stability of the AuNP@Ab conjugates

As for the homemade AuNP, the antibody conjugation and colloidal stability was studied for commercial AuNPs.

In contrast to the homemade-AuNP@MUA stock colloid, only one peak (one distribution) corresponding to 100 % of the light scattered intensity was detected by DLS for the commercial-AuNP, with a PdI consistently bellow 0.3. The size increase upon Ab binding (ca. 9.7 nm) was larger then the error of the method (ca. 1.01 nm, *SD* of three independent measurements) and there was no colloidal destabilization as assessed by the PdI (Figure 3.17 A and B). DCS detected size increase and error of the method were ca. 13.8 and 0.27 nm respectively (Figure 3.17 C and D).

DLS and DCS reported sizes are 33.4 and 26.0 respectively (on the same AuNP stock solution). For the homemade-AuNP@MUA, DLS also reported larger sizes, supporting the notion that DLS reported intensity averaged size is biased towards larger sizes due to the more intense scattering by larger particles. DLS is also more sensitive to the presence of small aggregates, as these are taken into account in the reported size, while for DCS, only the main peak is considered.

As for the Ab shell, DCS showed an increase of the diameter of ca. 13.8 nm while DLS showed and increase of ca. 9.7 nm ([Ab]/[AuNP]=200). There is a better agreement in the shell thickness for the commercial-AuNPs than for the homemade-AuNP@MUA. Commercial-AuNP had smaller PdI (consistently bellow 0.3) then homemade-AuNP@MUA, possibly contributing to the better agreement between DCS and DLS, as less aggregates would bias the DLS calculated average size from the intensity distribution, towards larger sizes.

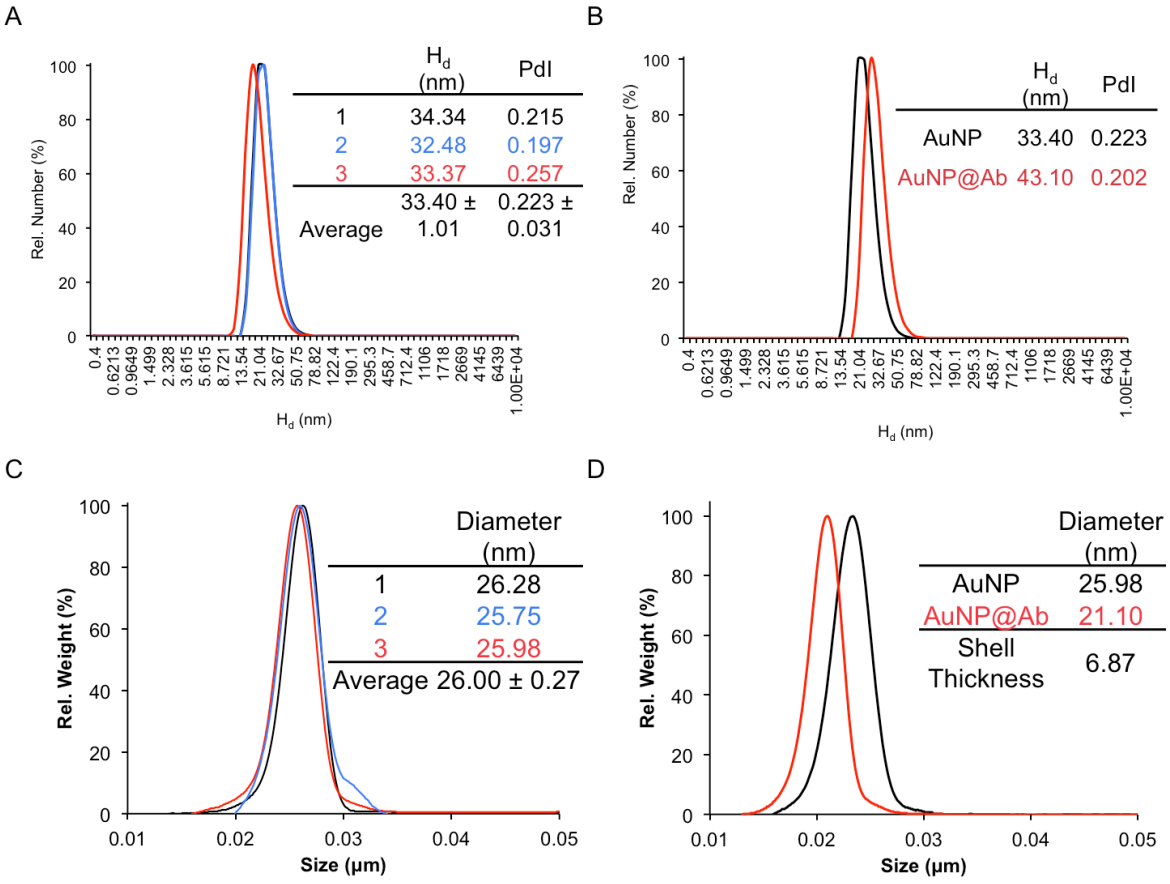

Figure 3.17 Size distributions of commercial AuNP and AuNP@Ab. The results of three independent measurements (different days) on the same AuNP batch are color-coded for DLS (A) and DCS (C). AuNP size increase upon Ab conjugation in DCS (D) and DLS (B) where each distribution averages three measurements with twenty sub runs. [Ab]/[AuNP]=200 and [AuNP]=0.056 nM.

The DCS size distribution of bare commercial-AuNP challenged against 75 mM NaCl shows extensive aggregation (Figure 3.18 A), when conjugated to antibodies ([Ab]/[AuNP]=200) they get

stabilized (Figure 3.18 B). UV-Vis derived aggregation ratios confirmed these findings, and indicated that AuNP@Ab get destabilized starting at 150 mM NaCl (Figure 3.18 C and D). Knowing that plasma's osmolarity is about 300 mOsm of which about 90 % comes from NaCl[137] and knowing that this conjugates are stable towards 75 mM NaCl, a maximum of 50 % (V/V) plasma could be used. This is just a theoretic indication of the stability against the plasma's ionic strength due to NaCl, the effect of the other salts, as well as other molecules was not tested. The only effect tested of other plasma's components was that from human transferrin and some data is available from BSA.

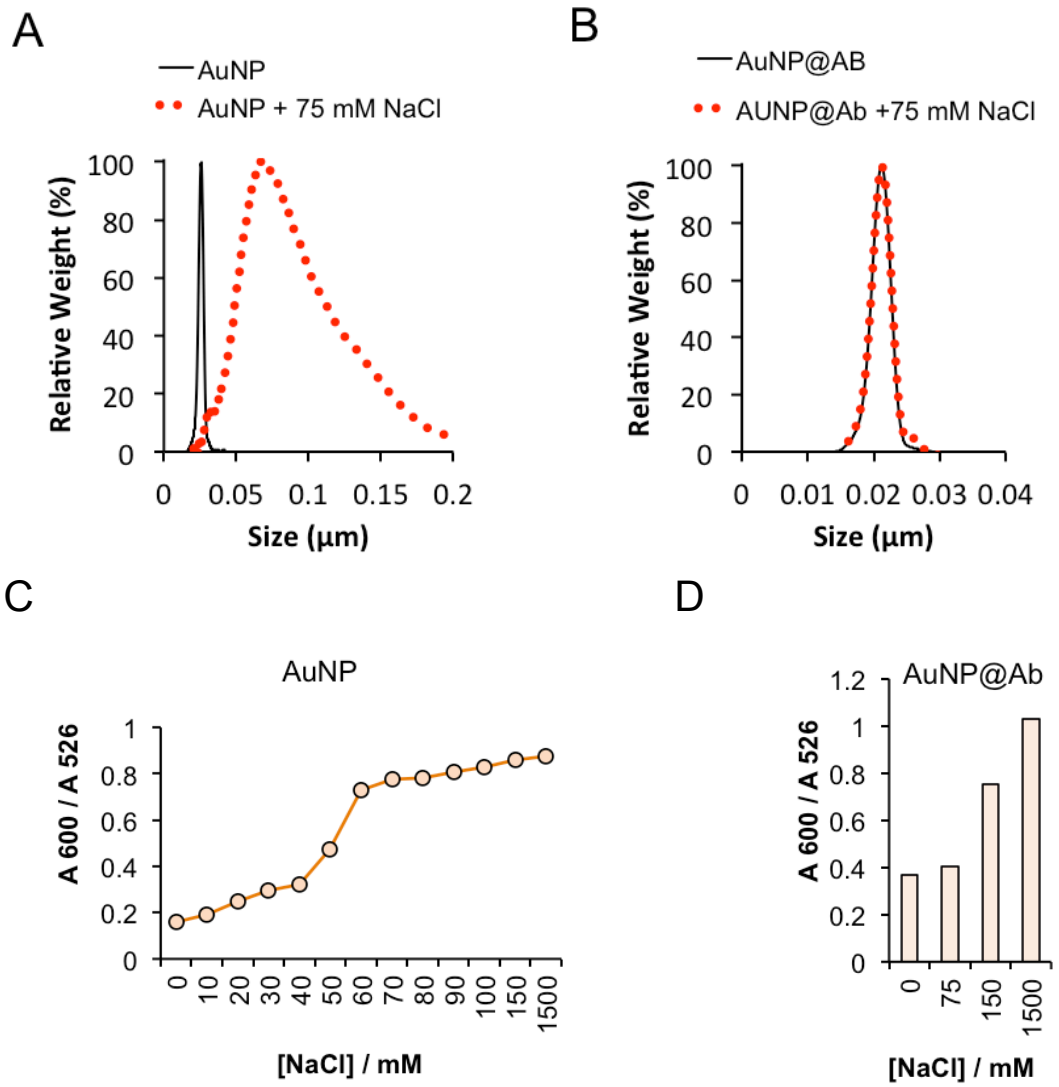

Figure 3.18 Colloidal stability of AuNP and AuNP@Ab upon ionic strength challenge. DCS relative weight size distributions of 75 mM NaCl challenged AuNP (A) and AuNP@Ab (B). Aggregation ratios (A 600 / A 526) of ionic strength challenged AuNP (C) and AuNP@Ab. [AuNP]=0.056 nM for DCS and 0.14 nM for UV-Vis; [Ab]/[AuNP]=200.

As for the homemade-AuNP the pH response is different between AuNP and AuNP@Ab, with AuNP starting to aggregate at pH values below 3, whereas the conjugates start to aggregate at pH values below 6, and then stabilize again at pH values below 4-4.5 (Figure 3.19). The most important information derived from this experiment is that the working range for these conjugates should be above pH 6.

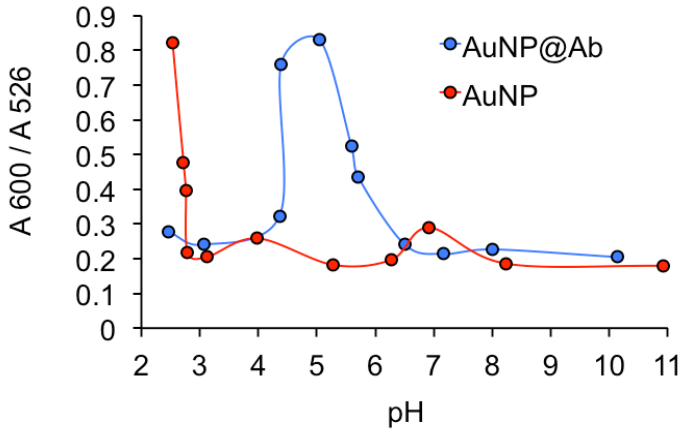

Figure 3.19 Colloidal stability of AuNP and AuNP@Ab upon pH challenge. Aggregation ratio at different pH values for AuNP (red line) and AuNP@Ab (blue line), [AuNP]=0.14nM.

21.1.2. Antibody ratio

DCS, shows an increase in the Ab shell thickness with increasing [Ab]/[AuNP] ratios, after an initial apparent plateau from ratios 25 to 200, Figure 3.20. As no saturation was achieved at the higher ratios tested, and AGE showed saturation starting at ratio 200 (Figure A.5 Appendix), the higher ratio in the first apparent DCS plateau, ratio 200 was selected for the following experiments. For AGE the conjugates are washed (pelleted by centrifugation and the supernatant removed) before loading into the gel, this could remove the soft corona, leaving only the hard corona attached, possibly being responsible for the saturation seen in AGE but not in DCS. However, when washed conjugates are analyzed in DCS, even thought the shell thickness is consistently smaller, no saturation is seen (Figure A.6 Appendix). Possibly AGE allows the separation of the two coronas, i.e. the proteins in the hard corona migrate in the gel bound to the nanoparticles, while the particles in the soft corona are more likely of migrating independently of the nanoparticle. This is to say that the electric field is able to separate the soft corona more efficiency then the washing step.

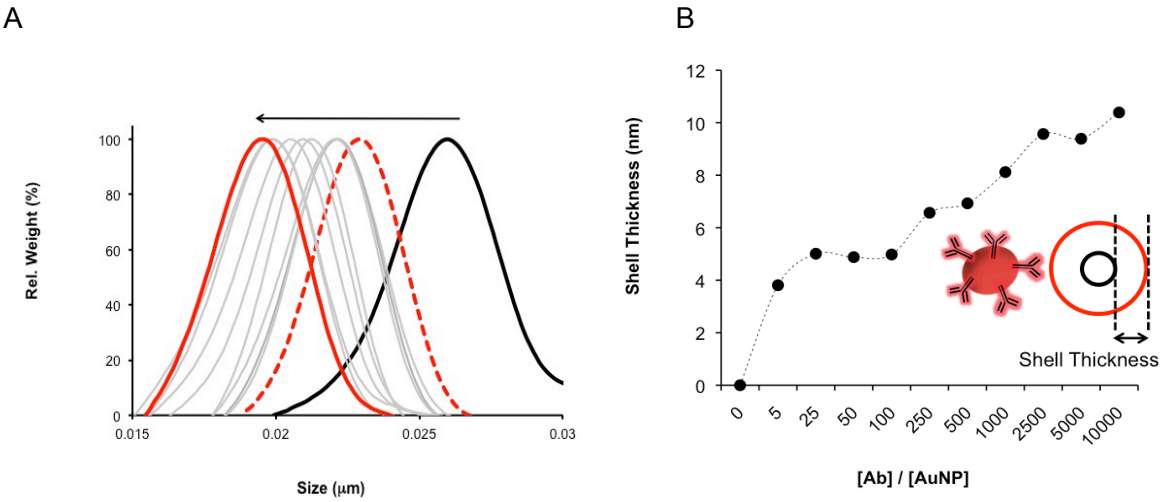

Figure 3.20 Antibody to AuNP ratio. (A) DCS relative wiehgt size distributions of the AuNP@Ab conjugates. AuNP (black line), conjugates at [Ab]/[AuNP] ratios 5 and 10000 (red dashed and continuous lines). (B) The size of the Ab shell (nm) surrounding the AuNP (calculated as described in the Appendix) is represented as a function of [Ab]/[AuNP] ratios, from 0 to 10000. [AuNP]=0.056nM.

21.1.3. Antibody incubation time

The DCS kinetic study of the Ab binding to the AuNP has shown that the binding is really fast, with the shell thickness after 1 minute incubation being 5 nm, with a final variation of less then 2 nm, when compared to the overnight incubation shell thickness (Figure 3.21). An incubation time of 120 minutes (already used for the previous experiment) was used as the minimal incubation time.

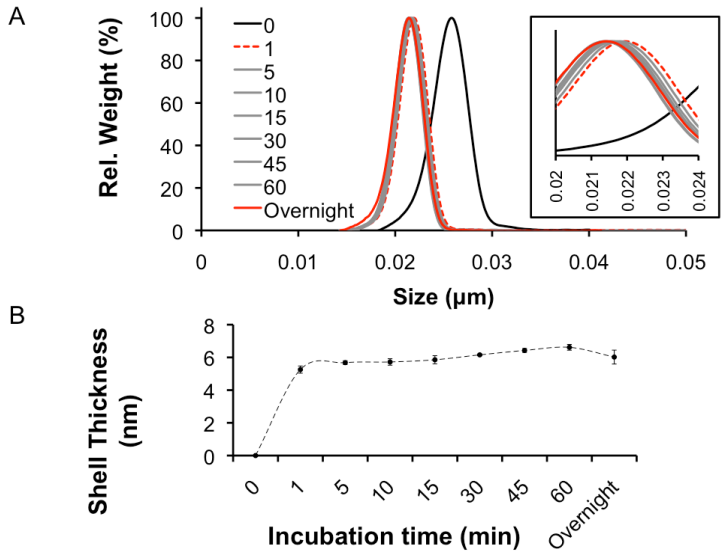

Figure 3.21 Kinetics of Ab binding to AuNPs studied by DCS. (A) DCS relative weight size distribution of AuNP@Ab with incubation times ranging from 1 minute (red dashed line) to overnight incubation (red continuous line), and a shift less then 2 nm, this can be better visualized in the inset. Time 0 minutes (black line), indicates AuNP without antibodies. (B) Shell thickness kinetic evolution of (A). All measurements were run as duplicates. [AuNP]=0.056nM.

21.1.4. Influence of washing and BSA blocking

AuNP@Ab washing from free antibodies and BSA blocking is a common preparatory step in NP based immunoassay area[55,56], to avoid the competitive effect of free antibodies on the antigen binding and to avoid non-specific binding to the nanoparticle surface respectively.

The washing step introduces some aggregation, which is not prevented using BSA blocking, actually more extensive aggregation is seen (Figure 3.22). The following experiments were performed with unwashed, unblocked conjugates, as the properties inferred from the aggregated conjugates would always by biased.

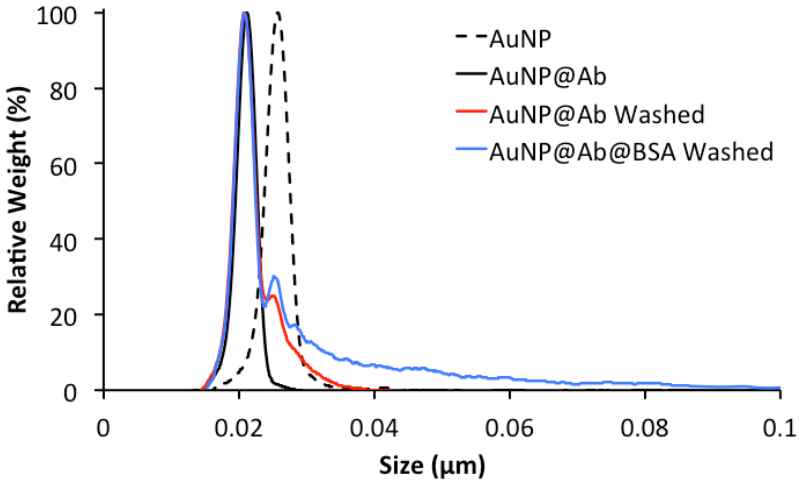

Figure 3.22 DCS relative weight size of AuNP@Ab, their BSA blocked and washed counterparts. AuNP@Ab where washed (centrifugation, followed by supernatant removal and resuspension in PB) to produce "Washed" conjugates; and incubated with BSA followed by washing to produce "BSA blocked" conjugates. [AuNP]=0.056nM and [Ab]/[AuNP]=200.

21.2. Antigen to AuNP@Ab conjugation

21.2.1. Ag to AuNP@Ab ratio

Incubation of AuNP@Ab with Ag (120 minutes incubation) at different ratios showed a bimodal population distribution indicating the presence of AuNP@Ab with and without the target Ag. This bimodal distribution could be perfectly fitted using two Gaussian distribution curves (Figure 3.23 B). With increasing Ag concentration an increase in the AuNP@Ag population was detected (Figure 3.23 A), that could be expressed by an increase in the area of the fitted peak (Figure 3.23 C).

Washed and BSA blocked conjugates where also able to bind the Ag, but they where less efficient (Figure A.7 Appendix).

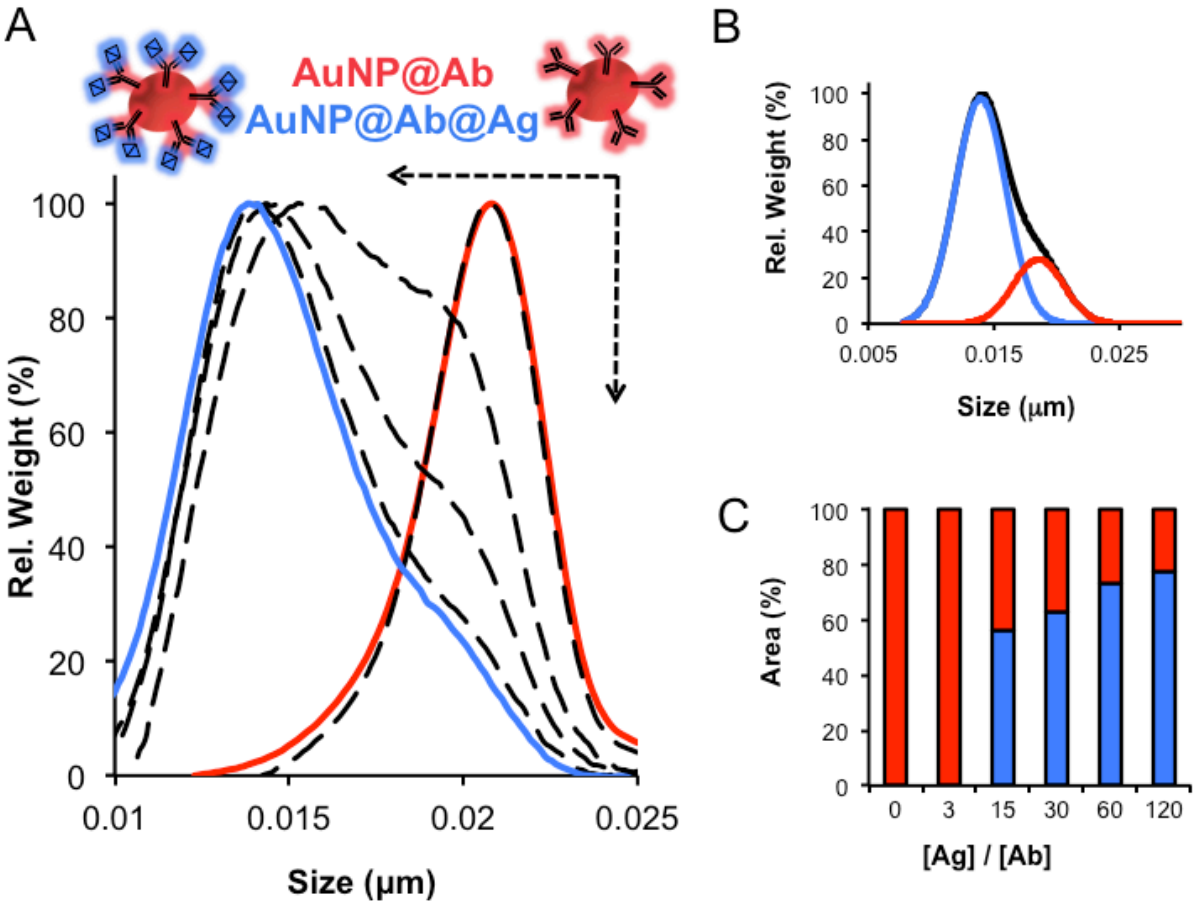

Figure 3.23 DCS relative weight size distributions of AuNP@Ab incubated with the Ag. (A) Upon incubation of AuNP@Ab conjugates (red line) with Ag at increasing Ag to Ab molar ratios, a change in the weight distribution is seen (dotted arrows) from a near Gaussian distribution when there is no Ag, towards a bimodal weight distribution when the target Ag is captured. Blue line corresponds to the higher ratio tested. (B) The experimental curves (black line, [Ag]/[Ab]=60) could be fitted using two Gaussian distribution curves (blue line: AuNP@Ag, red line: AuNP@Ab). (C) Relative area of the fitted Gaussian distributions, columns are color codded as in (B). Ag was added at the Ag to Ab molar ratios of 3, 15, 30, 60 and 120; corresponding to final concentrations ranging from 4.0 to 160 µg mL^{-1}. [AuNP]=0.056nM and [Ab]/[AuNP]=200.

21.2.2. Antigen incubation time

The kinetic study of the Ag binding ([Ag]/[Ab]=30) showed that no saturation was achieved (Figure 3.24), there is always a bimodal distribution containing both AuNP@Ab and AuNP@Ab@Ag. Overnight incubation (approximately 12 hours) resulted in sample aggregation. (Figure A.8 Appendix) An incubation time of 120 minutes was selected for subsequent experiments.

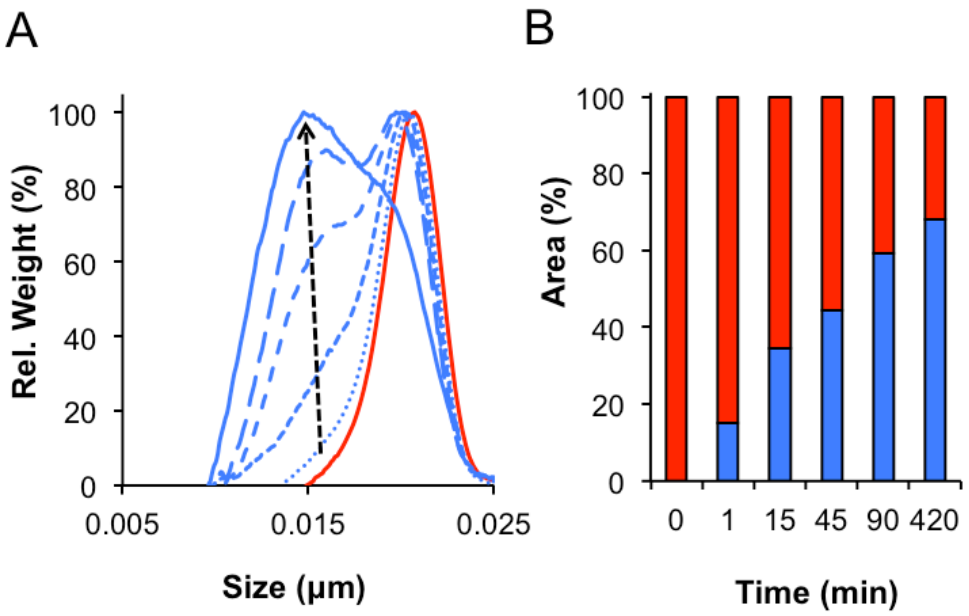

Figure 3.24 DCS kinetic study of the Ag binding to AuNP@Ab. (A) DCS relative weight size distributions. Data were collected at 0 (red line, AuNP@Ab no Ag added), 1, 15, 45, 90 and 420 minutes (blue line). (B) The relative area of the AuNP@Ab@Ag Gaussian distribution fit (blue columns) increases with time. [AuNP]=0.056nM, [Ab]/[AuNP]=200, [Ag]/[Ab]=30.

As there is no washing from free antibodies, these might be competing with the AuNP associated antibodies for binding the Ag, and this competition might be slowing down the binding to the AuNP@Ab. If this is true, washed conjugates would bind more Ag at the same incubation time. As mentioned previously no improvement was found (Figure A7 Appendix).

The influence of the AuNP surface chemistry and of the Ag buffer on the binding extent was also studied by DCS. No improvements were found (Figure A.9 and A.10 and discussion therein in the Appendix) regarding the present conditions, commercial-AuNP with the PBS as the Ag's buffer, as assessed by the increase in the shell thickness upon Ag binding to the AuNP@Ab conjugates.

21.3 Influence of Trf on the Ag to AuNP@Ab binding

21.3.1. DCS

When Ag is incubated in the presence of increasing Trf concentrations, there is an increase in the proportion of AuNP@Ab to that of AuNP@Ab@Ag, i.e., Trf as a negative effect on the binding of the Ag to the AuNP@Ab (Figure 3.25 A and B). Trf might interact with the antigen in a way that makes the antigen's epitope that is recognized by the antibody unavailable.

When AuNP@Ab are incubated with Trf (Trf concentration rage equal to that used for the Ag in Figure 3.23) no changes in the DCS size distribution are detected (Figure 3.25 C). When AuNP

without antibody are used the shell thickness increases with increasing Trf concentration (Figure 3.25 D) proving that Trf binds to bare AuNP in a non-specific manner. Therefore the AuNP@Ab surface is a specific surface that binds selectively to the Ag and avoids the binding of non-target proteins, such as Trf.

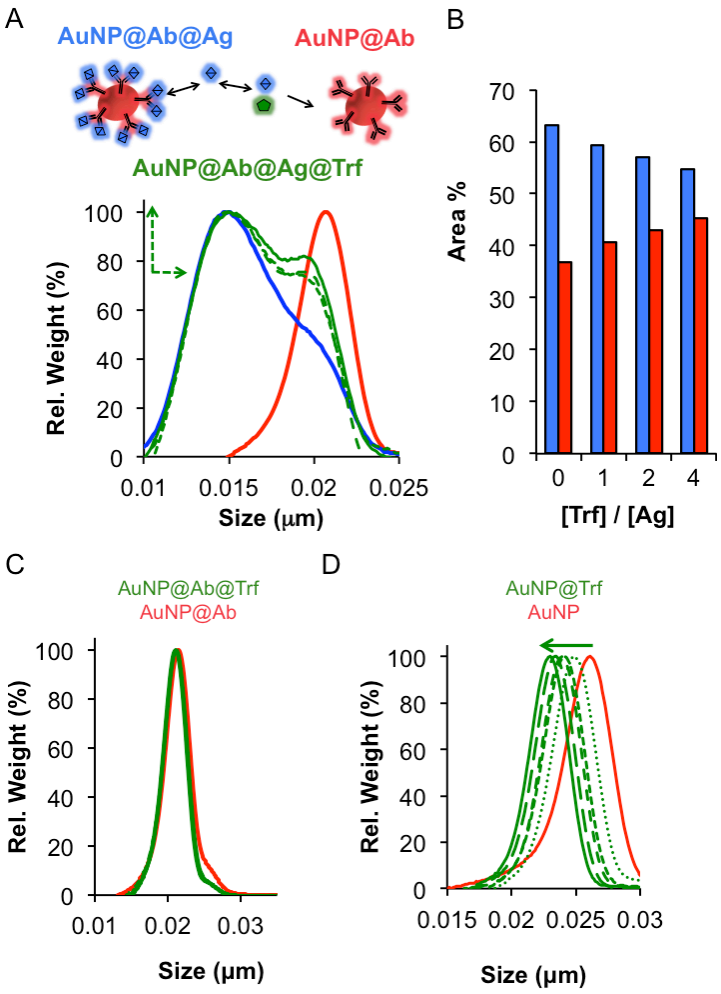

Figure 3.25 DCS assessment of the Ag binding specificity and Trf inhibition. (A) DCS size distributions of AuNP@Ab incubated with Ag ([Ag]/[Ab]=30, [Ag]=40 μg.mL^{-1}), and increasing amounts of Trf ([Trf]/[Ag] ratios of 1, 2 and 4, corresponding to 40, 80 and 160 μg.mL^{-1} of Trf). (B) The relative area of the AuNP@Ab@Ag Gaussian distribution fit (blue) decreases with increasing [Trf]/[Ag] ratio. DCS size distributions of AuNP@Ab (C) incubated with Trf, at [Trf]/[Ab] ratios of 3, 25, 30, 60 and 120; (D) AuNP incubated with Trf, Trf concentration equal to those used in (C). [AuNP]=0.056nM and [Ab]/[AuNP]=200.

21.3.2. AGE

Upon Ag binding, AuNP@Ab conjugates migrate less, in a concentration dependent manner (Figure 3.26 A). When Trf is used instead of the Ag, there is no observable shift in the AuNP@Ab's mobility (Figure 3.26 A, Inset). Considering the electrophoretic mobilities averaged from three independent experiments, there is some non-specific binding (Figure 3.26 C). Nonetheless, the

conjugates are much more sensitive to the Ag then to Trf (see below). Sensitivity is defined as the change in the analytical response caused by a small change in the analyte concentration[138].

When the Ag is tested in the presence of increasing Trf concentrations ([Trf]/[Ag] ranging from 1 to 10), the resulting AuNP@Ab@Ag@Trf bands migrate more then AuNP@Ab@Ag (Figure 3.26 B), indicating that Trf prevented the Ag binding to AuNP@Ab. The mobility was less than that of the AuNP@Ab, indicating that Ag binding is not completely prevented. Considering the averaged electrophoretic mobilities from three independent experiments (Figure 3.26 D), the mobility of AuNP@Ab@Ag@Trf (green line) is consistently between the mobilities of AuNP@Ab (red line) and AuNP@Ab@Ag (blue line).

These observations are in good agreement with DCS results (Figure 3.25) were Trf caused a partial inhibition of the Ag binding ([Trf]/[Ag] ranging from 1 to 4).

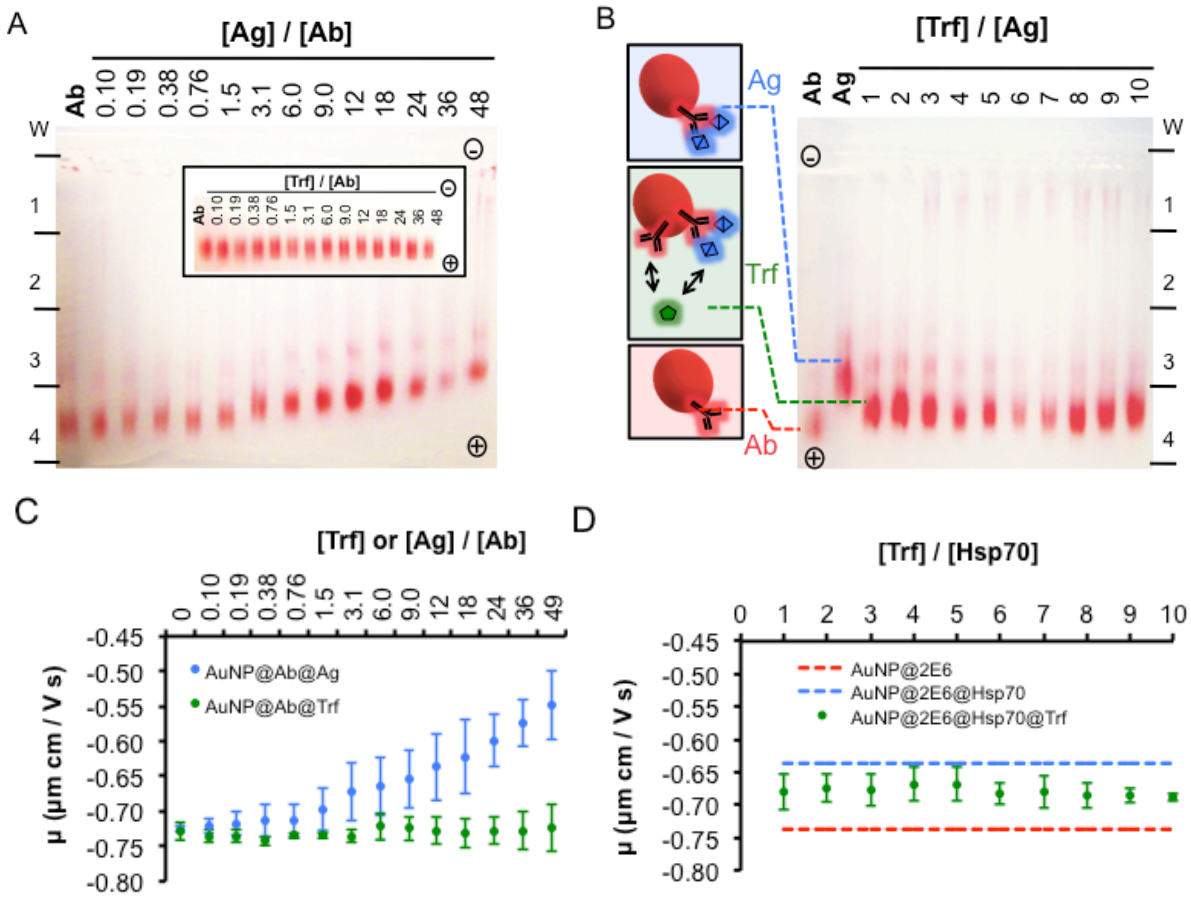

Figure 3.26 AGE assessment of the Ag binding specificity and Trf inhibition. (A) Digital picture of AuNP@Ab@Ag AGE; inset: digital picture AuNP@Ab@Trf AGE. Lanes: "0.10" to "48" indicate Ag (or Trf) to Ab molar ratios, corresponding to concentrations ranging from 0.22 to 57 μg mL^{-1}; "Ab" indicates AuNP@Ab. (B) Digital picture of AuNPs@Ab@Ag@Trf AGE. Lanes: "1" to "10" indicate the Trf to Ag molar ratios, corresponding to Trf concentrations ranging from 29 to 290 $\mu g.mL^{-1}$; "Ag" indicates AuNP@Ab@Ag (at an [Ag]/[Ab]=24 and [Ag]=29 $\mu g.mL^{-1}$), "Ab" indicates AuNP@Ab. Electrodes positioning: "-" and "+"; wells: "w"; migration distance (cm) indicated by vertically arranged numbers. (C) and (D) apparent electrophoretic mobilities (μ) calculated from the gels displayed in (A) and (B) respectively. Conjugates composition is color codded. [AuNP]=0.28nM, [Ab]/[AuNP]=200.

21.3.3. Fluorescence

After DCS and AGE, a spectroscopic technique was used to evaluate the Ag binding to the AuNP@Ab conjugates. The measured fluorescence intensity (F.I.) increased with increasing Ag concentration (Figure 3.27 blue line). When Trf was used instead of the Ag, the concentration dependent fluorescence increase is not observed (Figure 3.27 green line). Statistically there is a significant increase in the FI in respect to the blank for some concentrations, indicating that some Trf binding occurs (see below). However, the response is much more sensitive to the Ag then to Trf.

When both the Ag and Trf (at the same concentration) are tested in the assay (Figure 3.27, red line), the FI is significantly smaller, then that detected for the Ag only (Figure 3.27, blue line), implying a negative influence of Trf on the Ag binding to the AuNP@Ab.

The binding inhibition (Figure 3.27, inset) was shown to decrease with decreasing concentration of incubated proteins. If this inhibition was constant for the concentrations tested, as the proteins were incubated in equal concentrations, for each experimental data point, it would be an indication that the negative influence is due to the interaction of Trf with the Ag, as this is not the case, there might be a direct interaction of the Trf with the AuNP@Ab that avoids the binding of Ag.

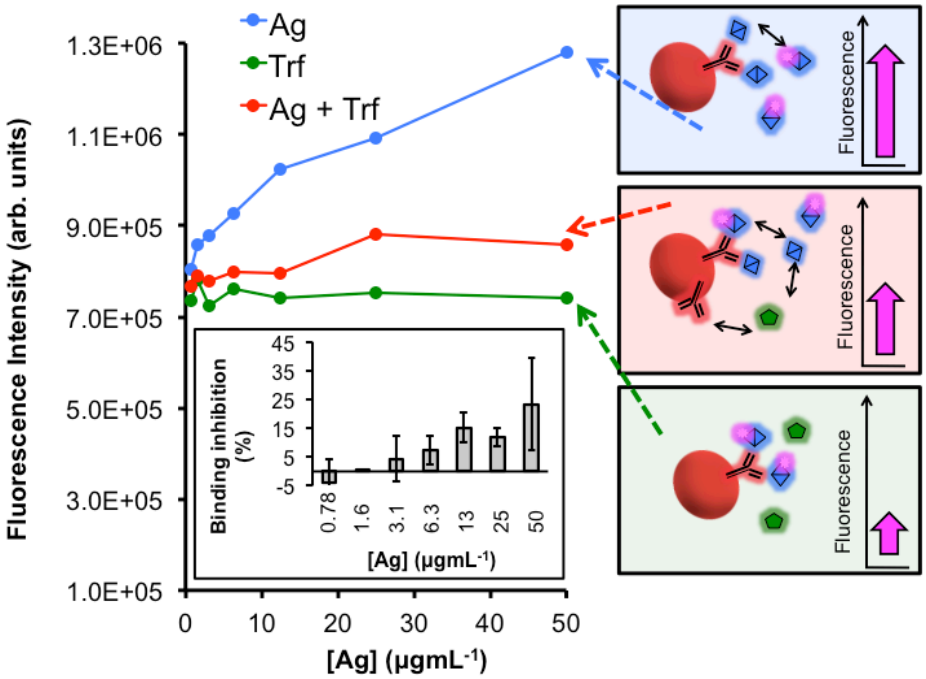

Figure 3.27 Fluorescence assessment of the Ag binding specificity and Trf inhibition. Experiments were performed with Ag only (blue), with Trf only at the same concentration as used for the Ag only (green) or with Ag in the presence of an equal concentration of Trf (red). The average results from two independent experiments are plotted. Lines were inserted to guide the eye. The Ag to Ab ratios used, 765 to 12.0, correspond to final antigen (and also of Trf) concentrations from 50 to 0.78 µg mL^{-1}. Inset: Ag binding inhibition in the presence of Trf, expressed as the decrease (%) of the CyAg concentration, calculated as follows: Binding Inhibition(%)=[(([CyAg]/$[CyAg]_o^{Ag}$)-([CyAg]/$[CyAg]_o^{Ag+Trf}$))/([CyAg]/$[CyAg]_o^{Ag}$)]x100, where the superscripts Ag and Ag+Trf, indicates that Ag only, or Ag with Trf where present. [AuNP]=0.0047nM,[Ab]/[AuNP]=200.

21.4. Analytical performance of the Ag binding characterization methods

21.4.1. Linear response regions

Linear response regions were identifiable for the techniques used in the Ag binding characterization. In the case of DCS, an insufficient number of experimental data points were tested for the correlation to be statistically significant (Figure 3.28). In some cases, to obtain linearity between assays and sample concentrations, the test data may need to be subjected to a mathematical transformation prior to regression analysis[135]. Different mathematical transformations were exploited (Table A.1 Appendix), and the plots are presented in Figure A.11, A.12 and A.13 in the Appendix, along with accompanying discussion on how the different plots were selected.

Note that the experimental results for the commercial-AuNP fluorescence immunoassay exhibited in Figure 3.28 A, are not the same as those exhibited in Figure 3.27 (blue lines) although the experimental conditions and procedure are the same.

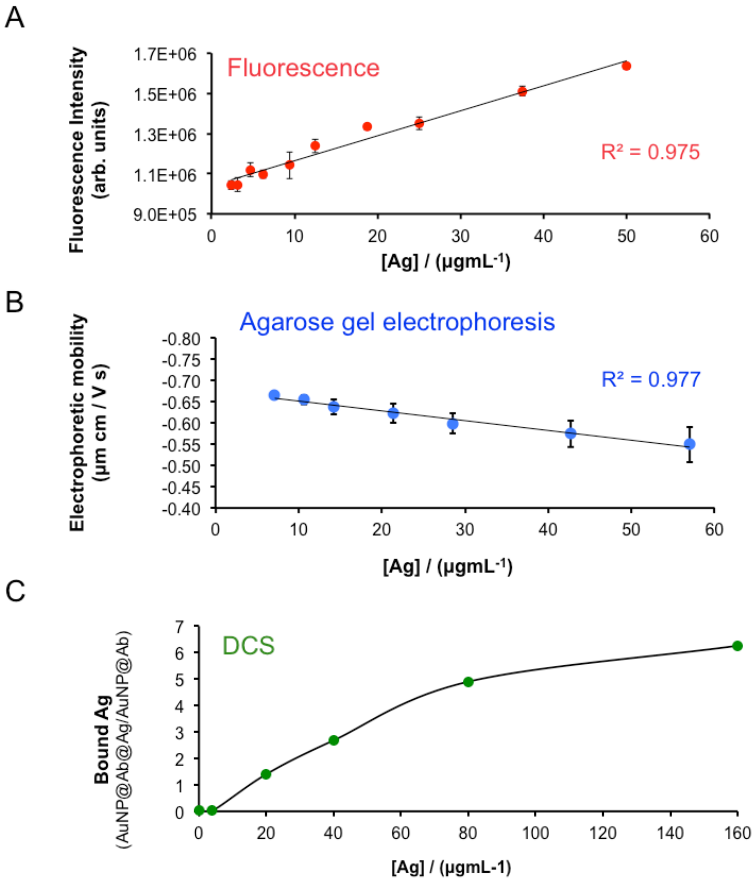

Figure 3.28 Analysis of the [Ag] *vs* analytical response plots for the Ag binding characterization techniques. In fluorescence (A) the analytical response is the fluorescence intensity, in AGE (B) the analytical response is the electrophoretic mobility and for DCS the analytical response is the ratio of bound Ag defined as the quotient between the relative weight values at the sizes of 14 and 19 nm, which are the approximate sizes of the AuNP@Ab@Ag and AuNP@Ab populations. Solid lines represent linear regression fits. In (C) an apparently linear response region extends from 4 to 80 µg mL^{-1}, the solid line is presented to guide the eye.

21.4.2. Analytical parameters for quantitative comparison of the immunoassays performance

Besides defining the linear response regions in immunoassays, others questions need to be answered to understand its analytical capabilities. Can the Ag analytical signal be obtained with an non-specific molecule? Is the Ag analytical signal significantly diminished in the presence of a non-specific competitor?

After an extensive literature review[135,138,139,140,141,142,143,144,145,146], it was found that a deeper discussion on the meaning of analytical parameters already presented is necessary. Reporting the smallest concentration that can be detected with a reasonable certainty by the immunoassays is certainly necessary. This performance is commonly characterized by the statistical limits of detection (SLoD) and quantification (SLoQ)[142]. The following definitions of SLoD given by IUPAC and the American Chemical Society (ACS), respectively, are commonly accepted:

(i) The limit of detection, expressed as a concentration or quantity, is derived from the smallest measure that can be detected with reasonable certainty for a given analytical procedure[139].

(ii) The limit of detection is the lowest concentration of an analyte that the analytical process can reliably detect[140].

The SLoQ has been introduced to provide supplemental statistical separation of the blank measurement and true analyte signal distributions and proposed because the SLoD was not considered satisfactory for quantitative analysis[142]. Thus, the SLoQ refers to the smallest concentration or mass that can be quantitatively analyzed with reasonable reliability by a given procedure[142]. A numerical definition is given in a ACS document[140], and according to IUPAC definition the limit of detection can be estimated as[139]:

$$SLoD = \frac{k \times SD}{m} \qquad \text{Eq.40}$$

where SLoD, is the statistically estimated limit of detection, *SD* is the standard deviation of blank measurements, *m* is the sensitivity of the method, i.e. the slope of the calibration curve, and *k* is a numerical factor chosen accordingly to the confidence level desired[139].

A value of *k* equal to 3 has been recommended by IUPAC[146] and other authors[135], however, no agreement exists, and 2, 2.5, or 3 are commonly used[138]. As for the SLoQ, a *k* factor of 10 can be seen in some examples[66,135,140].

The IUPAC formula for calculating the statistical limit of detection (SLoD) could be applied for the fluorescence results plotted as Fluorescence Intensity F.I. (arb. units) *vs* [Ag], but not for

Relative Fluorescence Increase, F.Inc. (%) *vs* [Ag]. Calculating the *SD* from the F.Inc. (%) of blank measurements is impossible because, the F.Inc. (%) of the blank can not be calculated (see Eq.39). One could think of using the *SD* and *m* values from the F.I. (arb. units) *vs* [Ag] plot instead, but this is not a correct approach as: i) the linear region might be different between the F.I. vs [Ag] and the F.Inc. *vs* [Ag] plots; *m* and *SD* are also different, therefore the calculated SLoD will be different, and incorrect. For example, in the commercial-AuNP fluorescence immunoassay (Figure 3.28 A), the *SD* and *m* from the F.I. *vs* [Ag] plot are, 1538 and 12438 respectively. This will give SLoD and SLoQ of 0.37 and 1.2 $\mu g.mL^{-1}$, respectively; if the sensitivity, *m*, from the F.Inc. (%) *vs* [Ag] is used instead, the SLoD and SLoQ will have the values of 7279 and 24264 $\mu g.mL^{-1}$, completely meaningless values.

An alternative approach, where the signal of the blank or its concentration are not necessary is given by the International Conference on Harmonisation of Technical Requirements for Registration of Pharmaceuticals for Human Use (ICH)[135]:

$$SLoD = \frac{3.3 \times SD}{m} \qquad \text{Eq.41}$$

$$SLoQ = \frac{10 \times SD}{m} \qquad \text{Eq.42}$$

where *SD*, the standard deviation of the response can be evaluated by the *SD* of the y-intercepts of the regression lines. The SLoD and SLoQ reported for the homemade-AuNP immunoassay (section 20) are according to the ICH definition, as it avoids the problem of obtaining the *SD* of the blank from a F.Inc. (%) *vs* [Ag] plot.

Besides this consideration of the applicability of the equations for estimating SLoD and SLoQ, according to different international regulation bodies, the practical relevance of these estimated values should also be considered. For example, in the commercial-AuNP fluorescence immunoassay (Figure 3.28 A) the SLoD is 0.72 $\mu g.mL^{-1}$ (Eq. 51, ICH), however, the first [Ag] whose F.I. was significantly above the blank, was 3.1 $\mu g.mL^{-1}$, considering a significance level given by the average ± 3 x SD. This means that the F.I. Sample – 3 x *SD* of the sample is higher then the F.I. Blank + 3 x *SD*. As antigens concentrations down to 0.22 $\mu g.mL^{-1}$ have been tested and 3.1 $\mu g.mL^{-1}$ was the first concentration to be significantly above the blank, the estimated SLoD, is not a good indication of the limit of detection of the assay, i.e. the smallest concentration that can be detected with reasonable certainty. Facing this evidence of lack of physical meaning of the SLoD, alternative analytical parameters were defined to estimate the minimal detectable Ag concentration [48], the minimal specifically detected Ag concentration (LoSD), the minimal inhibiting Trf concentration (LoINH), and the minimal non-specifically detected Trf concentration (LoIB):

(i) LoD was considered to be the minimal [Ag] whose analytical signal was significantly above the blank signal (avergae ± *SD* for AGE, and average ± 3 x *SD* for fluorescence);

(ii) LoSD was considered to be the minimal [Ag] whose analytical signal (avergae ± *SD*) was significantly higher than its corresponding analytical signal (avergae ± *SD*) in the presence of Trf only;

(iii) LoINH is meant to express the minimal [Trf] that could significanlty (average ± *SD*) decrease the analytical signal of the AuNP@Ab@Ag conjugates;

(iv) LoIB is meant to express the minimal [Trf] concentration that could significantly (average ± 3 x *SD*) increase the analytical signal of AuNP@Ab conjugates.

Further detail on the significance level for each technique is presented in the Appendix.

21.4.3. Quantitative comparison and physical meaning of the immunoassays performance

In Table 3.1, the LoD, LoSD, LoINH and LoIB are presented for DCS, fluorescence and AGE on commercial-AuNP.

Table 3.1 Analytical performance of the Ag binding characterization techniques

Physical Parameter	Analytical Parameter	DCS	Fluorescence	AGE
			$\mu g.mL^{-1}$ #	
Detection	Limit of Detection (LoD)	20	3.1	3.6
Specific detection	Limit of Specific Detection (LoSD)	20	13	11
Binding inhibition	Limit of Inhibition (LoINH)	40	6.3	29
Non-specific binding	Limit of Non-specific Binding (LoIB)	NA	NA*	7.2
			µg	
	LoD	2.0	0.20	1.2
	LoSD	2.0	0.75	3.6
	LoINH	4.0	0.38	9.6
	LoIB	NA	NA	2.4
			[Ag]/[Ab]	
	LoD	15	48	3.0
	LoSD	15	194	9.0
	LoINH	30	96	24
	LoIB	NA	NA	6.0

#, in the case of LoD and LoSD, the quantities - $\mu g.mL^{-1}$, µg, and [Ag]/[Ab]- refer to the Ag, in the case of LoIB and LoINH, the quantities refer to Trf, and the "[Ag]/[Ab]" refers to the Trf to Ab ratio, not the Ag to Ab ratio.*LoIB varied between the different days of analysis, values higher and lower than the background signal were found in a random way.

Fluorescence was more sensitive regarding the Ag detection (LoD), specific detection (LoSD) and detection of Trf inhibition (LoINH) then AGE and DCS in a *per* mass basis, while DCS was more sensitive than AGE in the Ag specific detection (LoSD) and detection of Trf inhibition (LoINH), also on a *per* mass basis.

The fact that the LoSD is the same as the LoD for the DCS, but for fluorescence and AGE the LoSD is higher then the LoD, indicates that DCS is less sensitive to the detection Trf non-specific binding, actually it did not detect Trf at all.

As DCS did not detect the Trf non-specific binding, the LoIB cannot be calculated, for AGE, the LoIB was 11 $\mu g.mL^{-1}$, starting at 11 $\mu g.mL^{-1}$ non-specific Trf binding was detected (it retarded the AuNP@Ab conjugates migration towards the positive electrode, for fluorescence non-specific binding was also detected, but in a random way, therefore a numerical value cannot be assigned.

The home made AuNP-fluorescence immunoassay was not tested regarding its specificity, the analytical parameters comparable to the commercial-AuNPs immunoassays are presented on Table 3.2. The homemade-AuNP fluorescence immunoassay had similar LoD to the commercial-AuNP immunoassays, but the detection range was only spanned half of the commercial–AuNPs detection range. The SLoD and SLoQ for both ICH and IUPAC recommendations are presented, to illustrate the fact that, according to the variables being plotted, these statistical derived parameters might give values that are meaningless, for example, in the AGE immunoassay the SLoD and SLoQ calculated by the ICH recommendations, are out of the detection range, but if the IUPAC recommendations are used instead, the values are within the detection range.

Table 3.2. Comparable analytical performance parameters of homemade- and commercial-AuNP immunoassays

	Fluorescence, homemade-AuNP		Fluorescence, commercial-AuNP		AGE commercial-AuNP	
Detection range	8.2-24		2.3-50		7.1-57	
LoD	2.3		3.1		3.6	
	IUPAC	ICH	IUPAC	ICH	IUPAC	ICH
SLoD	NA	2.4	0.37	0.72	6.0	63
SLoQ	NA	7.3	1.2	2.220	192	

NA, not available. Concentrations are in $\mu g.mL^{-1}$.

21.4.3.1. Analysis of the AGE results

Focusing on the information obtained from AGE, the LoSD was 11 $\mu g\ mL^{-1}$, meaning that for concentration smaller than 11 $\mu g\ mL^{-1}$ ([Ag]/[Ab]=9.0), the retardation of the mobility of AuNP@Ab@Ag conjugates is not significant (Average ± *SD*) in respect to the mobility of AuNP@Ab@Trf conjugates.

The LoD was 3.6 $\mu g.mL^{-1}$, in this case the significance level was average ± SD, because with a level of ± 3 x SD, only one of the tested Ag to Ab ratios would be significantly above the blank, in disagreement with the mobilities of the bands seen in the gel.

The LoIB was also 7.2 $\mu g.mL^{-1}$, meaning that the retardation, i.e. less migration towards the positive electrode, of the AuNP@Ab conjugates when incubated with Trf is significant (average ± 3 x *SD*) for Trf concentrations ≥ 7.2 $\mu g.mL^{-1}$.

21.4.3.2 Analysis of the fluorescence results

The fact that for fluorescence the LoSD is 13 $\mu g.mL^{-1}$ indicates that the binding of the Ag can only be considered specific for the last 3 highest Ag concentrations tested, 13, 25 and 50 $\mu g.mL^{-1}$ (Figure 3.27, blue line) below this concentrations the fluorescence intensities observed for the AuNP@Ab@Ag are not significantly different from the AuNP@Ab@Trf fluorescence responses.

For the sake of clarity, it is important to further discuss the physical meaning of the fluorescence response when only Trf is tested (AuNP@Ab@Trf+CyAg). In all the experiments (fluorescence, AGE, DCS) AuNP were incubated with all the proteins at the same time for two hours at RT, the only difference being that for the fluorescence, only after the two hours incubation CyAg is added, and then allowed to incubate another hour at RT. Therefore, the labeled Ag acts as a reporter of the nanoscale interactions taking place in the reaction mixture. The analytical signal of Trf was only significantly above the blank (AuNP@Ab+CyAg) for some experimental points, in a random way, not concentration dependent. Trf is able to somehow interact with the AuNP@Ab preventing the binding of CyAg, giving rise to fluorescence intensity values significantly above the blank.

Being sensitivity the change in the analytical response caused by a small change in the analyte concentration[138], it can be readily concluded that the AuNP@Ab conjugates have a sensitive and specific response to the Ag, while the response to Trf is random, this response is in fact a background signal, with very low amplitude in comparison to the Ag response.

When both Ag and Trf (at the same concentration) are tested in the assay (Figure 3.27, red line), the F.I. is smaller than for the Ag alone (Figure 3.27, blue line), implying a negative influence of Trf on the Ag binding to the AuNP@Ab. This binding inhibition is significant, i.e. the F.I. of the AuNP@Ab@Ag@Trf is significantly lower then the F.I. of AuNP@Ab@Ag starting at Trf and concentrations (and Ag, as they were tested in a 1 to 1 molar ratio) of 6.3 $\mu g.mL^{-1}$, the value of the LoINH. In practical terms this means that the decrease in the Ag fluorescence intensity can be attributed to the presence of Trf when both Ag and Trf are incubated for the four higher concentrations

tested, 6.3, 13, 25 and 50 μg.mL^{-1}. As previously observed this binding inhibition (Inset in Figure 3.27) decreases with decreasing concentration of incubated proteins, a possible indication that it is the Trf interaction with the AuNP@Ab that prevents the binding of the Ag. Therefore we cannot unequivocally assign the binding inhibition to the Trf interaction with the Ag or with the AuNP@Ab.

Rotello and coworkers [147,148] have developed sensing platforms in which different proteins can be distinguished in complex mixtures depending on their relative affinity towards a positively charged (and fluorescent) coating on the surface of nanoparticles or towards green fluorescent protein (GFP), whose fluorescence is quenched when bound to these particles. Fluorescence is recovered when a protein with higher affinity towards the particle is present, displacing the GFP from the nearby quencher surface. The fluorescence can be further quenched if the analyte protein has more affinity towards GFP. Our findings of the negative influence of Trf on the Ag binding to the Ab are interesting, as they were not completely expected, but they can be explained when considering the fact that non-specific interactions between proteins can avoid the recognition of the epitopes of one of these proteins by a specific antibody.

21.4.3.3 Analysis of Trf binding inhibition by the three techniques

From Table 3.1 it was concluded that fluorescence was the most sensitive technique to determine Trf inhibition of the Ag binding, because the minimal Trf concentration that inhibited the Ag binding was 6.3 μg.mL^{-1}, while for AGE it was 29 μg.mL^{-1}. However, for AGE, Trf concentrations lower then 29 μg.mL^{-1} were not tested. Another way of comparing the sensitivity of AGE, DCS and fluorescence to the Trf inhibition of the Ag binding would be the comparison of the extent of Ag binding inhibition at the same Ag and Trf concentrations, for the three techniques. In this case, [Trf]/[Ag]=1 was available for all techniques, and similar Ag concentrations were also available, namely, 40, 29 and 50 μg.mL^{-1} for DCS, AGE and fluorescence, respectively. However the Ag to Ab ratios are quite different, [Ag]/[Ab]=30, 24 and 765 for, DCS, AGE and fluorescence, respectively. From these results it follows that under the available most comparable experimental conditions, AGE is the most sensitive technique, as it detect a larger extent (in percentage of the analytical signal) of Ag binding inhibition, for the same (comparable) Ag concentration (Figure 3.29).

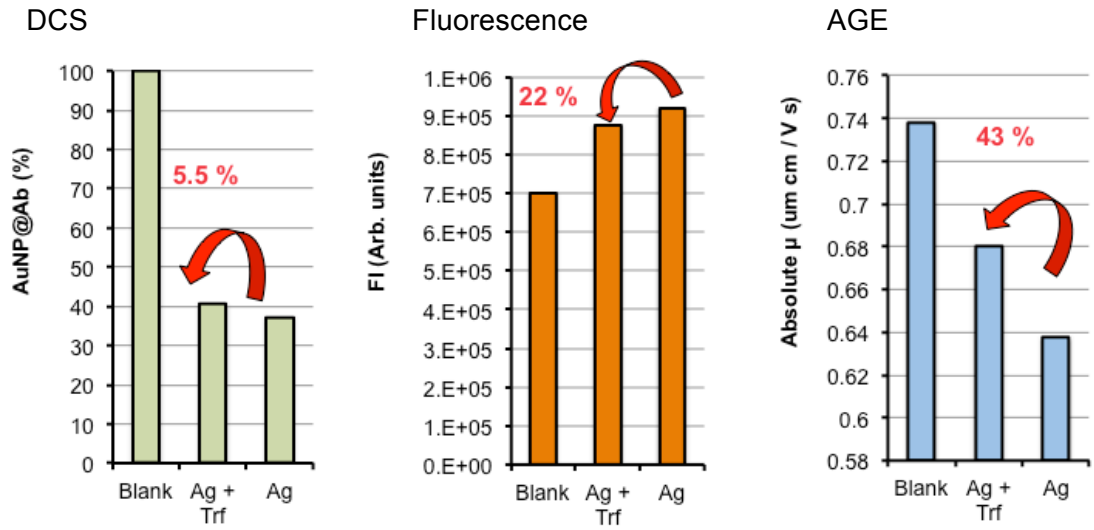

Figure 3.29 Trf binding inhibition assessed by AGE, DCS and Fluorescence. Blank sample stands for AuNP@Ab, Ag+Trf stands for AuNP@Ab@Ag@Trf, and Ag stands for AuNP@Ab@Ag. In fluorescence CyAg is also present in all the conditions. Inhibition percentage is indicated. Binding inhibition (%) = $[((AS^{Ag+Trf}-AS^{Blank})-(AS^{Ag}-AS^{Blank}))/(AS^{Ag}-AS^{Blank})]x100$, where AS is the analytical signal, i.e. the yy axis variable. [AuNP]=0.0047, 0.056 and 0.28 for Fluorescence, DCS and AGE respectively. [Ab]/[AuNP]=200 and [Trf]/[Ag]=1.

21.5. Influence of plasma in the antigen to antibody binding

21.5.1. AuNPs and AuNP@Ab conjugates stability in plasma

The position of the major peak for AuNP (blue lines) and AuNP@Ab (red lines) incubated with increasing plasma concentrations (Figure 3.30) did not change (shifted less then 0.7 nm), indicating that the size and density of their protein coronas was very similar despite the AuNP@Ab already having a pre-adsorbed layer of Ab, before incubation with plasma. Bare AuNP (blue lines) exhibited a smaller peak not seen in AuNP@Ab (orange lines). If this smaller peak is caused by sample aggregation, it is an indication that the AuNP were less stables then the AuNP@Ab in the presence of plasma.

The size distributions were not significantly different between them regarding the effect on the NPs stability, only for the AuNP (blue lines) one condition (0.1 % plasma) exhibited a larger second peak as compared to the other plasma concentrations.

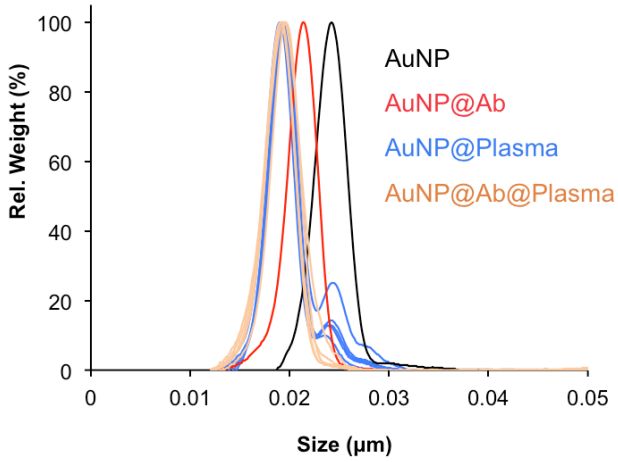

Figure 3.30 DCS size distributions of the AuNPs and AuNP@Ab in plasma. AuNP (blue lines) and AuNP@Ab (orange lines) were incubated with increasing plasma concentrations: 0.1, 0.5, 1.0, 1.5 and 3.0 %, corresponding to natural occurring Trf concentrations of 4.0, 20, 40, 60 and 120 µg mL^{-1}. AuNP (black line) and AuNP@Ab (red line) in the absence of plasma are shown as controls. [AuNP]=0.056nM and [Ab]/[AuNP]=200.

21.5.2. Detection of Ag binding in plasma

Ag binding to AuNP@Ab ([Ag]/[Ab]=30) in 2% (V/V) plasma could be detected (Figure 3.31 A), and the DCS size distribution (continuous green line) could be fitted to a bimodal population distribution using two Gaussian distributions (dotted green lines). Comparing the size distributions in the absence and presence of plasma (at the same Ag concentration, [Ag]/[Ab]=30) less Ag is bound in the presence of plasma (inset in Figure 3.31 B). Similar conclusions are found for the other Ag concentrations tested in 2% plasma (Figure A.14 Appendix).

The areas of the AuNP@Ab@Ag fitted Gaussian distributions increased with increasing Ag concentration in 2 % plasma, however the fitted areas were not significantly different in the absence and presence of plasma (data not shown). This is in contradiction to the DCS size distributions shown in Figures 3.31 A and B in which a clear inhibition of the Ag is seen in the presence of plasma.

This is a limitation of the fitting protocol. Therefore alternative approaches to monitor the changes in the amount of bound antigen were sought, and the ratio between the relative weight values at 14 and 19 nm, the approximate sizes of the two populations in the weight distribution was found to be a good parameter (Figure 3.31 C), as it was able to numerically express the decreased Ag binding in the presence of plasma observed in the DCS experiments. It should be mentioned that the approximate sizes of the AuNP@Ab and AuNP@Ab@Ag populations were ca. 18.73 ± 0.36 and ca. 14.18 ± 0.36. The DCS size distribution for the increasing Ag concentrations in 2 % plasma are presented in Figure A.14 in the Appendix.

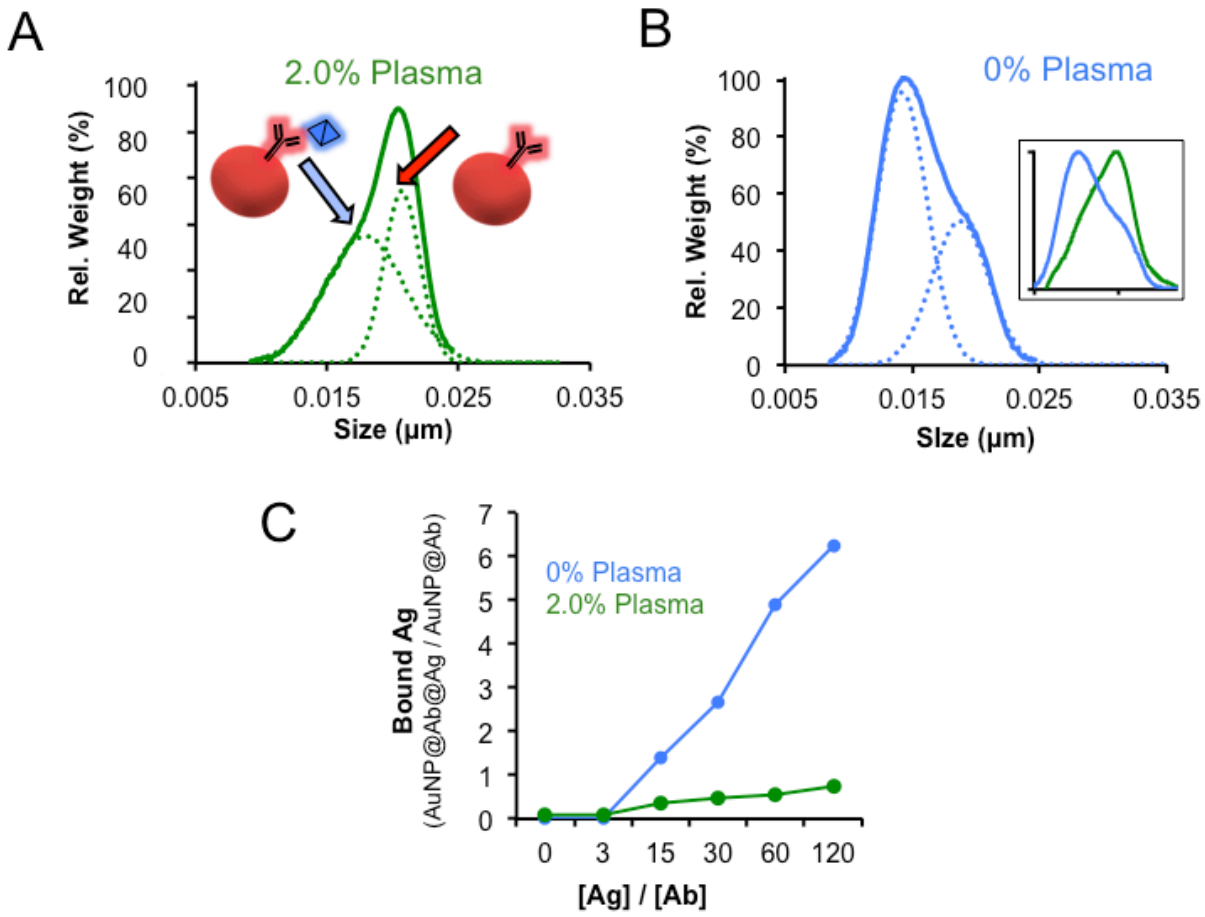

Figure 3.31 DCS results for the Ag binding to AuNP@Ab in 2% plasma. Experimental DCS size distributions (continuous lines) of AuNP@Ab@Ag and corresponding Gaussian fits (dashed lines) in the presence (A) and absence (B) of plasma. Inset in (B): overlap of the experimental size distributions in the presence (green line) and absence of plasma (blue). (C) Ratio between the relative weight values at 14 and 19 nm, the approximate sizes of the two populations, AuNP@Ab@Ag and AuNP@Ab. [Ag]/[Ab]=30, [AuNP]=0.056nM and [Ab]/[AuNP]=200.

21.5.3. Proving the Ag to AuNP@Ab binding specificity in plasma

We have shown that when both AuNP@Ab and AuNP are incubated with plasma, the thickness and density of the plasma protein corona is the same. This is not surprising considering that the protein concentration in plasma is around 60-85 $mg.mL^{-1}$, with more than 3000 different proteins[149]. Remarkably, despite the complex corona of plasma proteins, the Ab are still on the AuNP surface and are still active, this can be seen by the differences in the DCS relative weight size distribution of the AuNP and AuNP@Ab when Ag is added to the mixture (dashed black and red lines

respectively in Figure 3.32), the AuNP@Ab show a shift in the size distribution from a monomodal towards a bimodal distribution, while the size distribution of AuNP remains unchanged.

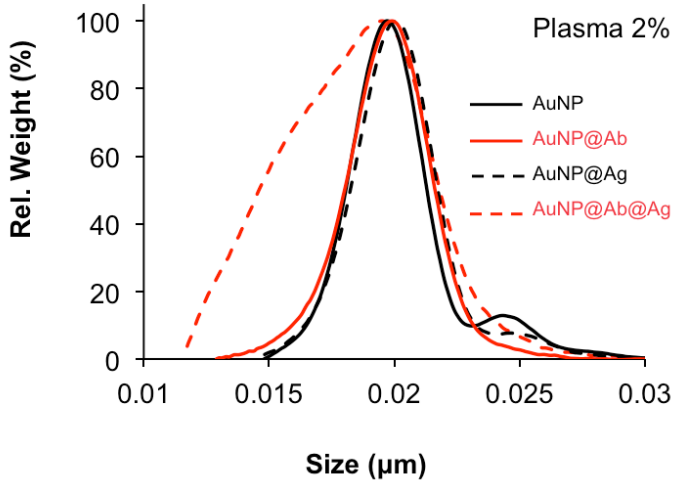

Figure 3.32 DCS assessment of the Ag binding specificity in plasma. DCS relative weight size distributions of AuNP (black lines) and AuNP@Ab (red lines) incubated in 2 % (V/V) plasma, in the presence (dashed lines) and absence of Ag (continuous lines). [Ag]/[Ab]=30, [AuNP]=0.056nM and [Ab]/[AuNP]=200.

21.5.4. Inhibition of the Ag to AuNP@Ab binding by plasma

AuNP@Ab were incubated with Ag (at a molar ratio of 30 to 1) and increasing plasma concentrations from 0.1 to 3.0 % (V/V). DCS size distributions showed the expected behavior, a decrease in the amount of Ag bound at increasing plasma concentrations, as can be perceived by a decrease in the AuNP@Ab@Ag population fitted area, depicted in Figure 3.33. The corresponding DCS relative weight size distributions are presented in Figure A.15, Appendix.

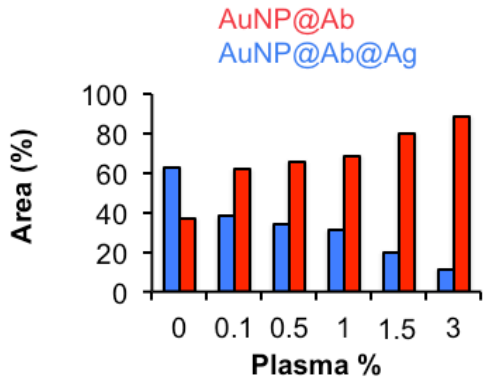

Figure 3.33 DCS assessment of the Ag binding inhibition by increasing plasma concentrations. The relative areas of the Gaussian distribution fits to AuNP@Ab and AuNP@Ab@Ag are depicted. Plasma concentrations: 0.1, 0.5, 1.0, 1.5 and 3.0 %, corresponding to natural occurring Trf concentrations of 4.0, 20, 40, 60 and 120 µg mL^{-1}. [Ag]/[Ab]=30, [AuNP]=0.056nM and [Ab]/[AuNP]=200.

21.5.5. Fluorescence detection of Ag binding in plasma

In the experiments for specificity evaluation using Trf, the background signal of AuNP@Ab in the presence of Trf only was clearly much lower then the analytical signal of the experiments with Ag only (for the larger concentrations tested, Figure 3.27). In the case of plasma, the background plasma signal is now higher then the Ag only signal in most of the concentrations tested (Figure 3.34, green line). As for the results in which both plasma and Ag are present in the reaction mixture (Figure 3.34, red line), the fluorescence signal was not decreased (as it did when both Trf and Ag were measured (Figure 3.27)), and it is higher than the Ag only signal throughout the concentration range tested (Figure 3.34, red and blue lines, respectively).

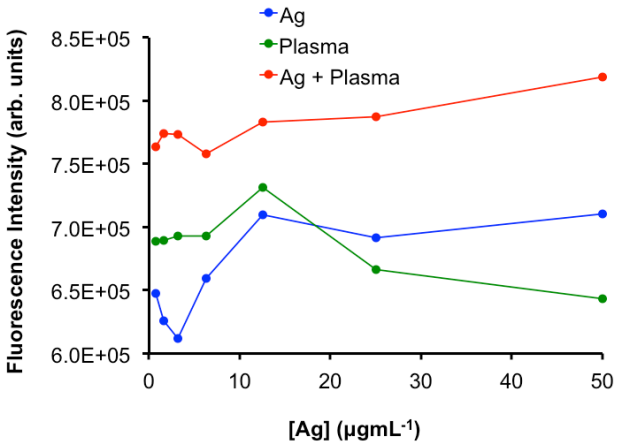

Figure 3.34 Fluorescence assessment of the Ag binding specificity and inhibition in the presence of 2% plasma. Experiments were performed with the Ag only (blue), with plasma only (green), whose naturally occurring Trf concentration was equal to the Ag concentration, and with both Ag and plasma (red) being the naturally occurring Trf concentration in plasma equal to the Ag concentration in each data point. Average results from three measurements are plotted. Lines were inserted to guide the eye. The Ag to Ab ratios used, 765 to 12.0, correspond to final antigen (and also of Trf in the plasma) concentrations from 50 to 0.78 $\mu g.mL^{-1}$ and [Ag] / $[CyAg]_0$ ratios of 2.86 to 0.0446. Plasma final concentration varied from 1.4 to 0.02 % (V/V). [AuNP]=0.0047 nM, [Ab]/[AuNP]=200.

21.5.6. Comparison of the Ag binding inhibition and the non-specific background signals of Trf and plasma

The data collected so far for DCS, allows a quantitative comparison between the extent of Ag binding inhibition in the presence of Trf and plasma. In Figure 3.35 is presented the Ag binding inhibition of Trf and plasma at Trf to Ag concentrations ratios of 1 and 2. For the sake of clarity, in the conditions presented in Figure 3.35 plasma is diluted in order for the naturally occurring Trf concentration to be equal ([Trf]/[Ag]=1), or twice ([Trf]/[Ag]=2) the amount of Ag. Note that the

natural occurring Trf concentration in plasma was obtained from the literature[149]. The data shows a small increase in the Ag binding inhibition with increasing [Trf]/[Ag] ratios for both purified and naturally occurring Trf (in plasma). Comparing Trf and plasma, plasma induces a higher Ag binding inhibition (independently of the Trf ratio) then Trf alone. This indicates that other plasma components can also inhibit the Ag binding.

The fluorescence signal of the Ag in the presence of plasma was always significantly above the Ag only signal, therefore no binding inhibition could be calculated (Table 3.3), although it might be present, as indicated by DCS experiments, the large background signal might be masking this effect.

As for the background signal, DCS results of AuNP@Ab incubated with plasma indicate that non-specific protein binding has occurred extensively (Figure 3.30) while incubation with Trf did not show Trf binding (Figure 3.25 C). This indicates that the non-specific analytical signal from plasma -background signal- was larger then the Trf background signal, in DCS experiments.

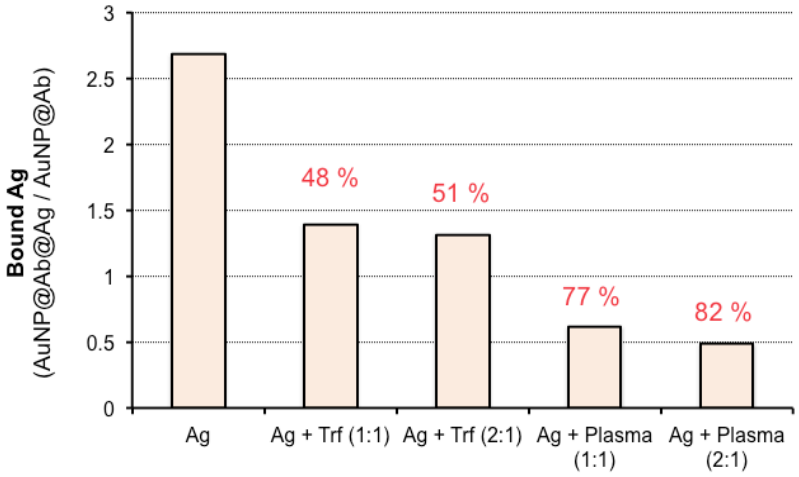

Figure 3.35 Ag to AuNP@Ab binding inhibition by Trf and plasma as assessed by DCS. The changes in the amount of bound antigen are monitored by the AuNP@Ab@Ag to AuNP@Ab ratio. Trf was added to AuNP@Ab@Ag at Trf to Ag concentration ratios of 1 and 2. Plasma was added to AuNP@Ab@Ag at final concentrations (V/V) of 1 and 2 %, corresponding to natural occurring Trf concentration in plasma of 40 and 80 µgmL-1, and Trf to Ag ratios of 1 and 2, respectively. The AuNP@Ab@Ag to AuNP@Ab ratio, for simplicity "Bound Ag" ratio, was used to estimate the binding inhibition: Inhibition (%) = [Bound Ag – Bound Ag (Trf or plasma)]/ Bound Ag x 100. [Ag]/[Ab]=30, [AuNP]=0.056nM and [Ab]/[AuNP]=200.

The Ag only fluorescence signal was significantly above the non-specific Trf only signal (Figure 3.27) starting at the Ag concentration of 13 $\mu g.mL^{-1}$ -the LoSD- (Tables 3.1 and 3.3), while for plasma this value increased to 25 $\mu g.mL^{-1}$ (Table 3.3). This result is an indication that the non-specific analytical signal from plasma -background signal- was larger then the Trf background signal. The fluorescence LoIB for plasma was 0.75 $\mu g.mL^{-1}$, meaning that all the plasma concentrations tested produced a background signal significantly above the blank (Figure 3.34 and Table 3.3), while for Trf, the LoIB could not be assigned, as Trf concentrations which produced a F.I. significantly above the blank were found in a random way (Figure 3.27, green line and Tables 3.1 and 3.3).

Table 3.3 Analytical performance parameters for the Trf and plasma competitive experiments using fluorescence detection

	[Trf] / (μg.mL^{-1})	[plasma Trf] / (μg.mL^{-1})
LoSD	13	25
LoIB	NA*	0.75
LoINH	6.3	NA[#]

*LoIB varied between days, values higher and lower than the background signal were found in a random, non concentration dependent disposition, [#] No binding inhibition could be detected, FI was always larger when Ag was measured in plasma than when it was measured alone.

21.6 Theoretical model of the antigen to antibody binding at the AuNP@Ab surface

During the development of the assay we expected that the CyAg fluorescence would be quenched in the presence of the AuNP@Ab, as the antibodies would retain the fluorophore near the AuNP's surface, an approach shown to be successful for other antibody-antigen pairs, in both competitive and sandwich formats (see Figure 1.3. Introduction, section 3.1.3.1). However, the F.I. of the blank measurement was actually higher than that of a solution containing the same amount of CyAg but no AuNP@Ab. This indicates that under the conditions tested, fluorescence enhancement occurs. To better understand the underlying mechanism of the proposed assay we compared the experimental data with a theoretical model based on a competitive equilibrium between the labeled (CyAg) and unlabeled antigen (Ag) for the antibody binding sites at the AuNP@Ab conjugates surface. Considering the equilibrium between the 3 components of the assay:

$$\mathrm{CyAg-BNC + Ag \Leftrightarrow Ag-BNC + CyAg} \qquad \text{Eq.43}$$

where "Ag" is the target analyte, "BNC" is the AuNP to antibody bionanoconjugate (written in this way for simplicity, instead of AuNP@Ab), CyAg-BNC stands for the labeled form of the Ag bound to the AuNP@Ab conjugates, Ag-BNC represents the bionanoconjugate bound form of the analyte, and "CyAg" stands for the labeled form of the Ag. This equilibrium constant can be expressed as:

$$K = \frac{[\mathrm{Ag-BNC}] \times [\mathrm{CyAg}]}{[\mathrm{CyAg-BNC}] \times [\mathrm{Ag}]} = 1 \qquad \text{Eq.44}$$

with K=1, based upon the assumption that the binding constants of the labeled and unlabeled forms of the Ag for the Ab at the surface of the conjugates are equal.

Considering that the initial concentration of the labeled antigen ($[CyAg]_o$) will be equal to the sum of the concentrations of its bionanoconjugate bound and free forms at equilibrium, and that the same is true for the unlabeled antigen we have,

$$\left[CyAg\right]_o = \left[CyAg - BNC\right] + \left[CyAg\right] \qquad \text{Eq.45}$$

and

$$\left[Ag\right]_o = \left[Ag - BNC\right] + \left[Ag\right] \qquad \text{Eq.46}$$

Assuming that the amount of labeled antigen not bound to the conjugates will be equal to the amount of bound unlabeled antigen, as the later is responsible for displacing the previous from the binding sites on the antibody,

$$\left[CyAg\right] = \left[Ag - BNC\right] \qquad \text{Eq.47}$$

the equilibrium equation (Eq.42) can be reformulated as:

$$K = \frac{\left[CyAg\right]^2}{\left(\left[CyAg\right]_o - \left[CyAg\right]\right) \times \left(\left[Ag\right]_o - \left[CyAg\right]\right)} = 1 \qquad \text{Eq.48}$$

Defining the ratio R as the coefficient between the concentration of unlabeled Ag added to the system and the initial CyAg concentration (Eq.47), the previous equation can be rearranged in order to obtain an expression of the fluorescence response as function of the total (constant) concentration of CyAg added to the system,

$$R = \frac{\left[Ag\right]_o}{\left[CyAg\right]_o} \qquad \text{Eq.49}$$

$$\frac{[CyAg]}{[CyAg]_o} = \frac{R}{R+1} \qquad \text{Eq.50}$$

R is calculated according to the experimentally known $[Ag]_o$ and $[CyAg]_o$ values, as the absorbance of the labeled Ag used in the assay is very low, A<<0.05, the fluorescence intensity is directly proportional, in a good approximation, to the label concentration, and it can be used to determine the experimental molar ratio $[CyAg] / [CyAg]_o$.

The rearrangement of the equilibrium constant equation (Eq. 43), was performed in order to provide a valid way of relating the fluorescence signal to the concentration of the Ag added in each experimental point. Knowing the concentration of Ag added at each point, the total concentration of CyAg and the concentration of Ab we can calculate the expected fluorescence response, as the ratio between the unbound CyAg concentration and total CyAg concentration. The unbound CyAg is the only species responsible for the measured fluorescence, as the bound fraction should have its fluorescence quenched. The theoretical value for $[CyAg] / [CyAg]_o$ can then be compared with the experimental value, obtained by dividing the fluorescence intensity of the sample in the presence of the Ag and the fluorescence intensity of a sample containing only the CyAg without AuNP@Ab or Ag. With these initial conditions the experimental and theoretical curves do not overlap (open circles in Figure 3.36).

The theoretical description had to be modified to take into account two major experimental observations:

i) there is always an excess of unbound CyAg. This is because the molar ratio of CyAg to Ab is ca. 268, if this information is not considered in the model, the theoretical curve would be always below the experimental curve, as the theoretical curve assumes that when there is no Ag added to the system, there is no free Cy3B. By adding to Eq.50 a factor that takes into account the fact that [CyAg]>>[Ab], we will now have Eq.51, and the theoretical curve (filled black circles) is now closer to the experimental curve (open red circles);

$$\frac{[CyAg]}{[CyAg]_o} = \frac{R}{R+1} + \frac{[CyAg]_o - [Ab]}{[CyAg]_o} \qquad \text{Eq.51}$$

ii) there is always some degree of fluorescence enhancement. The F.I. of the CyAg is higher in the presence of the AuNP@Ab than in its absence, there is no quenching. As previously stated, when calculating the experimental ratio $[CyAg]/[CyAg]_o$, [CyAg] is measured by the F.I. of the sample with a given Ag concentration, while $[CyAg]_o$ is measured by the F.I. of the CyAg. Therefore the [CyAg] takes into account the fluorescence enhancement because it is measured in the presence of the

AuNP@Ab, while the $[CyAg]_o$ does not takes into account this fluorescence enhancement. That is why the experimental (open red circles) curve is higher in the $[CyAg]/[CyAg]_o$ scale, than the theoretical curve (black filled circles). If this fluorescence enhancement is considered in the estimation of the initial CyAg concentration, $[CyAg]_o$, that is, if the F.I. of CyAg in the presence of AuNP@Ab is used for estimating $[CyAg]_o$ instead of the CyAg in the absence of the AuNP@Ab, the experimental (red filled circles) and theoretical (black filled circles) curves are now in good agreement (Figure 3.36 A and B).

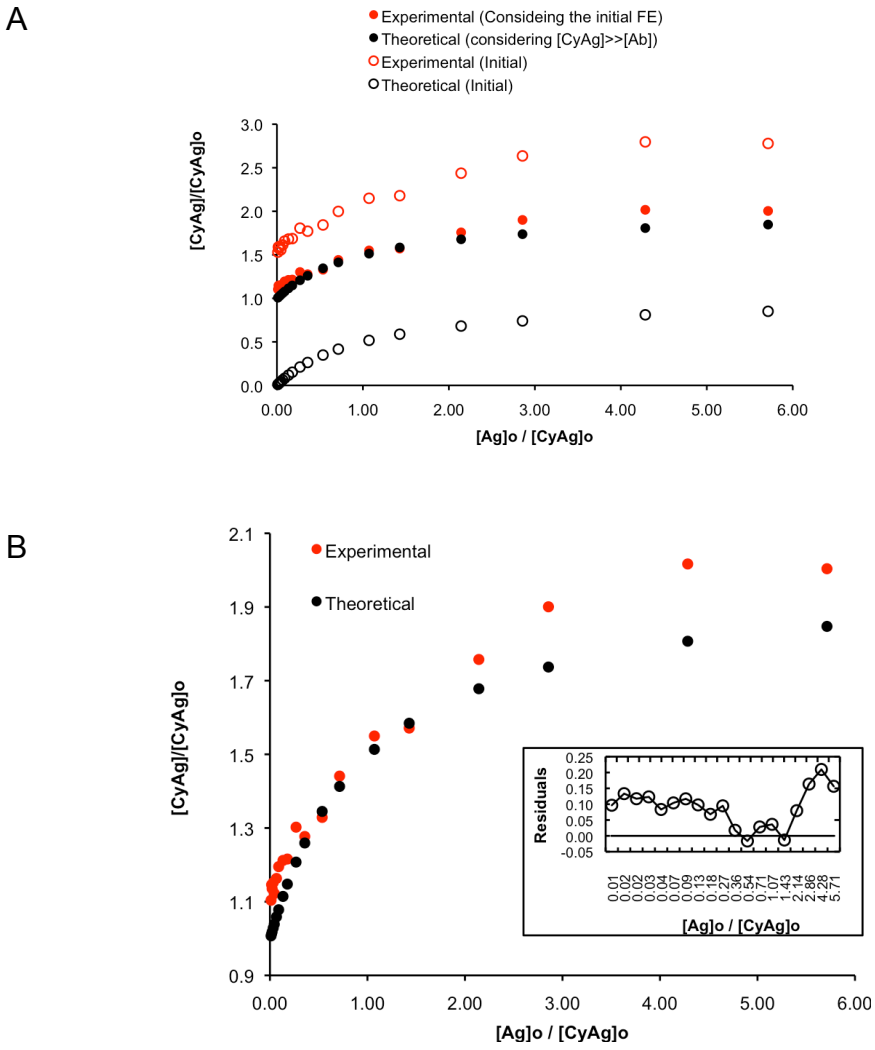

Figure 3.36 Fluorescence assay response assessed by the theoretical model. (A) The experimental (red circles) and theoretical (black circles) results are plotted. From the initial model (open circles) an improvement in the fit of the theoretical results to the experimental results could be obtained by taking into account the fact that the initial CyAg concentration was 268 times higher than that of the antibodies (filled red circles) and taking into account in the experimental results the fact that there is always an enhancement, as the fluorescence of Cy3B is increased when AuNP@Ab are added (filled black circles). (B) The final experimental and theoretical values considered, with the inset showing the residuals. These represent the difference between the experimental and theoretical $[CyAg]/[CyAg]_o$ ratios. The increase in the detected CyAg concentration ([CyAg]) is represented as a function of the increase in the added Ag concentrations ($[Ag]_o$). Both concentrations are normalized to the total CyAg concentration ($[CyAg]_o$). The Ag to Ab ratios used, 1500 to 3, correspond to final antigen concentrations from 100 to 0.195 μg mL^{-1} and $[Ag] / [CyAg]_o$ ratios of 5.71 to 0.0112.

The residuals plot (Figure 3.36 B, inset), expressing the difference between the theoretical and experimental values of $[CyAg]/[CyAg]_o$, showed a pattern of experimental deviation from the theoretically expected values, as random distribution of the deviations around zero would indicate an appropriate fit of the theoretical results. This deviation indicates that there is a underestimation of the measured fluorescence intensity by the model or that the experimental fluorescence intensity is increasingly enhanced as more Ag is bound, the rationale for this being that more bound Ag, would mean more unbound CyAg, that by being at a larger distance from the particle would be subject to an overall more enhanced interaction by the particles rather then an overall more quenched interaction. This interpretation is given because, as stated in the introduction, the distance of the possible fluorophore-metal surface interactions probably increases in order, with quenching interactions followed by enhancing interactions.

Chapter IV

Conclusions

22. Conclusions

All the proposed goals were achieved. In the applied research part, the immunoassay for malaria diagnosis was successfully established using: fluorescence detection for different-sized AuNP of 15 and 30 nm diameter, and also using AGE detection with 30 nm AuNP. As for the basic research part, the AuNP@Ab bionanoconjugates where shown to exhibit a specific response to the target Ag, with little –as assessed by AGE and fluorescence- or none –as assessed by DCS- non-specific binding detected when purified transferrin (Trf) is used; non-specific binding of plasma proteins was detected by Fluorescence and DCS; Ag binding (AuNP@Ab activity) was detected both in non-competitive or in competitive conditions both with plasma –as assessed by DCS and Fluorescence- and with Trf, detected by all three techniques; and finally, Trf inhibited the Ag binding, but not completely -as assessed by the three techniques- while plasma inhibited the Ag binding as assessed by DCS but the same conclusion could not be made for fluorescence due to the large background signal caused by plasma non-specific binding.

In addition, it was proved that stable homemade-AuNP to antibody conjugates are capable of detecting the native and recombinant forms of their target Ag (*Pf*Hsp70) where produced. The electrostatic conjugation approach was shown to produce more active conjugates than the crosslinking approach. The electrostatic conjugates were successfully applied in a proof-of-concept fluorescence immunoassay using the recombinant Ag and were also capable of detecting the native Ag in a *P. falciparum* infected RBC culture, with the potential of detecting parasitemia levels as low as 0.27%.

As for the molecular level Ag to commercial-AuNP@Ab binding characterization by AGE, fluorescence and DCS, all three techniques were capable of indicating that the AuNP@Ab conjugates are active. It is of fundamental and practical interest to have such characterization techniques, as the applicability of any immunoassays being developed with antibody to nanoparticle bionanoconjugates will depend on the a retained activity of the antibodies at the nanoparticle surface.

Fluorescence was the most sensitive on a *per* mass basis (as assessed by the LoD). The ability to discriminate a specific binding (as assessed by the LoSD), i.e. the lowest concentration at which the binding can be significantly considered to be above the level of non-specific binding (LoIB) was also higher for fluorescence, with DCS not being able to indicate the non-specific binding of Trf detected at a significant level by fluorescence and AGE.

These two last techniques indicated a sensitive response of the AuNP@Ab conjugates to the Ag, with a concentration dependence on the analytical signal, while the non-specific response to Trf –the Trf background signal- was much lower then the specific signal obtained with the target Ag, at a certain concentration range defined by the LoSD.

Fluorescence and AGE, for being readily available techniques are promising approaches for a pre-characterization of the activity and specificity of the nanoparticle to antibody conjugates meant for

immunoassay and other areas were these conjugates are applied, this simple approach will save time in the cases where the conjugates do not work in their intended application because the activity is completely lost, or lost to a degree where it can no longer be used for significantly assigning the analytical response to the detection of the target antigen. The good cross-correlation regarding activity (as assessed by LoD) and detection of Ag binding inhibition by Trf (assessed by LoINH) between fluorescence, AGE and DCS, with this last two techniques actually allowing us to "see" the binding and inhibition is a strong support to the reliability of the experimental findings.

Chapter V

Bibliography

23. Bibliography

1. Woo J-R, Lim D-K, Nam J-M (2011) Minimally Stable Nanoparticle-Based Colorimetric Assay for Simple, Rapid, and Sensitive Antibody Structure and Activity Evaluation. Small 7: 648-655.
2. Shonhai A (2010) Plasmodial heat shock proteins: targets for chemotherapy. Fems Immunology and Medical Microbiology 58: 61-74.
3. CDC (2011) Centers for Disease Control and Prevention; Malaria: http://www.cdc.gov/malaria/index.html (Acessed January 2011).
4. Shonhai A, Boshoff A, Blatch GL (2007) The structural and functional diversity of Hsp70 proteins from Plasmodium falciparum. Protein Science 16: 1803-1818.
5. WHO (2010) World Health Organization; World Malaria Report 2010. http://rbm.who.int/partnership/board/meetings/ppt/19pbm/19pbmWMR2010.pdf (Acessed July 2011).
6. Prudencio M, Rodriguez A, Mota MM (2006) The silent path to thousands of merozoites: the Plasmodium liver stage. Nature Reviews Microbiology 4: 849-856.
7. Prudencio M, Rodrigues CD, Hannus M, Martin C, Real E, et al. (2008) Kinome-Wide RNAi Screen Implicates at Least 5 Host Hepatocyte Kinases in Plasmodium Sporozoite Infection. Plos Pathogens 4.
8. Sturm A, Amino R, van de Sand C, Regen T, Retzlaff S, et al. (2006) Manipulation of host hepatocytes by the malaria parasite for delivery into liver sinusoids. Science 313: 1287-1290.
9. Bell D, Wongsrichanalai C, Barnwell JW (2006) Ensuring quality and access for malaria diagnosis: how can it be achieved? Nature reviews Microbiology 4: S7-20.
10. RDTinfo (2011) Current Information on Rapid Diagnostic Tests, PATH, USAID. http://www.rapid-diagnostics.org/index.htm.
11. Polpanich D, Tangboriboonrat P, Elaissari A, Udomsangpetch R (2007) Detection of malaria infection via latex agglutination assay. Analytical Chemistry 79: 4690-4695.
12. WHO (2009) World Health Organization, Rsults of WHO Malaria RDT Product Testing Round 2. http://www.wpro.who.int/internet/files/rdt/RDTMalariaRd2_FINAL.pdf (Acessed January 2011).
13. Murray CK, Gasser RA, Jr., Magill AJ, Miller RS (2008) Update on rapid diagnostic testing for malaria. Clinical Microbiology Reviews 21: 97-+.
14. Lee N, Baker J, Andrews KT, Gatton ML, Bell D, et al. (2006) Effect of sequence variation in Plasmodium falciparum Histidine-Rich protein 2 on binding of specific monoclonal antibodies: Implications for rapid diagnostic tests for malaria. Journal of Clinical Microbiology 44: 2773-2778.
15. Banumathy G, Singh V, Tatu U (2002) Host chaperones are recruited in membrane-bound complexes by Plasmodium falciparum. Journal of Biological Chemistry 277: 3902-3912.
16. Arruebo M, Valladares M, Gonzalez-Fernandez A (2009) Antibody-Conjugated Nanoparticles for Biomedical Applications. Journal of Nanomaterials.
17. Molina-Bolivar JA, Galisteo-Gonzalez F (2005) Latex immunoagglutination assays. Journal of Macromolecular Science-Polymer Reviews C45: 59-98.
18. Norde W (1986) ADSORPTION OF PROTEINS FROM SOLUTION AT THE SOLID-LIQUID INTERFACE. Advances in Colloid and Interface Science 25: 267-340.
19. Norde W (1995) ADSORPTION OF PROTEINS AT SOLID-LIQUID INTERFACES. Cells and Materials 5: 97-112.
20. Norde W, Giacomelli CE (2000) BSA structural changes during homomolecular exchange between the adsorbed and the dissolved states. Journal of Biotechnology 79: 259-268.
21. Klein J (2007) Probing the interactions of proteins and nanoparticles. Proceedings of the National Academy of Sciences of the United States of America 104: 2029-2030.

22. Dutta D, Sundaram SK, Teeguarden JG, Riley BJ, Fifield LS, et al. (2007) Adsorbed proteins influence the biological activity and molecular targeting of nanomaterials. Toxicological Sciences 100: 303-315.
23. Lynch I, Dawson KA (2008) Protein-nanoparticle interactions. Nano Today 3: 40-47.
24. Cavadas M, González-Fernández A, Franco R (2011) Pathogen-mimetic stealth nanocarriers for drug delivery: a future possibility. Nanomedicine: Nanotechnology, Biology, and Medicine In Press.
25. Cedervall T, Lynch I, Foy M, Berggad T, Donnelly SC, et al. (2007) Detailed identification of plasma proteins adsorbed on copolymer nanoparticles. Angewandte Chemie-International Edition 46: 5754-5756.
26. Cedervall T, Lynch I, Lindman S, Berggard T, Thulin E, et al. (2007) Understanding the nanoparticle-protein corona using methods to quantify exchange rates and affinities of proteins for nanoparticles. Proceedings of the National Academy of Sciences of the United States of America 104: 2050-2055.
27. Walczyk D, Bombelli FB, Monopoli MP, Lynch I, Dawson KA (2010) What the Cell "Sees" in Bionanoscience. Journal of the American Chemical Society 132: 5761-5768.
28. Rana S, Yeh Y-C, Rotello VM (2010) Engineering the nanoparticle-protein interface: applications and possibilities. Current Opinion in Chemical Biology 14: 828-834.
29. Aggarwal P, Hall JB, McLeland CB, Dobrovolskaia MA, McNeil SE (2009) Nanoparticle interaction with plasma proteins as it relates to particle biodistribution, biocompatibility and therapeutic efficacy. Advanced Drug Delivery Reviews 61: 428-437.
30. Vonarbourg A, Passirani C, Saulnier P, Simard P, Leroux JC, et al. (2006) Evaluation of pegylated lipid nanocapsules versus complement system activation and macrophage uptake. Journal of Biomedical Materials Research Part A 78A: 620-628.
31. Dobrovolskaia MA, Aggarwal P, Hall JB, McNeil SE (2008) Preclinical studies to understand nanoparticle interaction with the immune system and its potential effects on nanoparticle biodistribution. Molecular Pharmaceutics 5: 487-495.
32. Calzolai L, Franchini F, Gilliland D, Rossi F (2010) Protein-Nanoparticle Interaction: Identification of the Ubiquitin-Gold Nanoparticle Interaction Site. Nano Letters 10: 3101-3105.
33. Lundqvist M, Sethson I, Jonsson BH (2005) Transient interaction with nanoparticles "freezes" a protein in an ensemble of metastable near-native conformations. Biochemistry 44: 10093-10099.
34. Gole A, Dash C, Ramakrishnan V, Sainkar SR, Mandale AB, et al. (2001) Pepsin-gold colloid conjugates: Preparation, characterization, and enzymatic activity. Langmuir 17: 1674-1679.
35. Gomes I, Santos NC, Oliveira LMA, Quintas A, Eaton P, et al. (2008) Probing Surface Properties of Cytochrome c at Au Bionanoconjugates. Journal of Physical Chemistry C 112: 16340-16347.
36. Gagner JE, Lopez MD, Dordick JS, Siegel RW (2011) Effect of gold nanoparticle morphology on adsorbed protein structure and function. Biomaterials 32: 7241-7252.
37. Pathak S, Davidson MC, Silva GA (2007) Characterization of the functional binding properties of antibody conjugated quantum dots. Nano Letters 7: 1839-1845.
38. Rapoza RJ, Horbett TA (1990) THE EFFECTS OF CONCENTRATION AND ADSORPTION TIME ON THE ELUTABILITY OF ADSORBED PROTEINS IN SURFACTANT SOLUTIONS OF VARYING STRUCTURES AND CONCENTRATIONS. Journal of Colloid and Interface Science 136: 480-493.
39. Janeway Jr. C, Travers P, Walport M, Shlomchik M (2001) *Immunobiology. the immune system in health and disease*. 5th ed. New York: Garland Publishing. pp. 59-82.
40. Abbas A, Lichtman A, Pillai S (2007) *Cellular and Molecular Immunology*. 6th ed. Philadelphia: W. B. Saunders Company. pp. 29341-29342.
41. Goldsby R, Kindt T, Kuby J, Osborne B (2003) *Immunology*. 5th ed. New York: W. H. Freeman. pp. 299-318.
42. Murphy CJ, Gole AM, Hunyadi SE, Stone JW, Sisco PN, et al. (2008) Chemical sensing and imaging with metallic nanorods. Chemical Communications: 544-557.

43. Ghosh P, Han G, De M, Kim CK, Rotello VM (2008) Gold nanoparticles in delivery applications. Advanced Drug Delivery Reviews 60: 1307-1315.
44. Black DS, Bliska JB (2000) The RhoGAP activity of the Yersinia pseudotuberculosis cytotoxin YopE is required for antiphagocytic function and virulence. Molecular Microbiology 37: 515-527.
45. Baptista P, Pereira E, Eaton P, Doria G, Miranda A, et al. (2008) Gold nanoparticles for the development of clinical diagnosis methods. Analytical and Bioanalytical Chemistry 391: 943-950.
46. Dequaire M, Degrand C, Limoges B (2000) An electrochemical metalloimmunoassay based on a colloidal gold label. Analytical Chemistry 72: 5521-5528.
47. Leng C, Lai G, Yan F, Ju H (2010) Gold nanoparticle as an electrochemical label for inherently crosstalk-free multiplexed immunoassay on a disposable chip. Analytica Chimica Acta 666: 97-101.
48. Mao X, Baloda M, Gurung AS, Lin Y, Liu G (2008) Multiplex electrochemical immunoassay using gold nanoparticle probes and immunochromatographic strips. Electrochemistry Communications 10: 1636-1640.
49. Lai L-J, Yang Y-W, Lin Y-K, Huang L-L, Hsieh Y-H (2009) Surface characterization of immunosensor conjugated with gold nanoparticles based on cyclic voltammetry and X-ray photoelectron spectroscopy. Colloids and Surfaces B-Biointerfaces 68: 130-135.
50. Das J, Aziz MA, Yang H (2006) A nanocatalyst-based assay for proteins: DNA-free ultrasensitive electrochemical detection using catalytic reduction of p-nitrophenol by gold-nanoparticle labels. Journal of the American Chemical Society 128: 16022-16023.
51. Wang Z, Hu J, Jin Y, Yao X, Li J (2006) In situ amplified chemiluminescent detection of DNA and immunoassay of IgG using special-shaped gold nanoparticles as label. Clinical Chemistry 52: 1958-1961.
52. Fan A, Cao Z, Li H, Kai M, Lu J (2009) Chemiluminescence Platforms in Immunoassay and DNA Analyses. Analytical Sciences 25: 587-597.
53. Fan AP, Lau CW, Lu JZ (2005) Magnetic bead-based chemiluminescent metal immunoassay with a colloidal gold label. Analytical Chemistry 77: 3238-3242.
54. Hu D, Han H, Zhou R, Dong F, Bei W, et al. (2008) Gold(III) enhanced chemiluminescence immunoassay for detection of antibody against ApxIV of Actinobacillus pleuropneumoniae. Analyst 133: 768-773.
55. Li ZP, Wang YC, Liu CH, Li YK (2005) Development of chemiluminescence detection of gold nanoparticles in biological conjugates for immunoassay. Analytica Chimica Acta 551: 85-91.
56. Duan C-F, Yu Y-Q, Cui H (2008) Gold nanoparticle-based immunoassay by using non-stripping chemiluminescence detection. Analyst 133: 1250-1255.
57. Ambrosi A, Airo F, Merkoci A (2010) Enhanced Gold Nanoparticle Based ELISA for a Breast Cancer Biomarker. Analytical Chemistry 82: 1151-1156.
58. Zhang S-B, Wu Z-S, Guo M-M, Shen G-L, Yu R-Q (2007) A novel immunoassay strategy based on combination of chitosan and a gold nanoparticle label. Talanta 71: 1530-1535.
59. Song C, Wang Z, Yang J, Zhang R, Cui Y (2010) Preparation of 2-mercaptobenzothiazole-labeled immuno-Au aggregates for SERS-based immunoassay. Colloids and Surfaces B-Biointerfaces 81: 285-288.
60. Cai H-H, Yang P-H, Feng J, Cai J (2009) Immunoassay detection using functionalized gold nanoparticle probes coupled with resonance Rayleigh scattering. Sensors and Actuators B-Chemical 135: 603-609.
61. Huang H, Tang C, Zeng Y, Yu X, Liao B, et al. (2009) Label-free optical biosensor based on localized surface plasmon resonance of immobilized gold nanorods. Colloids and Surfaces B-Biointerfaces 71: 96-101.
62. Lee S, Mayer KM, Hafner JH (2009) Improved Localized Surface Plasmon Resonance Immunoassay with Gold Bipyramid Substrates. Analytical Chemistry 81: 4450-4455.
63. Mayer KM, Hao F, Lee S, Nordlander P, Hafner JH (2010) A single molecule immunoassay by localized surface plasmon resonance. Nanotechnology 21.

64. Peng Z, Chen Z, Jiang J, Zhang X, Shen G, et al. (2007) A novel immunoassay based on the dissociation of immunocomplex and fluorescence quenching by gold nanoparticles. Analytica Chimica Acta 583: 40-44.
65. Ao LM, Gao F, Pan BF, He R, Cui DX (2006) Fluoroimmunoassay for antigen based on fluorescence quenching signal of gold nanoparticles. Analytical Chemistry 78: 1104-1106.
66. Mayilo S, Ehlers B, Wunderlich M, Klar TA, Josel H-P, et al. (2009) Competitive homogeneous digoxigenin immunoassay based on fluorescence quenching by gold nanoparticles. Analytica Chimica Acta 646: 119-122.
67. Mayilo S, Kloster MA, Wunderlich M, Lutich A, Klar TA, et al. (2009) Long-Range Fluorescence Quenching by Gold Nanoparticles in a Sandwich Immunoassay for Cardiac Troponin T. Nano Letters 9: 4558-4563.
68. Kato N, Caruso F (2005) Homogeneous, competitive fluorescence quenching immunoassay based on gold nanoparticle/polyelectrolyte coated latex particles. Journal of Physical Chemistry B 109: 19604-19612.
69. Berne BJ, Pecora R, editors (1990) Dynamic Light Scattering with application to Chemistry, Biology and Physics. Melbourne, FL: Krieger Publishing Company.
70. Santos NC, Castanho M (1996) Teaching light scattering spectroscopy: The dimension and shape of tobacco mosaic virus. Biophysical Journal 71: 1641-1650.
71. Xiaohua Huang IHE-S, Mostafa A. El-Sayed, editor (2010) Fluorescent Quenching Gold nanoparticles: Potential Biomedical Applications. New Jersey, USA: John Wiley & Sons. 573-574 p.
72. Uwe Kreibig MV, editor (1995) Optical Properties of Metal Clusters. Berlin, DE: Springer Verlag. 116-117 p.
73. Yguerabide J, Yguerabide EE (1998) Light-scattering submicroscopic particles as highly fluorescent analogs and their use as tracer labels in clinical and biological applications - I. Theory. Analytical Biochemistry 262: 137-156.
74. Mie G (1908) Articles on the optical characteristics of turbid tubes, especially colloidal metal solutions. Annalen Der Physik 25: 377-445.
75. Malvern (2009) Zetasizer Nano User Manual, Mano317 Issue 5.0, August 2009, Worcestershire, UK. http://www.malvern.com/malvern/kbase.nsf/allbyno/KB002553/$file/Zetasizer Nano user manual (Man0317-5.0) inc addendum - (26-05-10).pdf.
76. Mulvaney P (1996) Surface plasmon spectroscopy of nanosized metal particles. Langmuir 12: 788-800.
77. Mayer KM, Hafner JH (2011) Localized Surface Plasmon Resonance Sensors. Chemical Reviews 111: 3828-3857.
78. Domingues MM, Santiago PS, Castanho MARB, Santos NC (2008) What can light scattering spectroscopy do for membrane-active peptide studies. Journal of Peptide Science 14: 394-400.
79. Lesniak A, Campbell A, Monopoli MP, Lynch I, Salvati A, et al. (2010) Serum heat inactivation affects protein corona composition and nanoparticle uptake. Biomaterials 31: 9511-9518.
80. Lakowicz JR (2005) Radiative decay engineering 5: metal-enhanced fluorescence and plasmon emission. Analytical Biochemistry 337: 171-194.
81. Ling J, Huang CZ (2010) Energy transfer with gold nanoparticles for analytical applications in the fields of biochemical and pharmaceutical sciences. Analytical Methods 2: 1439-1447.
82. Amanda J. Haes DAS, Richard P. Van Duyne, editor (2006) Nanoscale Optical Sensors Based on Surface Plasmon Resonance. Boca Raton, USA: CRC Press, Taylor & Francis Group, LCC.
83. Liz-Marzan LM (2006) Tailoring surface plasmons through the morphology and assembly of metal nanoparticles. Langmuir 22: 32-41.
84. Halas NJ, Lal S, Chang W-S, Link S, Nordlander P (2011) Plasmons in Strongly Coupled Metallic Nanostructures. Chemical Reviews 111: 3913-3961.
85. Morton SM, Silverstein DW, Jensen L (2011) Theoretical Studies of Plasmonics using Electronic Structure Methods. Chemical Reviews 111: 3962-3994.
86. Sardar R, Funston AM, Mulvaney P, Murray RW (2009) Gold Nanoparticles: Past, Present, and Future. Langmuir 25: 13840-13851.

87. Khlebtsov NG, Dykman LA (2010) Optical properties and biomedical applications of plasmonic nanoparticles. Journal of Quantitative Spectroscopy & Radiative Transfer 111: 1-35.
88. El-Sayed MA (2001) Some interesting properties of metals confined in time and nanometer space of different shapes. Accounts of Chemical Research 34: 257-264.
89. W.C. Tan KK, J. Singh, and S.O. Kasap,, editor (2006) Fundamental Optical Properties of Materials I. Wiltshire, UK: Jonh Wiley & Sons. 2-5 p.
90. Olympus (2011, 27th July) Olympus Microscopy Resource Center: Basic Concepts in Fluorescence, http://www.olympusmicro.com/primer/techniques/fluorescence/fluorescenceintro.html .
91. IUPAC, editor (1997) Compendium of Chemical Terminology (the "Gold Book"). Oxford: Blackwell Scientific Publications.
92. Lakowicz JR, editor (2006) Principles of Fluorescence Spectroscopy. 3rd Edition ed. New York, USA: Springer.
93. Stryer L (1978) FLUORESCENCE ENERGY-TRANSFER AS A SPECTROSCOPIC RULER. Annual Review of Biochemistry 47: 819-846.
94. Bhowmick S, Saini S, Shenoy VB, Bagchi B (2006) Resonance energy transfer from a fluorescent dye to a metal nanoparticle. Journal of Chemical Physics 125.
95. Li X, Qian J, Jiang L, He S (2009) Fluorescence quenching of quantum dots by gold nanorods and its application to DNA detection. Applied Physics Letters 94.
96. Kondon M, Kim J, Udawatte N, Lee D (2008) Origin of size-dependent energy transfer from photoexcited CdSe quantum dots to gold nanoparticles. Journal of Physical Chemistry C 112: 6695-6699.
97. Orange JS, Fassett MS, Koopman LA, Boyson JE, Strominger JL (2002) Viral evasion of natural killer cells. Nature Immunology 3: 1006-1012.
98. Persson BNJ, Lang ND (1982) ELECTRON-HOLE-PAIR QUENCHING OF EXCITED-STATES NEAR A METAL. Physical Review B 26: 5409-5415.
99. Yun CS, Javier A, Jennings T, Fisher M, Hira S, et al. (2005) Nanometal surface energy transfer in optical rulers, breaking the FRET barrier. Journal of the American Chemical Society 127: 3115-3119.
100. CPS (2004) CPS DIsc Centrifuge Operating Manual, Updated June 2004, CPS Instruments, Florida, USA. http://www.cpsinstruments.eu/pdf/Manual.pdf.
101. Vegad H (2007) 'Old' technique reborn for nanoparticle size analysis with unparalleled resolution. Powder Metallurgy 50: 291-293.
102. Ian Laidlaw MS, editor (2005) Introduction to Differential Sedimentation, in *Analytical Ultracentrifugation Techniques and Methods*. Norfolk, UK: Royal Society of Chemistry. 270-290 p.
103. Robert Novy DD, Keith Yaeger, Robert Mierendorf (2001) Overcoming the codon bias of *E. coli* for enhanced protein expression. inNovations 12: 1-3.
104. Sheehan D (2000) Physical Biochemistry: Principles and Applications, John Wiley & Sons, Chichester, pp.153-213.
105. Patra HK, GuhaSarkar D, Dasgupta AK (2009) Multimodal electrophoresis of gold nanoparticles: A real time approach. Analytica Chimica Acta 649: 128-134.
106. Lopez-Lorente AI, Simonet BM, Valcarcel M (2011) Electrophoretic methods for the analysis of nanoparticles. Trac-Trends in Analytical Chemistry 30: 58-71.
107. Hanauer M, Pierrat S, Zins I, Lotz A, Sonnichsen C (2007) Separation of nanoparticles by gel electrophoresis according to size-and shape. Nano Letters 7: 2881-2885.
108. Parak WJ, Pellegrino T, Micheel CM, Gerion D, Williams SC, et al. (2003) Conformation of oligonucleotides attached to gold nanocrystals probed by gel electrophoresis. Nano Letters 3: 33-36.
109. Ding B, Deng Z, Yan H, Cabrini S, Zuckermann RN, et al. (2010) Gold Nanoparticle Self-Similar Chain Structure Organized by DNA Origami. Journal of the American Chemical Society 132: 3248-+.

110. You CC, De M, Han G, Rotello VM (2005) Tunable inhibition and denaturation of alpha-chymotrypsin with amino acid-functionalized gold nanoparticles. Journal of the American Chemical Society 127: 12873-12881.
111. Novagen (2004) Novagen User protocol TB009 Rev. F 104, Competent cells, pp 1-23. http://www.med.unc.edu/csb/PEP/manuals/novagen_competent_cells2.pdf.
112. Matambo TS, Odunuga OO, Boshoff A, Blatch GL (2004) Overproduction, purification, and characterization of the Plasmodium falciparum heat shock protein 70. Protein Expression and Purification 33: 214-222.
113. Champion JA, Mitragotri S (2006) Role of target geometry in phagocytosis. Proceedings of the National Academy of Sciences of the United States of America 103: 4930-4934.
114. Baca AM, Hol WGJ (2000) Overcoming codon bias: A method for high-level overexpression of Plasmodium and other AT-rich parasite genes in Escherichia coli. International Journal for Parasitology 30: 113-118.
115. Hanahan D (1983) STUDIES ON TRANSFORMATION OF ESCHERICHIA-COLI WITH PLASMIDS. Journal of Molecular Biology 166: 557-580.
116. Bertani G (2004) Lysogeny at mid-twentieth century: P1, P2, and other experimental, systems. Journal of Bacteriology 186: 595-600.
117. Qiagen (2003) The QIAexpressiomist™ A handbook for high-level expression and purification of 6xHist-tagged proteins. http://kirschner.med.harvard.edu/files/protocols/QIAGEN_QIAexpressionist_EN.pdf (Acessed January 2011).
118. Amersham (2000) The Recombinant Protein Handbook, Protein Amplification and Simple Purification, Handbooks from Amersham Pharmacia Biotech 18-1142-75, pp 8. http://www.biochem.uiowa.edu/donelson/Database items/recombinant_protein_handbook.pdf (Acessed January 2011).
119. Tsuji M, Mattei D, Nussenzweig RS, Eichinger D, Zavala F (1994) DEMONSTRATION OF HEAT-SHOCK PROTEIN-70 IN THE SPOROZOITE STAGE OF MALARIA PARASITES. Parasitology Research 80: 16-21.
120. Electrics HG (2011) Protein G HP Spin Trap, Instructions 28-9067-72 AB, http://www.gelifesciences.co.jp/tech_support/manual/pdf/28906772.pdf.
121. Electrics HG (2011) Protein G Sepharose 4 Fast Flow, Instructions 71-7083-00 AI, http://www.gelifesciences.com/aptrix/upp00919.nsf/Content/C760CFB155F7312BC1257628001CFE03/$file/71708300AI.pdf.
122. Baptista P, Doria G, Henriques D, Pereira E, Franco R (2005) Colorimetric detection of eukaryotic gene expression with DNA-derivatized gold nanoparticles. Journal of Biotechnology 119: 111-117.
123. Kimling J, Maier M, Okenve B, Kotaidis V, Ballot H, et al. (2006) Turkevich method for gold nanoparticle synthesis revisited. Journal of Physical Chemistry B 110: 15700-15707.
124. Bonanni A, Pumera M, Miyahara Y (2011) Influence of gold nanoparticle size (2-50 nm) upon its electrochemical behavior: an electrochemical impedance spectroscopic and voltammetric study. Physical Chemistry Chemical Physics 13: 4980-4986.
125. Kim S, Sessa DJ, Lawton JW (2004) Characterization of zein modified with a mild cross-linking agent. Industrial Crops and Products 20: 291-300.
126. Pierce TS (2011) Thermo Scientific, Pierce protein Research products, "Chemistry of crosslinking", http://www.piercenet.com/browse.cfm?fldID=CE4D6C5C-5946-4814-9904-C46E01232683 - nhsester.
127. Haiss W, Thanh NTK, Aveyard J, Fernig DG (2007) Determination of size and concentration of gold nanoparticles from UV-Vis spectra. Analytical Chemistry 79: 4215-4221.
128. Ferard G (1994) QUANTITIES AND UNITS FOR ELECTROPHORESIS IN THE CLINICAL LABORATORY - (IUPAC RECOMMENDATIONS 1994) (REPRINTED). Pure and Applied Chemistry 66: 891-896.

129. Zanchet D, Micheel CM, Parak WJ, Gerion D, Williams SC, et al. (2002) Electrophoretic and structural studies of DNA-directed Au nanoparticle groupings. Journal of Physical Chemistry B 106: 11758-11763.
130. Park S, Hamad-Schifferli K (2008) Evaluation of hydrodynamic size and zeta-potential of surface-modified an nanoparticle-DNA conjugates via Ferguson analysis. Journal of Physical Chemistry C 112: 7611-7616.
131. Helathcare GE (2006) GE Healthcare, Amersham, Cy™3B mono-reactive dye, Reagents for the labelling of biological compounds with Cy™3B monofunctional dyes, Product Booklet, Buckinghamshire, UK, http://www.gelifesciences.com/aptrix/upp00919.nsf/Content/F297E3EA17D1154DC1257628001D0AAA/$file/PA63100PL_Rev_C_2006_web.pdf.
132. Cooper M, Ebner A, Briggs M, Burrows M, Gardner N, et al. (2004) Cy3B (TM): Improving the performance of cyanine dyes. Journal of Fluorescence 14: 145-150.
133. Sigma AF (2011) Sigma-Aldrich, BCA, Bicinchoninic Acid Protein Assay Kit, St. Louis, MO, USA. http://www.sigmaaldrich.com/etc/medialib/docs/Sigma/Bulletin/b9643bul.Par.0001.File.tmp/b9643bul.pdf.
134. Liu X, Atwater M, Wang J, Huo Q (2007) Extinction coefficient of gold nanoparticles with different sizes and different capping ligands. Colloids and Surfaces B-Biointerfaces 58: 3-7.
135. ICH TM (2005) IInternational Conference in Harmonisation of Pharmaceuticals for Human Usage; ICH Harmonised Tripartite Guideline; Validation of Analytical procedures:Text and Methodology Q2(R1); http://www.ich.org/fileadmin/Public_Web_Site/ICH_Products/Guidelines/Quality/Q2_R1/Step4/Q2_R1__Guideline.pdf.
136. Murray A, Lawrence GP (1993) HOW SHOULD THE REPEATABILITY OF CLINICAL MEASUREMENTS BE ANALYZED - AN ASSESSMENT OF ANALYSIS TECHNIQUES WITH DATA FROM CARDIOVASCULAR AUTONOMIC FUNCTION-TESTS. Quarterly Journal of Medicine 86: 831-836.
137. Krebs HA (1950) CHEMICAL COMPOSITION OF BLOOD PLASMA AND SERUM. Annual Review of Biochemistry 19: 409-430.
138. Ekins R, Edwards P (1997) On the meaning of "sensitivity". Clinical Chemistry 43: 1824-1831.
139. (1976) COMMISSION ON SPECTROCHEMICAL AND OTHER OPTICAL PROCEDURES FOR ANALYSIS - NOMENCLATURE, SYMBOLS, UNITS AND THEIR USAGE IN SPECTROCHEMICAL ANALYSIS .2. DATA INTERPRETATION. Pure and Applied Chemistry 45: 99-103.
140. (1980) GUIDELINES FOR DATA ACQUISITION AND DATA QUALITY EVALUATION IN ENVIRONMENTAL CHEMISTRY. Analytical Chemistry 52: 2242-2249.
141. NATA AU (2009) NATA Technical Note #17, Guidelines for the validation and verification of chemical test methods, National Association of Testing Authorities, Australia. http://www.nata.com.au/phocadownload/publications/Technical_publications/Technotes_Infopapers/technical_note_17.pdf.
142. Mocak J, Bond AM, Mitchell S, Scollary G (1997) A statistical overview of standard (IUPAC and ACS) and new procedures for determining the limits of detection and quantification: Application to voltammetric and stripping techniques (technical report). Pure and Applied Chemistry 69: 297-328.
143. BIPM GUM (2008) Bureau International des Poids et Mesures, Joint Committee for Guides in Metrology, JCGM 100:2008, GUM 1995 with minor correction, Evaluation of measurement data — Guide to the expression of uncertainty in measurement, http://www.ifcc.org/pdf/latestnews/jcgm_100_2008_2010.pdf.
144. Taylor BN, Kuyatt CE (1994) NIST Technical Note 1297,Guidelines for Evaluating and Expressing
the Uncertainty of NIST Measurement Results, Gaithersburg, MD, USA. http://physics.nist.gov/Pubs/guidelines/TN1297/tn1297s.pdf.

145. Armbruster DA, Pry T (2008) Limit of blank, limit of detection and limit of quantitation. The Clinical biochemist Reviews / Australian Association of Clinical Biochemists 29 Suppl 1: S49-52.
146. Currie LA (1995) NOMENCLATURE IN EVALUATION OF ANALYTICAL METHODS INCLUDING DETECTION AND QUANTIFICATION CAPABILITIES (IUPAC RECOMMENDATIONS 1995). Pure and Applied Chemistry 67: 1699-1723.
147. Bunz UHF, Rotello VM (2010) Gold Nanoparticle-Fluorophore Complexes: Sensitive and Discerning "Noses" for Biosystems Sensing. Angewandte Chemie-International Edition 49: 3268-3279.
148. De M, Rana S, Akpinar H, Miranda OR, Arvizo RR, et al. (2009) Sensing of proteins in human serum using conjugates of nanoparticles and green fluorescent protein. Nature Chemistry 1: 461-465.
149. Hortin GL, Sviridov D, Anderson NL (2008) High-abundance polypeptides of the human plasma proteome comprising the top 4 logs of polypeptide abundance. Clinical Chemistry 54: 1608-1616.

Appendix

In this section additional information relevant to the chapters II. Materials and Methods, and III. Results and Discussion, is presented. This information is not necessary to the understanding of the work, and it is ordered according to the its mentioning in the text.

Core-shell model analysis for DCS data.

A simple model to analyse data for protein shell-coated particles was used to get an estimation of the shell thickness (Walczyk D, Bombelli FB, Monopoli MP, Lynch I, Dawson KA (2010) What the Cell "Sees" in Bionanoscience. Journal of the American Chemical Society 132: 5761-5768). If a spherical particle, composed of an inner core of density, ρ_c, with a diameter Dc, and a shell of density, ρ_s, and thickness, Ds, is placed in a rotating disc filled with a fluid of density, ρ_f, the particle will suffer a drag force of the form:

$$F_d = 3\pi D_s \eta \nu \qquad \text{(Eq. A1)}$$

where D_s ($D_s = D_c+2\delta$, with δ being the shell thickness) is the total diameter of the core-shell particle, η is the viscosity of the fluid and ν is the settling velocity of the particle. This force will be balanced by the centrifugal force:

$$F_c = m\omega^2 R \qquad \text{(Eq. A2)}$$

where R is the distance from the particle to the axis of rotation, m is the particle mass and ω is the angular velocity of the disc (and the particle within). Considering the buoyancy and the presence of two different materials in the particle, the mass m can be written as:

$$m = \frac{\pi}{6}\left(\rho_c D_c^{\,3} + \rho_s\left(D_s^{\,3} - D_c^{\,3}\right) - \rho_f D_s^{\,3}\right) \qquad \text{(Eq. A3)}$$

At equilibrium between forces, we have:

$$\left(\rho_c - \rho_s\right)\frac{D_c^{\,3}}{D_s} + \left(\rho_s - \rho_f\right)D_s^{\,2} = \frac{18\eta}{\omega^2}\frac{1}{R}\frac{dR}{dt} \qquad \text{(Eq. A4)}$$

Solving this equation for the simplest case where there is no physical shell ($\rho_c=\rho_s$), we obtain:

$$\left[\left(\rho_c - \rho_f\right)D^2\right]t = \frac{18\eta}{\omega^2} ln\left(\frac{R_f}{R_o}\right) \qquad \text{(Eq. A5)}$$

where dR/dt is the radial velocity, t is the time elapsed while the particle moves between the initial R_o and the final R_f position and D is the measured diameter. Since all DCS measurements are calibrated for this equation in the presence of a shell one can extract the real particle diameter, D_s, from the measured D using the following equation:

$$\frac{(\rho_c - \rho_s)}{(\rho_c - \rho_f)} \frac{D_c^3}{D_s} + \frac{(\rho_s - \rho_f)}{(\rho_c - \rho_f)} D_s^2 = D^2 \qquad \text{(Eq. A5)}$$

DCS results for the AuNP with the different proteins showed a particle size distribution with a main peak (100%) related to the monomeric particle population. From the apparent measured diameter of these peaks we extracted the shell thickness, δ, by knowing ρ_c, ρ_f, ρ_s and D_c. In particular, D_c is set to the value obtained for the bare NPs in buffer and ρc is the density of the material. Actually, ρ_f should be considered as a function of the radius R but it is substituted with an effective quantity, which is its mean value between R_o and R_f. In this case, a source of uncertainty for the quantitative determination of the shell thickness is the choice for the shell density since experimental values for the hydration degree and the actual conformation of the antibody are not available. A value of 1.125 g cm^{-3} was chosen, this is the average value of the density of hydrated protein crystals, 1,23 g cm^{-3}, and of blood plasma, 1,025 g cm^{-3} (Walczyk D, Bombelli FB, Monopoli MP, Lynch I, Dawson KA (2010) What the Cell "Sees" in Bionanoscience. Journal of the American Chemical Society 132: 5761-5768).

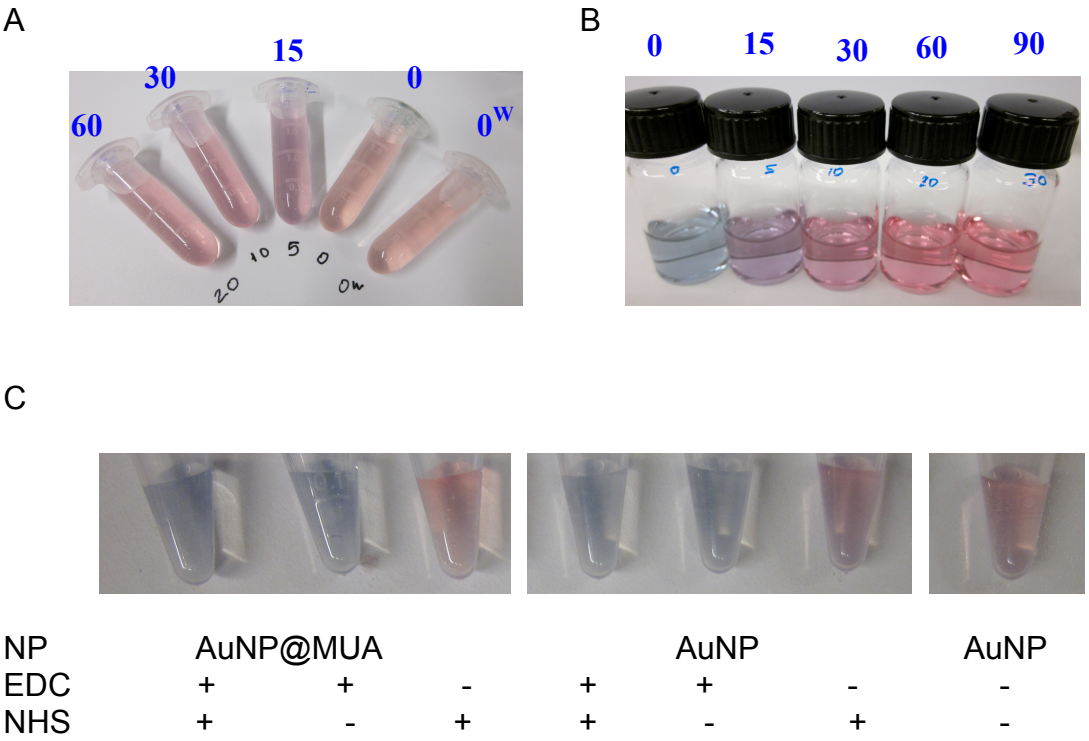

Figure A.1 Digital photographs of homemade-AuNP with different degrees of aggregation promoted by the cross-linkers EDC/NHS or by the antibody. (A) Gold colloids of non cross-linked AuNP@Ab conjugates, showing that ratio 15 (antibody to AuNP molar ratio) exhibited some degree of aggregation (slightly more violet colour) due to the presence of the antibodies, as seen in the UV-Vis spectrum of Figure 3.6 B. 0 and 0^{w}, correspond to AuNP@MUA were no antibody was added, in 0, a 50% V/V addition of PB 1.6 mM, pH 7.0 was performed, as it is performed when the antibody is added, in 0^{w}, water was added instead of PB, this proves that the slight difference in colour between colloids with and without antibody is due to the presence of the antibodies not to some effect caused by PB. (B) Gold colloids of cross-linked AuNP@Ab conjugates, showing that the colloid stabilizes at antibody to NP ratio of 60. (C) Gold colloids showing that the cross-linker's induced aggregation is due to EDC (the cross-linker, NHS is a catalyser) and is independent of the presence of MUA at the nanoparticle surface. This can be derived from the fact that aggregation only occurs when EDC is present, despite the presence of NHS, which doesn't aggregate the particles by itself. All featured colloids were at a concentration of 0.33 nM.

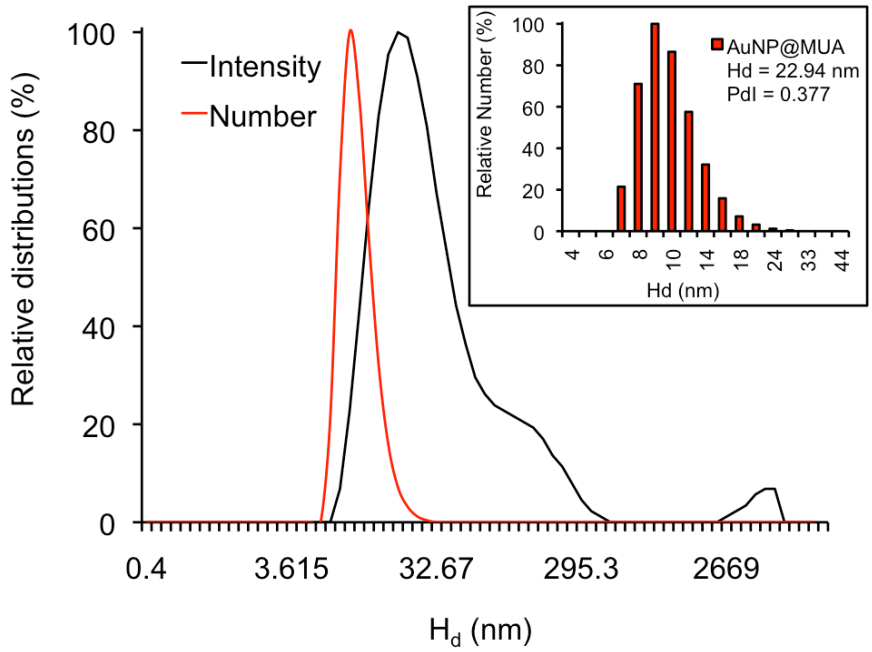

Figure A.2 Comparison between size and number distributions obtained by DLS measurements of AuNP@MUA. Relative number (red line) and intensity (black line) size distribution. Inset: histogram of the relative number size distribution highlighting the size distribution centred close to 10 nm.

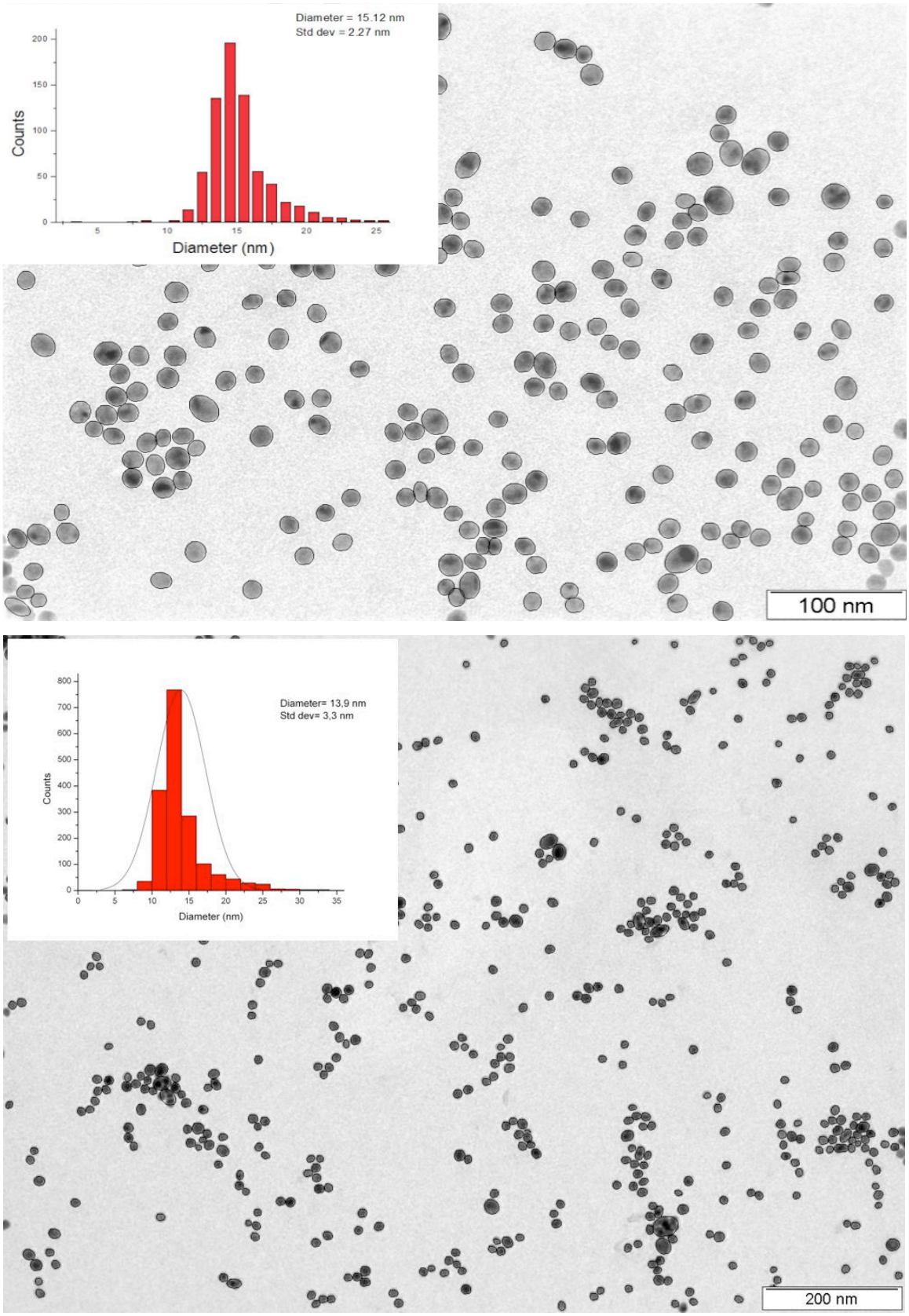

Figure A.3 TEM images from two different batches of citrate stabilized homemade-AuNPs. Data kindly provided by Dr. Pedro Quaresma and Dr. Inês Gomes, DQUP and FCTUNL, Portugal, respectively. Upper panel: 15.12 ± 2.27 nm; lower panel: 13.9 ± 2.3 nm.

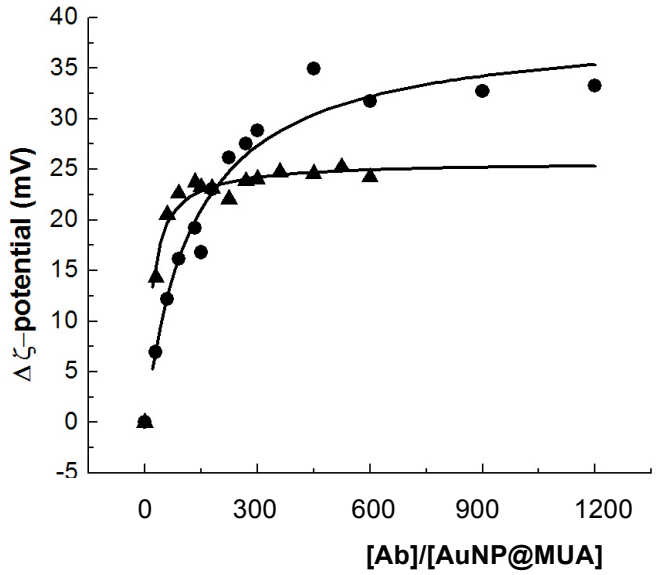

Figure A.4 Analysis of the formation of the AuNP@MUA@Ab conjugates by ζ-potential measurements. ζ-potential variation, in relation to bare AuNP@MUA (Δζ-potential), for the AuNP@Ab conjugates, as a function of the antibody to AuNP@MUA molar ratio. Triangles and circles refer to conjugates prepared in the absence and in the presence of the EDC/NHS cross-linkers, respectively. Lines represent the fits to a Langmuir-type adsorption isotherm.

ζ-potential measurements give an indication of the particles surface charge in solution. The actually measured parameter when the ζ-potential is performed is the electrophoretic mobility of the light scattering particles, so, as for the agarose gel electrophoresis experiments, increasing antibody to AuNP-MUA molar ratios lead to both a increase of the particles size and a global decrease of the particles charge, the seen effect during the measurements is a decrease of the particles electrophoretic mobility. Agarose gels showed a saturation of the particles surface with antibodies, assessed by a plateau in the electrophoretic mobility (Figure 3.12), for smaller molar ratios when NHS/EDC cross-linkers are used; in good agreement, ζ-potential measurements (Figure A.2) showed a saturation, as accessed by a plateau in the ζ-potential, for smaller molar ratios when the cross-linkers are used. Both these techniques prove conjugation, and indicate that more antibodies are bound at the AuNP-MUA's surface when saturation is achieved, when the simple conjugation approach is used.

A plot of the variation of the ζ-potential in relation to AuNP-MUA alone against the [Ab]/[AuNP@MUA] ratio, generates a Langmuir type of adsorption curve (Gomes I, Santos NC, Oliveira LMA, Quintas A, Eaton P, et al. (2008) Probing Surface Properties of Cytochrome c at Au Bionanoconjugates. Journal of Physical Chemistry C 112: 16340-16347.)(Figure A.4). A larger variation on the ζ-potential value was observed for the electrostatic AuNP@Ab (ca. 35 mV) in

comparison with the cross-linked AuNP@Ab (ca. 25 mV). This observation is an indication of adsorption of a ca. 30% larger amount of antibody to the electrostatic AuNP@Ab, in relation to cross-linked AuNP@Ab. The binding constant for both types of bionanoconjugates could be determined by fitting a Langmuir-type curve to the experimental data (Eq. A6)

$$\Delta\xi = \frac{\Delta\xi_{\max} K_L R}{1 + K_L R} \qquad \text{Eq. A6}$$

in which $\Delta\zeta$ is the variation in the ζ-Potential measured for a certain [Ab]/[AuNP@MUA] in relation to the ζ-potential value obtained for AuNP@MUA alone; $\Delta\zeta_{max}$ is the maximum value for $\Delta\zeta$-potential as [Ab]/[AuNP@MUA] increases and K_L is a binding constant corresponding to the value of the inverse of the concentrations ratio, for one-half of $\Delta\zeta_{max}$. R is the ratio of [Ab]/[AuNP@MUA]. The binding constant for the formation of AuNP@Ab was determined to be K_L= 0.023 for the electrostatic conjugates, and KL= 0.161 for the cross-linked conjugates, a seven-fold increase. This result corroborates observations from the agarose gels of both types of conjugates, indicating that smaller [Ab]/[AuNP] ratios are needed to saturate the AuNP@MUA surface with the crosslinking approach.

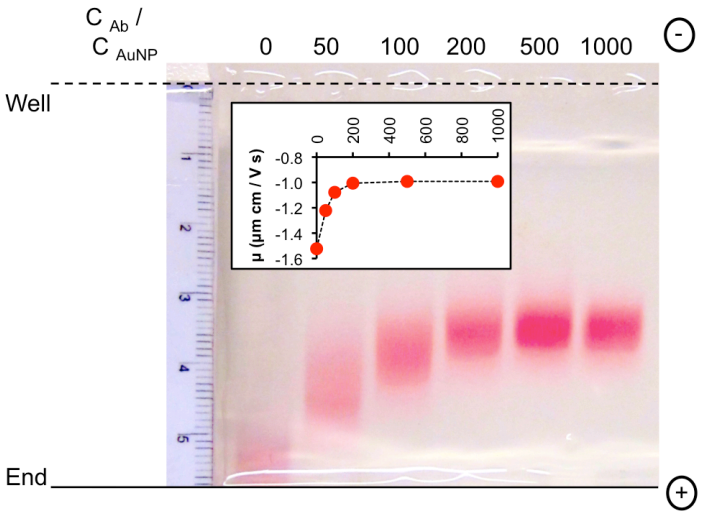

Figure A.5 Digital picture of the AGE of commercial-AuNP antibody conjugates (AuNP@Ab). Eight wells gels with 0.5 % agarose were used to run the samples (27 μL of the pelleted nanoparticles plus 3 μL of glycerol) at a constant voltage of 300 V for 30 minutes. Inset, apparent electrophoretic mobilities (μ) calculated from the migration rate (ν = distance (μm) / time (1800 s)) and the applied electric field, E = electro motive force (150 V) / electrode spacing (15 cm).

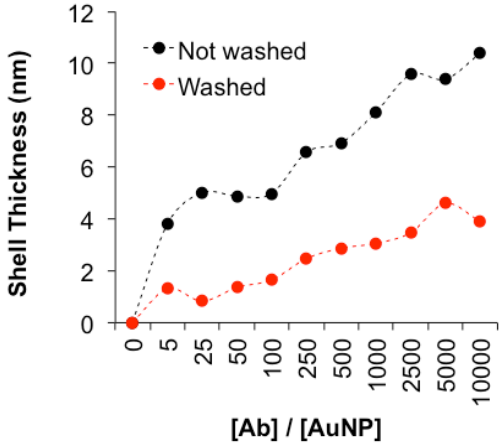

Figure A.6 Ab shell thickness variation in commercial AuNP@Ab conjugates with increasing Ab to AuNP ratio before (Not washed) and after washing (washed) by centrifugation.

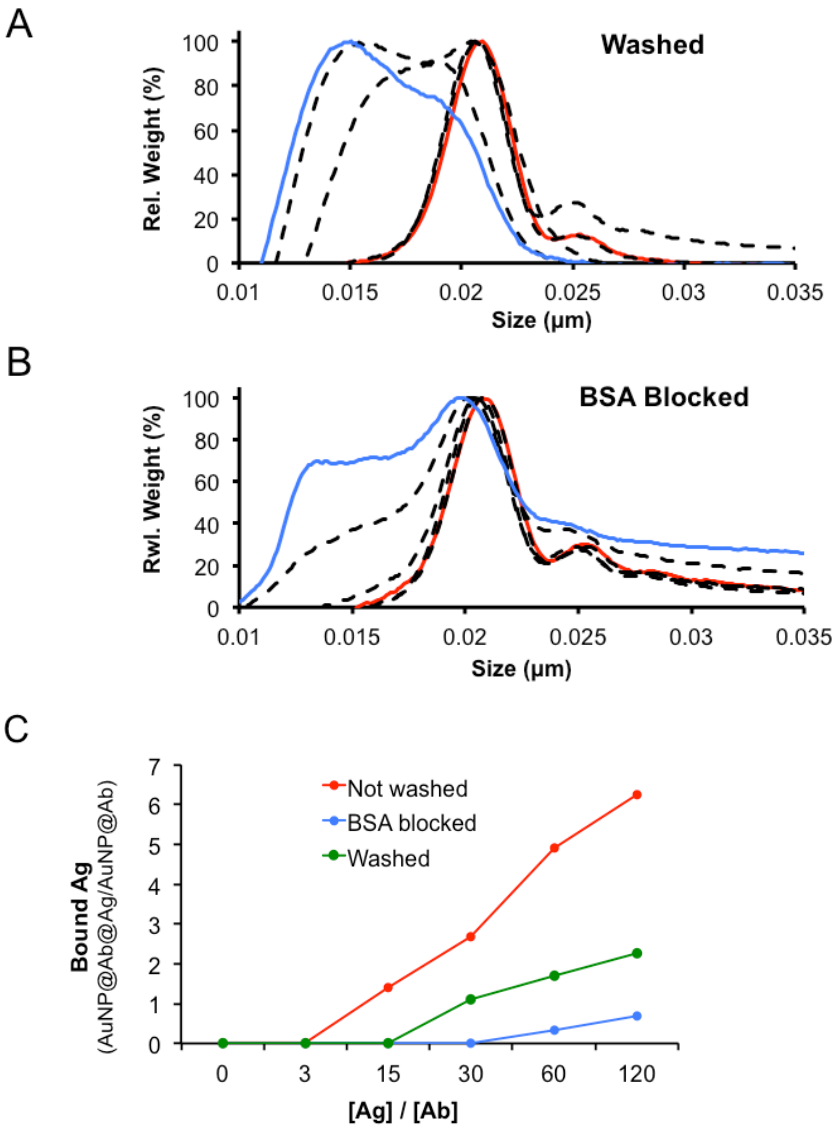

Figure A.7 DCS relative weight particle size distributions of AuNP@Ab incubated with increasing Ag concentrations after washing and BSA blocking. (A) and (B) AuNP@Ab@Ag conjugates at different Ag to Ab ratios for washed and BSA blocked conjugates respectively. Upon incubation of AuNP@Ab conjugates (red line) with Ag at increasing Ag to Ab molar ratios, a change in the weight distribution is seen (dotted arrows) from a near Gaussian distribution when there is no Ag, towards a bimodal weight distribution with increasing amounts of Ag bound to the AuNP@Ab. Blue line corresponds to the higher ratio tested. Ag was added at the Ag to Ab molar ratios of 3, 15, 30, 60 and 120; corresponding to final concentrations ranging from 4.0 to 160 μg mL^{-1}. (C) Comparison of the extent of Ag binding between the conjugates used throughout the work (Not washed), and their washed and BSA blocked counterparts. The binding extent was accessed by the ratio between the relative weight values at 14 and 19 nm, the approximate sizes of the two populations in the weight distribution, AuNP@Ab@Ag and AuNP@Ab. This parameter was used to monitor the extent of Ag binding instead of the fitted Gaussian areas because the extensive aggregation seen in the (A) and (B) would bias the fitted areas. Incubation was performed for 120 minutes at RT.

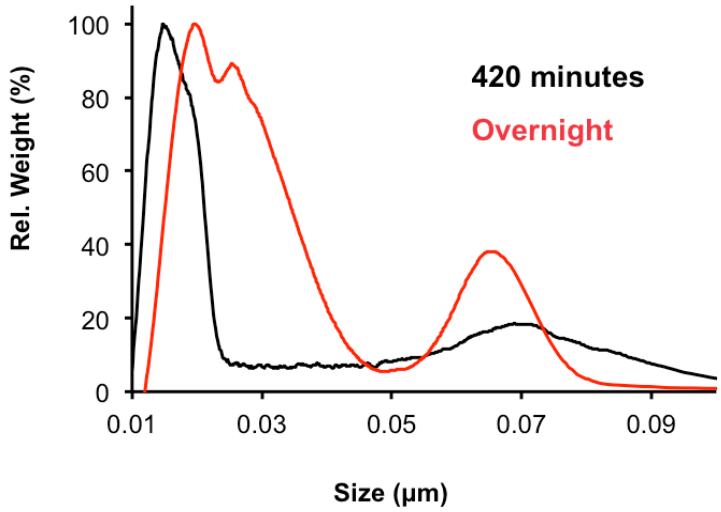

Figure A.8 DCS relative weight size distributions of AuNP@Ab@Ag at an Ag to Ab molar ratio of 30 after overnight (~12 hours) and 420 minutes incubation (7 hours) at room temperature.

AuNP's surface chemistry and Ag's buffer: influence on the Ag binding

To assess the influence of the Ag buffer on the extent of Ag binding the PBS buffered Ag was buffer exchanged to PB or Borate buffer (BB, 150 mM Borate, 100 mM NaCl, pH 8.3) using ultrafiltration devices (5 KDa, MWCO, 4 cicles of centrifugation to 1/20th of the initial volume followed by buffer addition until the initial volume). The differently buffered Ag solutions where then incubated with the commercial AuNP@Ab conjugates. The extent of Ag binding was evaluated by the changes in the AuNP@Ab shell-thickness. PB and BB did not increase the extent of Ag binding (Figure A.9 B).

The influence of the surface chemistry was also evaluated by the changes in the shell thickness, using PBS as the Ag buffer. Commercial AuNP@Ab conjugates where the most active (Figure A.9 C). The DCS size distributions of the shell thickness analysis presented in Figure A.9 are presented on Figure A.10.

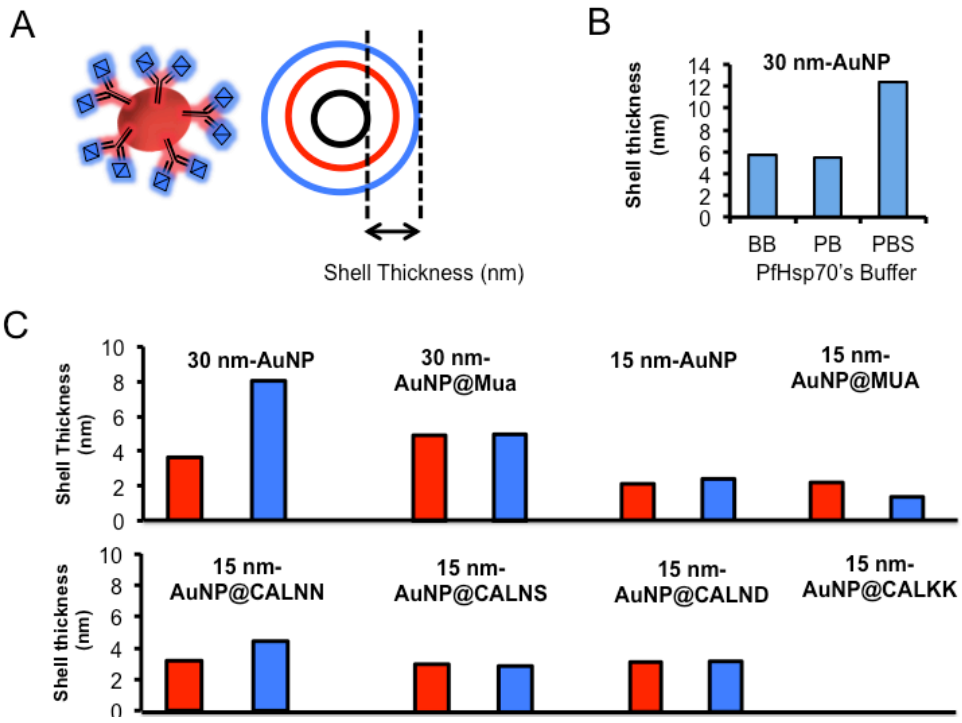

Figure A.9 Influence of AuNP's surface chemistry and the Ag's buffer on the Ag to BNC binding. (A) Schematic representation of AuNP@Ab@Ag conjugates, with depiction of the shell thickness as the protein thickness (nm) covering the AuNP inorganic core. (B) Shell thickness variation of the AuNP@Ab@Ag when the Ag's storage buffer is varied: phosphate buffer (PB), phosphate buffered saline (PBS) and borate buffer (BB). (C) Shell thickness variation of the AuNP@Ab (red column) and AuNP@Ab@Ag (blue column). CALNX, where X= N,S or D and CALKK are pentapeptides, MUA is mercaptoundecanoic acid. The surface modifier to AuNP molar ratio was 120:1. 15 nm- and 30 nm-AuNP stands for home made and commercial AuNP. The Ag was in PBS when added to the NPs, at an [Ag]/[AuNP]=100. For the commercial AuNP: [AuNP]=0.56nM and [Ab]/[AuNP]=200; for the home made AuNP: [Ab]/[AuNP]=300, [AuNP]=0.67nM. Incubation time of 120 minutes.

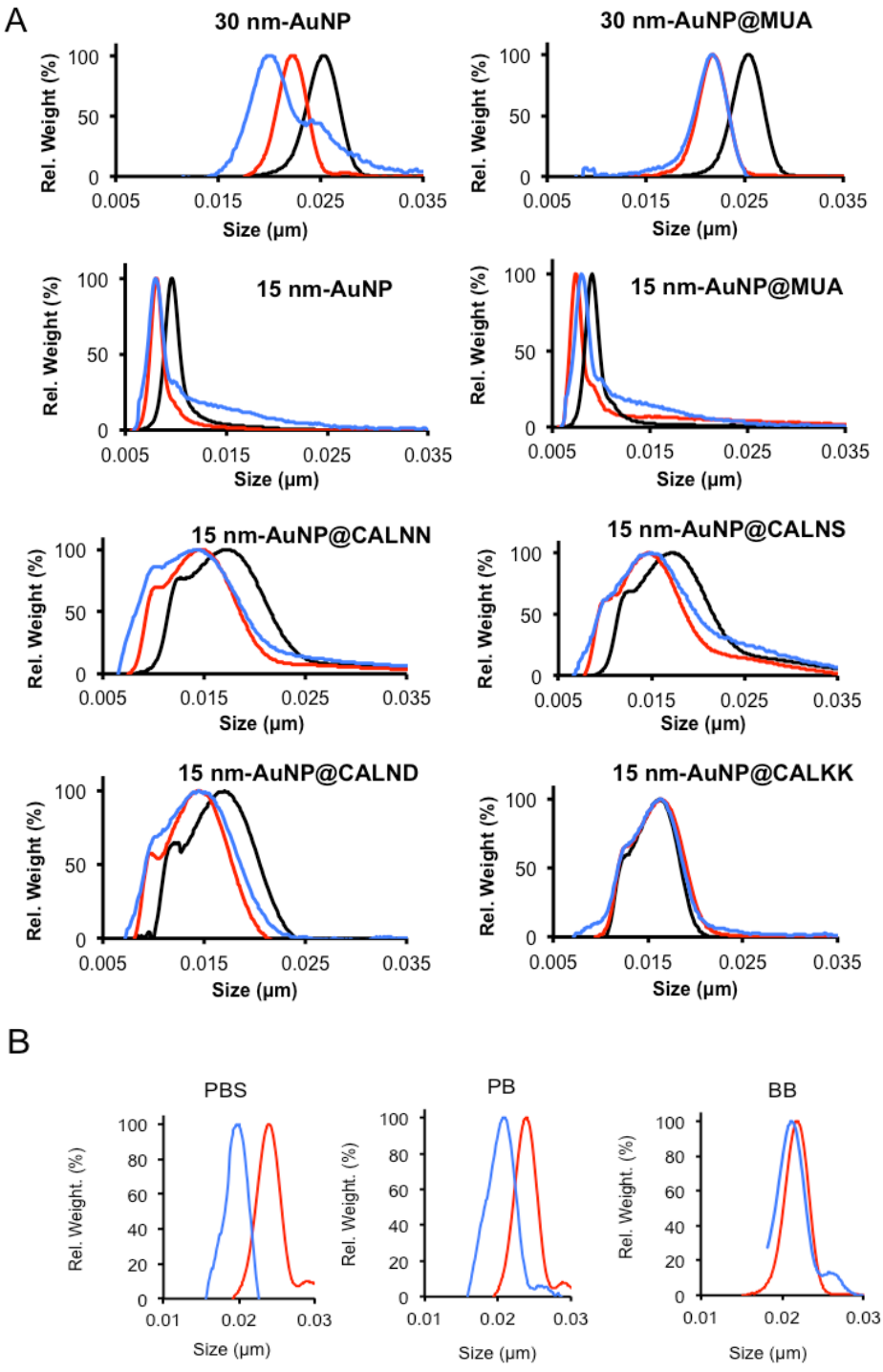

Figure A.10. Influence of surface chemistry and PfHsp70's buffer on the Ag to BNC binding. DCS relative weight size distributions of the AuNP (black lines), AuNP@Ab (red lines) and AuNP@Ab@Ag (blue lines) of the experiments on the influence of surface chemistry (A) and influence of Ag buffer (B) in the Ag to Ab binding. Experimental conditions detailed in Figure A.9.

Additional Figures and discussion pertinent to Section "21.4.1. Linear response regions".

Selection of the plotting variables

In some cases to obtain linearity between assays and sample concentrations, the test data may need to be subjected to a mathematical transformation prior to regression analysis (International Conference on Harmonisation Of Technical Requirements For Registration Of Pharmaceuticals For Human Use –ICH- Harmonised Tripartite Guideline Validation Of Analytical Procedures: Methodology, 2005. Recommended for Adoption at Step 4 of the ICH Process on 6 November 1996 by the ICH Steering Committee). Examples of these transformations are using a logarithmic scale for the sample concentration, or transforming the analytic signal into a relative number, as in the case of F.Inc. parameter in homemade-AuNP immunoassays. Throughout the literature many examples can be found of combinations of quantity and analytical signal or some derivative of it, as concentration, mass, and logarithmic scales of these, to fluorescence intensities or relative fluorescence increases.

The decision on how to plot the results was made upon five criteria: 1) the concentration and analyte signal should have a visually detectable linear region; 2) the correlation coefficient of the linear regression should be as close to unit as possible; 3) the linear detection range should be the largest possible; 4) suitability to compare the calibration curves obtained by different experimental methods (in this case fluorescence and AGE); 5) ability to present results that could be intuitively understood (the analytical signal and the concentration in $\mu g.mL^{-1}$, is preferred over mathematical treatments of these quantities).

The linear correlation coefficient (R^2) for the different assays: fluorescence, for commercial- and homemade-AuNP, and AGE for commercial-AuNP, for the different possibilities of results plotting: analytical signal (electrophoretic mobility and fluorescence intensity), mathematically derived signal (mobility decrease (%) and fluorescence increase (%)), Ag concentration and logarithm of antigen concentration, are presented in Table A.1.

Table A.1. R^2 values for the different plotting possibilities in the electrophoretic and fluorescence immunoassays

	Fluorescence, home made AuNP	
	F.I. (arb. units)	*F.Inc. (%)*
[Ag]	0.989	0.995
log ([Ag])	0.968	0.982
	Fluorescence, commercial AuNP	
	F.I. (arb. units)	*F.Inc. (%)*
[Ag]	0.975	0.954
log ([Ag])	0.976	0.991
	Agarose gel electrophoresis, commercial AuNPs	
	Mobility (um cm / Vs)	*Mob. Decrease (%)*
[Ag]	0.977	0.991
log ([Ag])	0.973	0.958

In the case of the immunoassay with homemade-AuNPs, the regression analysis was performed on a fluorescence increase (F.Inc. (%)) *vs* analyte concentration ([Ag]) plot. Using F.I. (arb. units), a linear response region was also obtained but the R^2 decreased from 0.995 to 0.989. Using the log ([Ag]) did not improve the value of R^2.

In the case of the fluorescence immunoassays with commercial-AuNP (Figure A.12), linear regions could also be found for all the possible plotting combinations. With the logarithmic scale, the shape of the curves was altered and the linear regions were obtained at higher concentration. The plotting possibilities for the AGE immunoassays are depicted in Figure A.13.

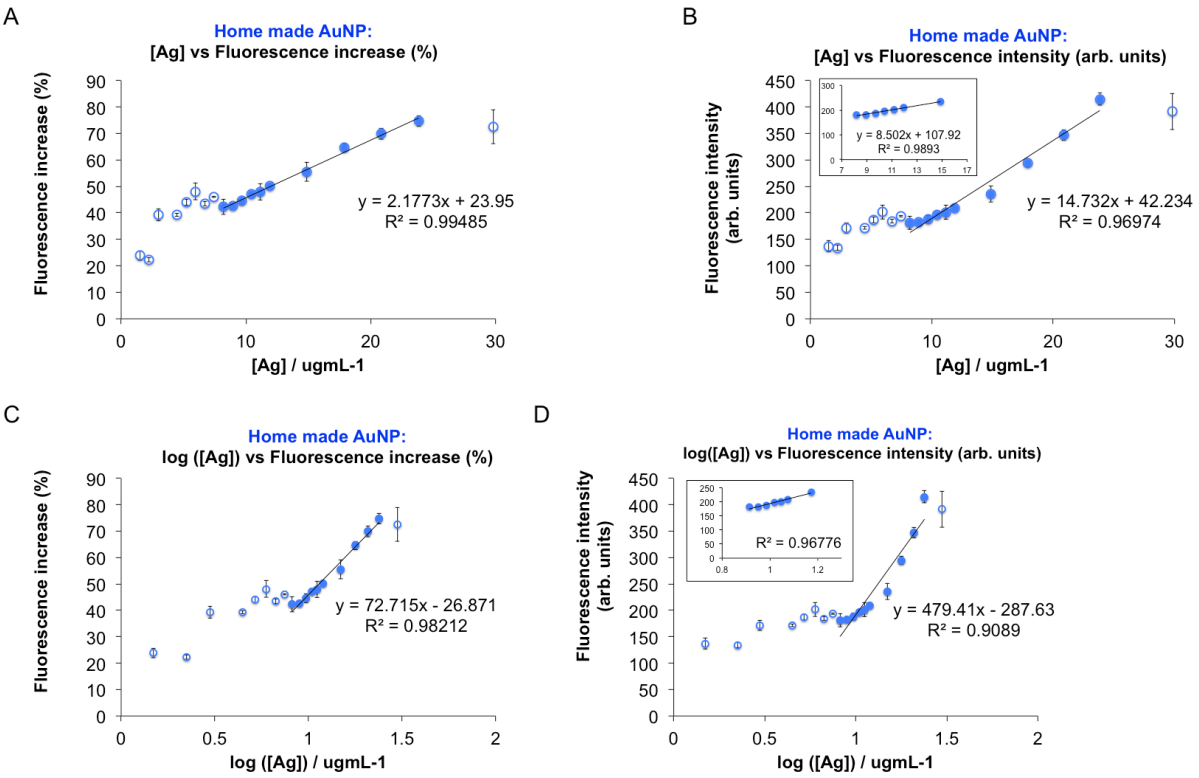

Figure A.11 Comparison of the different plotting possibilities of the fluorescence immunoassay results with home made AuNP. Results are plotted as F.Inc. (%) and F.I. (arb. units) *vs* [Ag] in (A) and (B) respectively, and *vs* log ([Ag]) in (C) and (D) respectively. The experimental concentration values that where used in the linear regression and those, which were not, are plotted as filled and open circles respectively. From (A) to (D) the experimental concentration values used for linear regression were the same, when different values were used to emphasize different linear regions they are shown as insets.

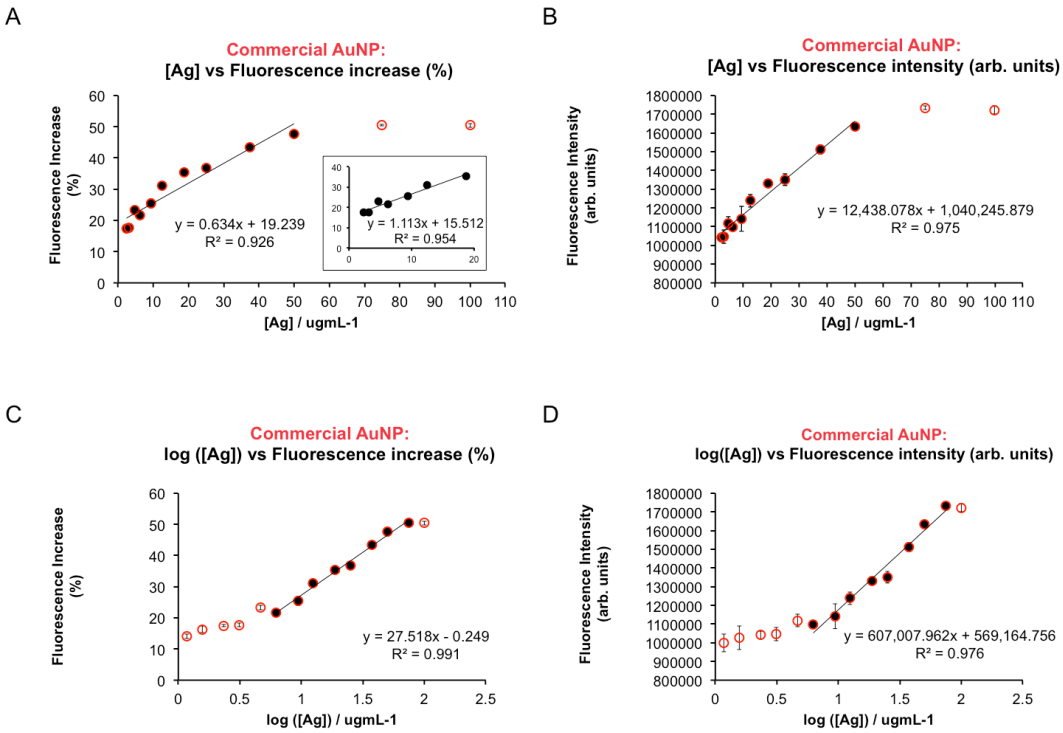

Figure A.12 Comparison of the different plotting possibilities of the fluorescence immunoassay results with commercial AuNP. Results are plotted as F.Inc. (%) and F.I. (arb. units) *vs* [Ag] in (A) and (B) respectively, and *vs* log ([Ag]) in (C) and (D) respectively. The experimental concentration values that where used in the linear regression and those, which were not, are plotted as filled and open circles respectively. From (A) to (D) the experimental concentration values used for linear regression were the same, when different values were used to emphasize different linear regions they are shown as insets.

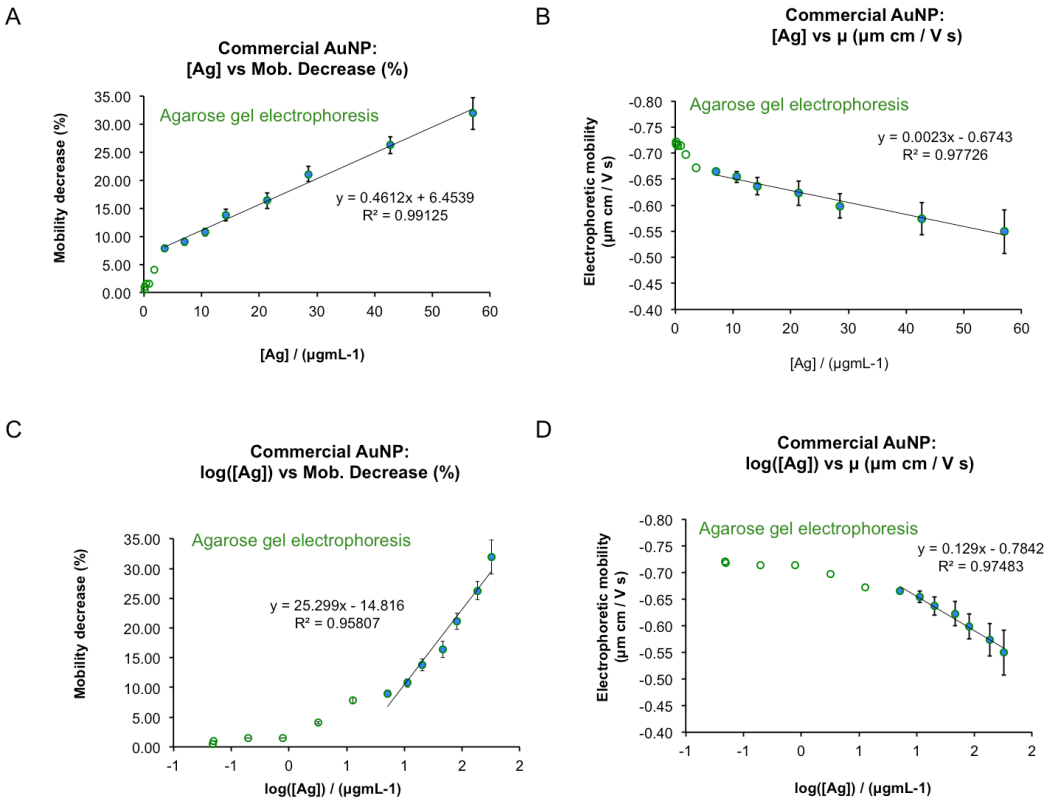

Figure A.13 Comparison of the different plotting possibilities of the agarose gel electrophoresis immunoassay results with commercial AuNP. Results are plotted as F.Inc. (%) and F.I. (arb. units) *vs* [Ag] in (A) and (B) respectively, and *vs* log ([Ag]) in (C) and (D) respectively. The experimental concentration values that where used in the linear regression and those, which were not, are plotted as filled and open circles respectively. From (A) to (D) the experimental concentration values used for linear regression were the same, when different values were used to emphasize different linear regions they are shown as insets.

Additional discussion pertinent to Section "21.4.2. Analytical parameters for quantitative comparison of the immunoassays performance".

Significance level for the LoD, LoSD, LoINH and LoIB for the different techniques

LoD

For fluorescence this was the minimal [Ag] where the F.I.(Sample) (average ± 3 x *SD*) was significantly higher then the F.I.(Blank) (average ± 3 x *SD*). The analysis was performed on the average of the F.I. of 3 measurements, on 2 different days; for AGE this consisted of the minimal [Ag] were the mobility (AuNP@Ab@Ag) (average ± *SD*) was significantly retarded, i.e. it migrated less towards the positive electrode, in respect to the mobility (AuNP@Ab) (average ± *SD*). The analysis was performed on the average of 3 measurements, each performed on different days. For DCS this was considered to be the minimal [Ag] where a bimodal distribution could be detected;

LoSD

For the fluorescence, this consisted of the minimal [Ag] where the F.I. (AuNP@Ab@Ag) was significantly higher than the F.I. (AuNP@Ab@Trf) conjugates sample. For AGE experiments, this consisted of the minimal [Ag] in which the mobility (AuNP@Ab@Ag) was significantly retarded in relation the mobility (AuNP@Ab@Trf). For DCS the LoSD was the same as the LoD, as Trf binding was not detected.

LoINH

For fluorescence experiments, this consisted of the minimal [Trf] where the F.I. (AuNP@Ab@Ag@Trf+CyAg) was significantly lower than the F.I. (AuNP@Ab@Ag+CyAg). For AGE this consisted of the minimal [Trf] where the mobility (AuNP@Ab@Ag@Trf) increased, i.e. it moved more towards the positive electrode, in respect to the mobility (AuNP@Ab@Ag). For DCS, this was considered to be the minimal [Trf] where the bimodal distribution of AuN@Ab@Ag conjugates shifted towards AuNP@Ab conjugates.

LoIB

For fluorescence, this consisted of the minimal [Trf] concentration where the F.I. (AuNP@Ab@Trf+CyAg) was higher then the F.I.(Blank). For AGE this consisted of the minimal [Trf] where the mobility (AuNP@Ab@Trf) was decreased, i.e. it moved less towards the positive electrode, in respect to the mobility (AuNP@Ab) conjugates. For DCS, no Trf binding was observed.

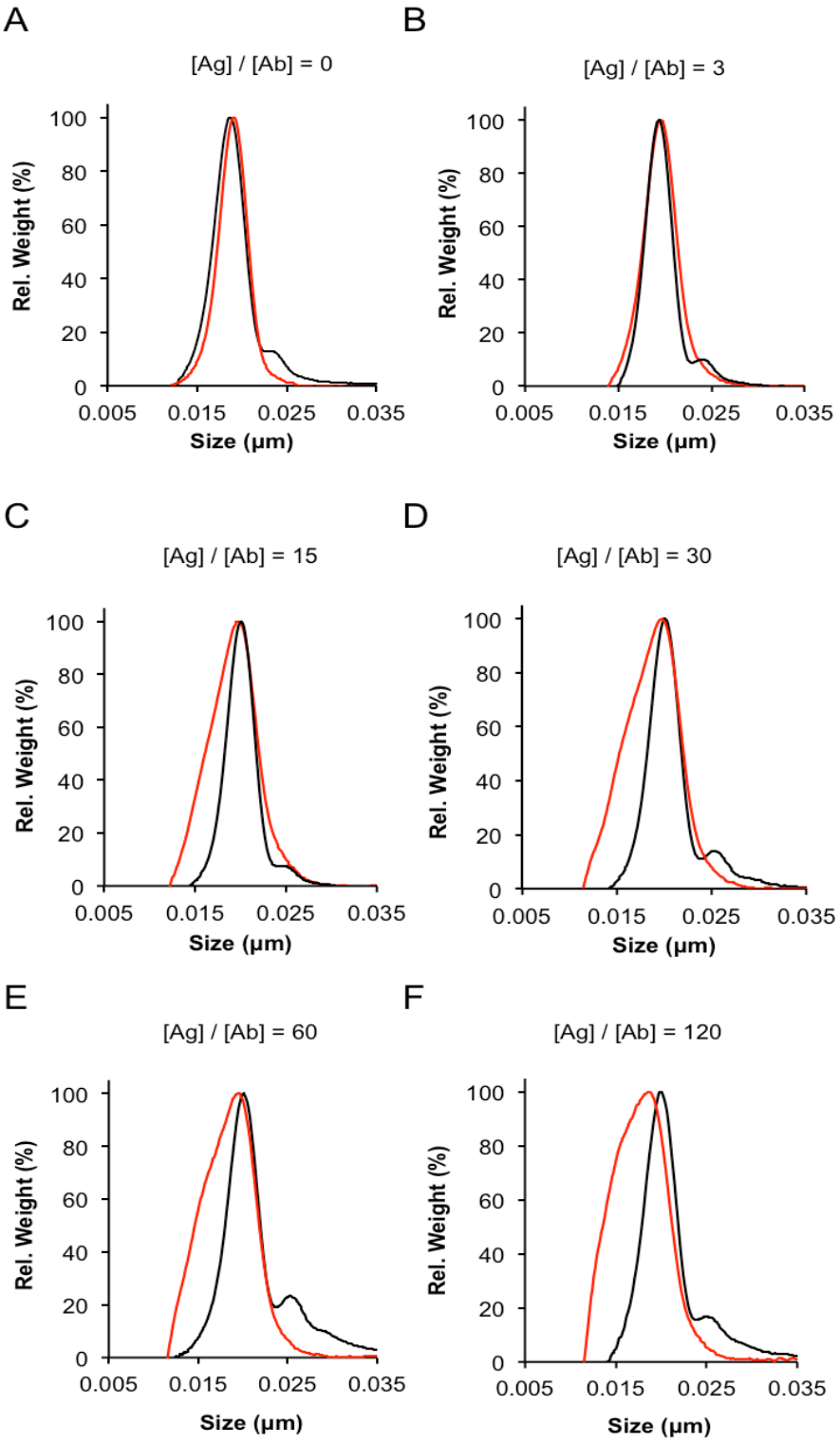

Figure A.14 DCS weight distributions of the Ag binding to AuNP@Ab conjugates at increasing Ag concentrations in the presence of 2% plasma. (A) to (F) DCS relative weight size distributions of AuNP@Ab@Ag and AuNP@Ag incubated with plasma (2 % V/V) at increasing Ag to Ab ratios, 3, 15, 30, 60 and 120; corresponding to final concentrations ranging from 4.0 to 160 µg mL^{-1}. Red lines AuNP@Ab@Ag, black lines AuNP@Ag. Note that plotting the results for AuNP (black lines), in parallel to the results for the AuNP@Ab@Ag (red lines) is meant to facilitate the visual perception of the change from the monomodal distribution towards the bimodal distribution. It also proves that the distribution changes are not plasma induced and are dependent on the presence of Ag.

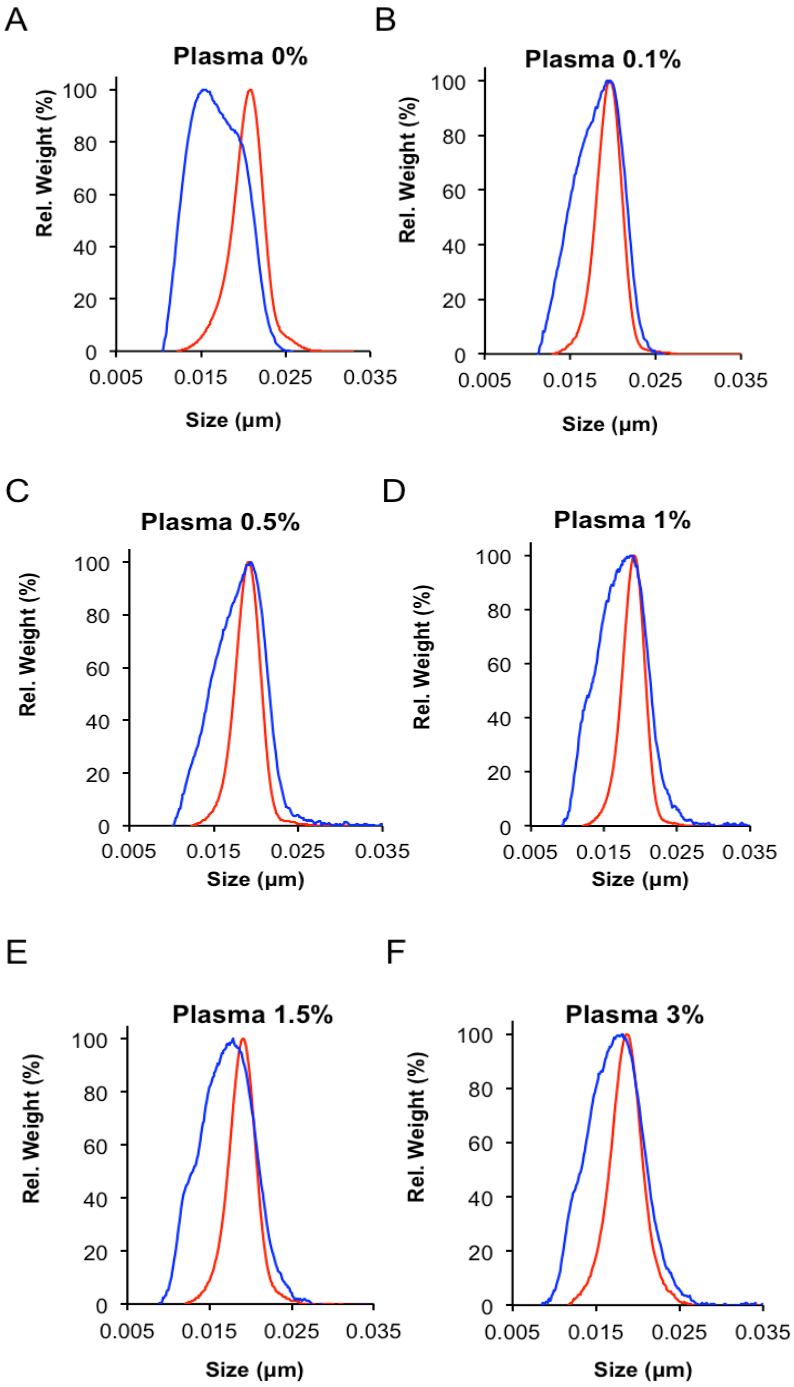

Figure A.15 DCS relative weight size distributions for the influence of plasma in the Ag to AuNP@Ab binding at increasing plasma concentrations. (A) to (F) DCS relative weight size distributions of AuNP@Ab@Ag (molar ratio of 30 to 1) and AuNP@Ab at increasing plasma concentrations. Red lines AuNP@Ab, blue lines AuNP@Ab@Ag. Plasma concentrations: 0.1, 0.5, 1.0, 1.5 and 3.0 %, corresponding to natural occurring Trf concentrations of 4.0, 20, 40, 60 and 120 µg mL^{-1}. Note that plotting the results for AuNP@Ab (blue lines) without Ag, in parallel to the results for the AuNP@Ab@Ag (red lines) is meant to facilitate the visual perception of the change from the monomodal distribution towards the bimodal distribution. It also proves that the distribution changes are not plasma induced.